Università degli Studi di Padova

Dipartimento di Ingegneria Civile, Edile e Ambientale

Scuola di Dottorato di Ricerca

in Scienze dell'Ingegneria Civile e Ambientale

XXXVI Ciclo

Uncertainty Quantification of the Continuous and Discontinuous Geomechanical Response in Over-exploited Aquifers

Coordinator: *Prof. Massimiliano Ferronato*

Supervisor: *Prof. Pietro Teatini*

Co-Supervisor: *Dr. Claudia Zoccarato*

Ph.D. student: *Yueting Li*

Acknowledgments

I would like to take this opportunity to express my heartfelt gratitude and appreciation to all those who have supported and helped me throughout my journey in completing this thesis.

First and foremost, I am deeply grateful to my advisor, Prof. Pietro Teatini, for providing me with the invaluable opportunity to pursue doctoral studies and for his unwavering support and continuous encouragement. Over the past three years, Prof. Teatini has not only offered insightful suggestions but has also inspired me to become a better researcher. I am honored to have had such a dedicated mentor who has played a pivotal role in shaping my growth and development in the field.

I would also like to extend my heartfelt thanks to my co-advisor, Claudia Zoccarato, for her unwavering dedication and support throughout this journey. Her guidance in navigating the topic of uncertainty quantification, her endless patience, and her assistance with the writing process have been invaluable. This thesis would not have been possible without their commitment and expertise.

I am also indebted to the members in Simo, Caterina, Laura, Andrea, Pellizzon, Selena, Miao, Zohreh and Prof. Massimiliano. Their kindness, assistance, and accompany over the past three years have created a lovely environment. I am grateful for the chance to learn and work together.

Thanks to the European Union PRIMA Programme for funding my PhD scholarship under grant agreement No. 1924, project RESERVOIR. I also extend my gratitude to the members of RESERVOIR. It has been an excellent experience studying this interesting topic and working in this diverse and inclusive team. Thank you for the share of knowledge which is fundamental to this thesis. Thanks to Naomi, Lorenzo and Chiara for their expertise and contributions to this thesis.

I would like to express my gratitude to my dear friends in the residence, who have provided support, encouragement, and kindness throughout these past three years. Specifically, I would like to thank my landlord, Ruggero, for creating a friendly and warm atmosphere that made me feel like being home. To Martine, Eli, Agatha, Gauri and Sogand thank you for all the joyful memories and sharing moments.

Lastly, I want to express my deepest appreciation to my family for their unconditional love, understanding, and constant support.

Abstract

Groundwater over-exploitation has resulted in various adverse geomechanical consequences, notably land subsidence and the emergence of earth fissures. Despite extensive efforts to predict these geohazards, many studies have overlooked the uncertainties stemming from aquifer properties and geological conditions. Therefore, this thesis aims to quantify associated uncertainties through the integration of numerical modeling approaches, monitoring techniques, surrogate models, and statistical methods.

Prior research has underscored the importance of accurate predictions in land subsidence, necessitating proper characterizations of primary parameters such as hydraulic conductivity, soil compressibility, or specific storage. In the context of homogeneous aquifer systems, a surrogate-model-based Bayesian inversion method is proposed. This method leverages a coupled variably-saturated groundwater flow and geomechanical model alongside interferometric synthetic aperture radar (InSAR) data to infer the posterior distribution of these aquifer parameters. To alleviate computational burden, sparse grid collocation is employed to construct cost-effective surrogate models for efficient Markov Chain Monte Carlo (MCMC) sampling. Application of this framework in the Alto Guadalentín Basin, Spain, successfully characterizes hydraulic conductivity and compressibility.

Additionally, this thesis develops a decoupling methodology to characterize heterogeneous parameter distributions in confined aquifer system. In these cases, Bayesian inversion remains computationally challenging. Here, the focus lies on characterizing specific storage, while hydraulic conductivity has been previously deduced by incorporating piezometric data into groundwater flow modeling. Based on groundwater solution and mesh configuration, specific storage at InSAR observational points is derived using a one-dimensional Terzaghi consolidation equation. Subsequently, the Kriging method is employed to estimate the spatial distribution of specific storage by interpolating these computed "observations". The efficacy of this methodology is demonstrated in the Gediz River Basin, Turkey.

In addition to land subsidence, earth fissure formation is investigated using a novel numerical approach. By incorporating interface elements (IEs) into the continuum finite element (FE) model, the present thesis replicates the formation and development of multi-fissures in the Guangming village, China. Numerical outcomes reveal the mechanisms behind fissure forma-

tion, where tensile stresses cause opening and shear stresses lead to sliding. Furthermore, global sensitivity analyses are conducted using three different methods: Monte Carlo method, polynomial chaos expansion (PCE), and gradient boost tree (GBT). All analyses highlight the significant impact of ridge slope in triggering earth fissures given specific piezometric level declines.

Overall, this thesis significantly advances our understanding of the complex behaviors of over-exploited aquifer systems and offers effective methodologies to address associated uncertainties. These contributions are crucial in the development of sustainable groundwater management strategies, especially in face of escalating water demand.

Acronym

Acronym	Full name
FE	Finite Element
GBT	Gradient Boost Tree
GW	Groundwater
IE	Interface Element
INSAR	Interferometric Synthetic Aperture Radar
LOS	Line Of Sight
MAP	Maximum A Posterior
MCMC	Markov Chain Monte Carlo
MDA	Mean Decrease Accuracy
PCE	Polynomials Chaos Expansion
QoI	Quantity Of Interest
UQ	Uncertainty Quantification

Contents

List of Figures

List of Tables

Chapter 1

Introduction

Groundwater has become a critical resource supporting various human endeavors, including residential consumption, irrigation, and industrial applications, particularly in the context of global climate change Margat and Van der Gun [2013], Famiglietti [2014], Goldstein et al. [2015]. The intensification of groundwater exploitation has resulted in a series of adverse economic, social, and environmental impacts.

One well-known consequence is land subsidence, defined as the gradual downward settling or sinking of the land surface. In recent decades, land subsidence associated with groundwater withdrawal has emerged as a pressing concern [Galloway and Burbey, 2011, Gambolati and Teatini, 2015, Guzy and Malinowska, 2020]. The problem is particularly severe in regions with limited water availability, such as arid and semi-arid areas, as well as in coastal and deltaic zones where groundwater is a crucial resource for water supply [Teatini et al., 2006b, Shi et al., 2007, Castellazzi et al., 2016, Minderhoud et al., 2017, Pirouzi and Eslami, 2017]. Land subsidencce poses significant threats to structural integrity, disrupts infrastructure such as roads and pipelines, damages well casing, exacerbates saltwater intrusion, amplifies flood risks in coastal cities, and diminishes both porosity and permeability within geological formations, consequently reducing well yields and aquifer storage [Eggleston and Pope, 2013, Rahmawati et al., 2013, Smith et al., 2017, Wade et al., 2018].

Moreover, differential land subsidence is associated with a non-uniform distribution of stresses in the underlying sedimentary layers. When these localized stresses exceed a critical threshold, it may manifest as land surface fracturing, which is typically denoted as earth fissures [Burbey, 2002,

Budhu and Shelke, 2008, Carreón-Freyre et al., 2016]. These geologic occurrences have the potential to seriously compromise structural integrity and environmental safety. Specifically, earth fissures can act as conduits for the percolation of pollutants into deep groundwater aquifers, thus endangering the quality of water resources. Additionally, such fissures are capable of disrupting natural drainage systems [Budhu, 2011, Conway, 2016, Yoo and Frederick, 2017, Peng et al., 2020].

For these reasons, it is essential to acquire a comprehensive understanding of these geohazards and implement measures to mitigate potential adverse effects through strategic groundwater management policies. Consequently, predictive modeling for aquifer deformation in response to groundwater withdrawal has gained increasing attention, with specifically developed numerical models devised to simulate real-world occurrences of land subsidence [Kasmarek and Strom, 2002, Burbey, 2002, Teatini et al., 2005, Ye et al., 2016].

The accuracy of computational models in forecasting anthropogenic land subsidence depends on the reliability of hydrogeological and geomechanical data characterizing the aquifer system. Among these parameters crucial for robust simulations are hydraulic conductivity and bulk compressibility. Hydraulic conductivity plays a crucial role in governing the dynamics of groundwater flow field, thereby influencing the variation of hydraulic head consequent to groundwater extraction [McLaughlin and Townley, 1996, Castagna and Bellin, 2009, Rubin et al., 2010]. Bulk compressibility, on the other hand, is key in determining the extent of aquifer compaction resulting from pore pressure reduction [Hoffmann et al., 2003, Galloway and Burbey, 2011, Gazzola et al., 2021].

Direct measurements of these two parameters, such as through pumping tests and laboratory tests, are often impractical in real-world applications. As an alternative, estimations of these parameters rely on indirect inference from field measurements and computational models, e.g., piezometric records and land subsidence measurements, forming what is known as an inverse problem [Tarantola, 2005, Kaipio and Somersalo, 2006].

Bayesian inference is considered to be a quite common approach to solving inverse problems and estimating parameters in the presence of uncertainty. It provides a framework to update prior knowledge about the parameters of a model based on observed data. Prior information encodes preliminary assumptions concerning the parameters, such as aquifer properties, and is represented as a probability distribution. The likelihood distribution

integrates information from observed data and the model, enabling the refinement of prior assumptions, ultimately yielding the inverse solution in the form of a posterior distribution [Gelman et al., 1995].

Markov chain Monte Carlo (MCMC) technique is a common method to investigate the posterior distribution. MCMC algorithms construct a Markov chain to explore the prior support with an invariant distribution aligning with the posterior distribution of interest. Consequently, upon convergence, the MCMC algorithm generates samples representative of this target distribution, thereby facilitating computations regarding model parameters and their associated uncertainties [Gelman et al., 1997, Liu and Liu, 2001]. However, the implementation of MCMC necessitates a large number of samples to satisfy convergence criteria.

While Bayesian inference stands as a powerful tool, the presence of insufficient measurements can pose significant challenges in solving inverse problems or lead to unreliable solutions [Woodbury and Rubin, 2000, Bohling and Butler Jr, 2010]. In the context of land subsidence, conventional monitoring techniques such as monitoring wells, spirit leveling, and extensometers are costly and thus spatially sparse. As a result, the measurements obtained through these methods are often inadequate in reducing the uncertainty of aquifer properties, especially for heterogeneous sedimentary basins [Galloway and Burbey, 2011].

Recent advancements in remote sensing technologies, particularly Interferometric Synthetic Aperture Radar (InSAR), have significantly enhanced data acquisition in terms of land displacements. InSAR leverages radar signals from satellites orbiting Earth to conduct high-density measurements across extensive areas, capturing alterations in land-surface elevation with high measurement accuracy [Hooper, 2008, Crosetto et al., 2016, Bonì et al., 2017]. Moreover, its cost-effectiveness significantly increases accessibility compared to other conventional monitoring techniques. The potential of InSAR technique in aquifer characterization has been recognized since the early 2000s [Hoffmann et al., 2003]. Since then, considerable efforts have been directed towards incorporating InSAR measurements into hydrogeological property characterizations, in particular hydromechanical properties i.e., skeletal storativity, specific storage, and compressibility [Hoffmann et al., 2003, Bell et al., 2008, Chaussard et al., 2014, Rezaei and Mousavi, 2019, Peng et al., 2022]. These investigations assume purely elastic vertical deformation and derive the properties using one-dimensional (1D) analytical

equations. Subsequently, the spatial distribution of properties is obtained by interpolating derived values.

Nevertheless, there are many obstacles to overcome when incorporating satellite-derived measurement into Bayesian inference. This requires a proper poroelastic model that links the observed surface deformation to groundwater flow in the aquifer. However, finding solutions to such models, which are governed by partial differential equations, can be time-consuming, making the implementation of Markov chain Monte Carlo (MCMC) methods infeasible.

For low-dimensional inverse problems, particularly those disregarding the heterogeneity of the aquifer, meta-modeling techniques offer a viable solution to address computational challenges. A meta-model (also known as a surrogate model or proxy model) is a computationally cheaper model designed to provide reasonably accurate approximations of solutions obtained from computationally intensive models, such as poroelastic models. Due to their efficiency, surrogates can be used for different purposes, not only Bayesian inference but also sensitivity analysis, optimization, etc. There are a wide variety of techniques for constructing surrogates, and the choice of the technique depends on factors including the forward model, intended purposes, and desired level of accuracy [Razavi et al., 2012, Asher et al., 2015, Bhosekar and Ierapetritou, 2018].

In this thesis work, a sparse-grid Bayesian framework is developed to characterize the hydraulic conductivity and the soil compressibility of a homogeneous aquifer system, utilizing piezometric records and InSAR surface displacement measurements. This framework is based on a three-dimensional (3D) coupled poroelastic model developed by Nardean et al. [2021], which allows for delineating associated processes within a variably saturated aquifer where porosity changes associated with effective stress variation are explicitly computed and accounted for. Sparse grid collocation is employed to construct a cheap surrogate of the coupled poroelastic model. This method involves polynomial approximation through a linear combination of Lagrangian interpolants, which are constructed over a series of tensor grids, each containing only a few points. The aggregate of these tensor grids forms what is known as the sparse grid [Piazzola and Tamellini, 2023a]. The use of sparse grid collocation enables the characterization of the parameter posterior distribution via MCMC at a feasible cost.

However, aquifer properties often display significant heterogeneity over

large scales, especially hydraulic conductivity, which can vary spatially by several orders of magnitude. Addressing such high-dimensional inverse problems is particularly challenging due to the exponential growth of the parameter dimensionality and the complex solutions of large-scale partial difference equations. Accordingly, the integration of InSAR measurements and poroelastic model to inform aquifer heterogeneity remains at a preliminary stage, with only a few attempts [Iglesias and McLaughlin, 2012, Hesse and Stadler, 2014, Alghamdi et al., 2020, 2021]. In these studies, the primary goal was to compute the maximum a posteriori (MAP) estimate. Therefore, the poroelastic inverse problems were formulated as large-scale optimization problems. Alghamdi et al. [2021] further exploited the low-rank structure of the Hessian matrix to identify the low-dimensional manifolds that can efficiently represent the high-dimensional posterior distribution, making MCMC implementation possible. Nevertheless, the complexity and computational cost of running extensive inversion make implementation prohibitive for many practical applications.

Alternatively, this thesis proposes an iterative procedure to characterize heterogeneous properties within a confined aquifer system. Each iteration begins with a 3D groundwater (GW) model, where hydraulic conductivity is calibrated based on piezometric records. The GW model solution, namely the evolution of the hydraulic head, along with displacement measurements acquired from InSAR, are then imported into the Terzaghi one-dimensional (1D) consolidation equation to estimate the specific storage. These analytical solutions serve as the 'observations'. Essentially, the specific storage is characterized by a Gaussian field, following which the spatial distribution can be estimated via the Kriging method according to the spatial correlation between 'observed' and unknown points. Finally, the interpolation results, including the mean and variance are incorporated into the GW model to update hydraulic conductivity and hydraulic head.

When it comes to land subsidence, existing numerical models are generally sufficient to capture the underlying mechanisms [Teatini et al., 2005, Janna et al., 2012, Ye et al., 2016]. In contrast, the mechanism causing earth fissures, i.e. discontinuous displacements, is markedly more complex and challenging to simulate, as highlighted in previous studies [Budhu, 2011, Hernandez-Marin and Burbey, 2010, Ochoa-González et al., 2018]. Different hydrogeological settings favoring the occurrence of earth fissures have been conceptualized based on field studies, including buried undulating bedrock,

pre-existing fault, and abrupt heterogeneous thickness of aquifer [Sheng and Helm, 1998, Sheng et al., 2003]. The features of the earth fissures such as density, shape, length, aperture, depth, and dislocation vary greatly in different settings, which also implies different driving mechanisms.

This thesis specifically aims to improve the understanding of the earth fissure mechanism with the presence of buried bedrock ridges crossing subsiding basins. Knowledge of the mechanisms driving these hazards is useful to predict and therefore mitigate significant damages to buildings, streets, highways, railroads, earth dams, water wells, and other engineering structures. Earth fissures that coincide with fault scarps and abrupt thickness change may be related to seismicity [Carreón-Freyre et al., 2016, Peng et al., 2013], but this is beyond the scope of this thesis.

Modeling the behavior of earth fissures requires a deep understanding of contact mechanics and various numerical methods were developed to delineate the physics of this problem [Hernandez-Marin and Burbey, 2010, Liu et al., 2019, Wang et al., 2015]. The finite element-interface element (FE-IE) numerical method developed by Franceschini et al. [2016] is a prominent approach that exhibits stable and accurate performances on quantifying fissure characteristics [Franceschini et al., 2019, Frigo et al., 2019, Ye et al., 2018, Li et al., 2021]. Therefore, it is adopted to simulate the fissuring process in a subsiding basin with buried bedrock ridges.

Despite addressing model inadequacies through the FE-IE numerical method, uncertainties stemming from various sources such as geologic configuration, pore-pressure distribution, hydrogeological, and geomechanical parameters persist [Frigo et al., 2019, Sheng et al., 2003]. In this context, a global sensitivity analysis is fundamental to evaluate the susceptibility of input variables to fissure formation and propagation, considering their possible mutual interactions [Iooss and Le Maître, 2015, Saltelli and Annoni, 2010]. A variance-based global sensitivity analysis is employed based on the functional decomposition of the output variance, providing the Sobol' indices that quantify the input contribution to the output variance [Sobol', 1993, 2001].

Typically, Sobol' indices are computed using the Monte Carlo method, which requires a large number of samples to achieve convergence. To mitigate the associated computational costs, two strategies are employed here, that is, an efficient Monte Carlo sampling design and surrogate models. Here, the Sobol' sequence is specifically utilized due to its ability to generate uniformly

distributed samples across the input parameter space, resulting in faster convergence compared to conventional Monte Carlo algorithms [Sobol' et al., 2011]. On the other hand, cheap surrogate models are commonly utilized for sensitivity analysis by substituting expensive computational models as mentioned earlier. Among surrogate modeling techniques, polynomial chaos expansion (PCE) exploits orthogonal polynomial projections of the input parameters to construct the stochastic model output [Ghanem and Spanos, 1991]. Furthermore, PCE offers a straightforward means to derive Sobol' indices from polynomial coefficients [Crestaux et al., 2009]. Benefiting from these advantages, PCE surrogates have widely been applied in environmental modeling for global sensitivity analysis. [Ciriello et al., 2013, Couaillier and Savin, 2019, Friedman et al., 2021, Sochala and Le Maître, 2013, Kaintura et al., 2018, Zoccarato et al., 2020].

However, compromised approximations may rise when the quantity of interest (QoI) presents some discontinuities concerning the input parameters [Sochala and Le Maître, 2013, Le Maître et al., 2004]. In case of earth fissuring simulation, this issue can manifest as the discontinuity develops within the continuous porous medium. To mitigate this issue, a decision tree-based method, the gradient boosting tree (GBT), is adopted. GBT uses an ensemble of decision trees to approximate the solution, particularly for nonlinear models with arbitrary inputs [Friedman, 2001, Louppe, 2014]. Although tree-based models are considered "black box" methods, various interpretation methods, such as Shapley Additive Explanations and Mean Decrease Accuracy (MDA), have been designed to assess feature importance according to their relevance for the corresponding estimator, similarly to the key insights of global sensitivity analysis [Arabameri et al., 2022, Breiman, 2001, Carvalho et al., 2019, Lundberg and Lee, 2017].

This thesis is organized in five chapters, as follows:

- **Chapter 2** presents the mathematical representations of the methodologies utilized within this dissertation. Initially, it displays the governing partial differential equations that characterize the processes of interest, such as groundwater flow and soil deformation due to pore pressure variation. Subsequently, the chapter introduces four distinct meta-modeling approaches designed to approximate these numerical solutions. Thereafter, it describes the basics of different sensitivity analysis techniques. Concluding this chapter is the delineation of the general Bayesian framework.

- **Chapter 3** demonstrates the Alto Guadalentín Basin case as the application of the proposed sparse-grid Bayesian framework. The chapter provides an overview of this Spanish region and available InSAR measurements, with a description of the setup of the coupled poroelastic model and surrogate models. Thereafter, it presents how the Bayesian framework quantifies the uncertainty associated to hydraulic conductivity and soil compressibility using piezometric records and InSAR datasets. Finally, it illustrates the numerical outcomes with the MAP estimate and provides a comparison between numerical outcomes and the observations.

- **Chapter 4** introduces an iterative approach to characterize heterogeneous aquifer properties. The effectiveness is illustrated by estimating the spatial distribution of specific storage in the confined aquifer system of the Gediz River Basin in Turkey. The chapter presents an overview of the study area, followed by an explanation of the numerical modeling approach utilized to simulate the hydrologic and geomechanical behavior of the region, as well as the details of implementing Kriging. Thereafter, the incorporation of the estimated specific storage distribution into a 3D bi-elastic geomechanical model enables the comparison between the simulated land subsidence rates and the actual InSAR-derived subsidence data.

- **Chapter 5** investigates the discontinuous mechanical behaviors, specifically earth fissures. The effectiveness of the geomechanical and earth fissure model is demonstrated by reproducing the evolution of three earth fissures documented in Guangming, China. Subsequently, the real-world test is simplified to an ideal test. In this context, three distinct global sensitivity analyses are conducted to assess the influence of various hydrogeologic parameters on the behaviors of tensile fissures. The outcomes indicate the conditions in favor of activating earth fissure. The comparison of these methodologies highlights their respective strengths and weaknesses.

- **Chapter 6** concludes the thesis by emphasizing the major outcomes and discussing expectations from future developments.

Chapter 2

Methods

This chapter describes the main mathematical and statistical approaches in this thesis work. The first part of the chapter is dedicated to reviewing the governing equations used to simulate the physical processes of interest, namely the continuous and discontinuous displacement fields affecting over-exploited aquifer systems. The second part focuses on the methods implemented to address the uncertainty quantification associated with the physical properties of an aquifer system within the modeling framework.

2.1 Mathematical Models

The mathematical representations of groundwater flow dynamics, soil mechanics, and contact mechanics are provided in this section. These formulations enable a comprehensive description of the physical processes investigated in the subsequent case studies.

2.1.1 Groundwater Flow (GW) Model

Assuming no sources or sinks of moisture within an unsaturated aquifer, the conservation equation for the water phase reads [Bear, 1979]:

$$\frac{\partial}{\partial t}(\rho_w S_w \phi) + \nabla \cdot (\rho_w \boldsymbol{q}) = 0 \tag{2.1}$$

where ρ_w is the water density, S_w the saturation degree, and ϕ the soil porosity. $\boldsymbol{q}$ is the water specific discharge that can be derived by the equation

of motion, i.e. Darcy's law:

$$\boldsymbol{q} = -k_r \boldsymbol{K} \nabla H \tag{2.2}$$

where k_r is the relative permeability, $\boldsymbol{K}$ is the saturated hydraulic conductivity tensor, and $H = \psi + z$ the hydraulic head, with ψ the pore pressure head and z elevation of the point of interest. As the gradient of ρ_w is negligible in relatively shallow depths, we can assume that the following equation holds:

$$\nabla \cdot (\rho_w \boldsymbol{q}) = \rho_w \nabla \cdot \boldsymbol{q} = -\rho_w \nabla \cdot (k_r \boldsymbol{K} \nabla H) \tag{2.3}$$

The first term of Eq. 2.1 can be written as:

$$\begin{aligned} \frac{\partial}{\partial t}(\rho_w S_w \phi) &= \rho_w \phi \frac{\partial S_w}{\partial t} + S_w \frac{\partial (\rho_w \phi)}{\partial t} \\ &= \rho_w \phi \frac{\partial S_w}{\partial t} + S_w \rho_w (\frac{\phi}{\rho_w} \frac{\partial \rho_w}{\partial p_w} + \frac{\partial \phi}{\partial p_w}) \frac{\partial p_w}{\partial t} \end{aligned} \tag{2.4}$$

where $p_w = \rho_w g \psi$ is the pore pressure with g gravity acceleration. Introducing the definitions of water compressibility β and oedometric bulk compressibility c_m:

$$\begin{aligned} \beta &= \frac{1}{\rho_w} \frac{\partial \rho_w}{\partial p} \\ c_m &= -\frac{1}{1-\phi} \frac{\partial (1-\phi)}{\partial p} = \frac{1}{1-\phi} \frac{\partial \phi}{\partial p} \end{aligned} \tag{2.5}$$

Eq. 2.1 can be expressed as [Bear, 1979]:

$$\phi \frac{\partial S_w}{\partial t} + S_w S_s \frac{\partial \psi}{\partial t} = \nabla \cdot (k_r \boldsymbol{K} \nabla (\psi + z)) \tag{2.6}$$

with $S_s = \rho_w g (\phi \beta + (1-\phi) c_m)$ the specific elastic storage. Eq. 2.6 describes the groundwater flow in porous media.

S_w and k_r are functions of the pore pressure head ψ. These constitutive relationships were investigated by several authors, among which we refer to [Van Genuchten and Nielsen, 1985]:

$$S_e(\psi) = \begin{cases} [(1 + (\alpha \psi)^n]^{-m} & \psi < 0 \\ 1 & \psi \geq 0 \end{cases} \tag{2.7}$$

where $S_e = \frac{S_w - S_{wr}}{1 - S_{wr}}$ is the effective saturation degree, with S_{wr} the irreducible water saturation, α is proportional to the inverse of the entry pressure, n

is a fitting parameter related to the pore size distribution, and $m = 1 - \frac{1}{n}$. Commonly, n in the range $[1.25, 6]$ [Paniconi and Putti, 1994]. The relative permeability k_r can be represented as [Van Genuchten and Nielsen, 1985]:

$$k_r(S_e) = \begin{cases} \sqrt{S_e}\left[1 - \left(1 - S_e^{\frac{1}{m}}\right)^m\right]^2 & \psi < 0 \\ 1 & \psi \geq 0 \end{cases} \tag{2.8}$$

Following Wang [2000] and Coussy [2004], in poroelastic problems the effect of deformation on the hydraulic behavior of a porous medium can be characterized by relating the soil porosity ϕ to the displacement field $\mathbf{u}$ and ψ:

$$\phi(\mathbf{u}, p_w) = \phi_0 + \alpha_p \nabla \cdot (\mathbf{u} - \mathbf{u}_0) + \frac{1}{M}(p_w - p_{w,0}) \tag{2.9}$$

where the subscript 0 refers to the initial state, $\alpha_p = 1 - \frac{c_r}{c_m}$ is the Biot coefficient, with c_r the volumetric compressibility of grains, and M is the Biot modulus that is set to infinity for incompressible grains and water.

The variably saturated flow in a deforming porous medium can be obtained by introducing Eq. 2.9 into Eq. 2.6 [Nardean et al., 2021]:

$$\left(\phi_0 \frac{\partial S_w}{\partial \psi} + \frac{\rho_w g S_w}{M}\right)\frac{\partial \psi}{\partial t} + \alpha_p S_w \frac{\partial \nabla \cdot \mathbf{u}}{\partial t} = \nabla \cdot k_r \mathbf{K} \nabla(\psi + z) \tag{2.10}$$

where the products between the variable parts of ϕ and the derivative of S_w are neglected.

2.1.2 Geomechanical Model

The displacement $\mathbf{u}$ of the solid grains can be obtained by prescribing the equilibrium condition for the porous medium :

$$\mathbf{div}\boldsymbol{\sigma} = \mathbf{0} \tag{2.11}$$

where $\boldsymbol{\sigma}$ is the total Cauchy stress tensor. According to Terzaghi-Bishop's principle, $\boldsymbol{\sigma}$ can be readily computed by subtracting the pore water pressure p_w from the effective stress tensor $\hat{\boldsymbol{\sigma}}$ [Bishop, 1960, Lewis and Schrefler, 1982],

$$\boldsymbol{\sigma} = \hat{\boldsymbol{\sigma}} - \alpha_p \chi p_w \mathbf{1} \approx \hat{\boldsymbol{\sigma}} - \alpha_p S_w p_w \mathbf{1} \tag{2.12}$$

where χ is the Bishop parameter, which is approximately equal to saturation degree S_w, and $\mathbf{1}$ is the rank-2 identity tensor. The pore pressure $p_w = \rho_w g \psi$ originates from the groundwater model described in the previous section.

The effective stress tensor $\hat{\boldsymbol{\sigma}}$ is a function of the mechanical constitutive law characterizing the soil behavior and displacement $\mathbf{u}$:

$$\begin{aligned} \hat{\boldsymbol{\sigma}} &= \mathbf{C} : \boldsymbol{\epsilon} \\ \boldsymbol{\epsilon} &= \nabla^s \mathbf{u} \end{aligned} \tag{2.13}$$

where $\mathbf{C}$ is the rank-4 elasticity tensor, $\boldsymbol{\epsilon}$ the strain tensor, and $\nabla^s = \frac{1}{2}(\nabla + \nabla^T)$ the symmetric gradient operator. Here we restrict our attention to isotropic elastic materials, and the representation of Eq. 2.13 in Voigt notation is as follows:

$$\hat{\boldsymbol{\sigma}} = c_m^{-1} \boldsymbol{D} \boldsymbol{\epsilon} \tag{2.14}$$

where $\boldsymbol{D}$ is expressed by:

$$\boldsymbol{D} = \begin{bmatrix} 1 & \frac{\nu}{1-\nu} & \frac{\nu}{1-\nu} & 0 & 0 & 0 \\ \frac{\nu}{1-\nu} & 1 & \frac{\nu}{1-\nu} & 0 & 0 & 0 \\ \frac{\nu}{1-\nu} & \frac{\nu}{1-\nu} & 1 & 0 & 0 & 0 \\ 0 & 0 & 0 & \frac{1-2\nu}{2(1-\nu)} & 0 & 0 \\ 0 & 0 & 0 & 0 & \frac{1-2\nu}{2(1-\nu)} & 0 \\ 0 & 0 & 0 & 0 & 0 & \frac{1-2\nu}{2(1-\nu)} \end{bmatrix} \tag{2.15}$$

with ν the Poisson' s ratio.

In the analyses conducted within the framework of this thesis work, c_m is characterized by a bi-linear (piece-wise) function that depends on the maximum vertical stress $\sigma_{z,max}$ experienced by soils, commonly known as the preconsolidation pressure,

$$c_m = \begin{cases} a, & \text{if} \quad \sigma_z \geq \sigma_{z,max} \text{ loading} \\ ra, & \text{if} \quad \sigma_z < \sigma_{z,max} \text{ unloading/reloading} \end{cases} \tag{2.16}$$

where a is a constant and r is a multiplicative factor. In the following case studies, r is set equal to 0.2, which is a common value for medium-depth aquifer systems [Teatini et al., 2011b]. This enables the model to represent the mechanical hysteresis of a porous medium under fluctuating pore pressure conditions, where deformation may partially recover.

2.1.3 Earth Fissure Model

To include discontinuities into continuum mechanics, such as the geomechanical model, earth fissures are conceptualized mathematically as pairs of friction surfaces embedded within the continuous domain Ω and conform to some constraints, such as the normal contact requirement, ensuring that the two surfaces do not interpenetrate or overlap along the normal direction. As long as they adhere to the normal contact requirement, the discontinuity remains stuck (or inactive). The discontinuity activates once the stress state reaches a failure condition, causing the two surfaces that move differently.

The discrete fracture model proposed by Karimi-Fard et al. [2003] and Garipov et al. [2016] is used in the modelling approach used in this thesis to simulate contact mechanics. Furthermore, we take advantage of the model implementation developed in Franceschini et al. [2016] and Franceschini et al. [2019], where the fracture network is discretized by interface elements (IEs), which are zero-thickness FEs with shape functions compatible with those of the surrounding FEs.

A fissure is viewed as a boundary Γ_f within Ω, and is made of two opposed surfaces Γ_f^1 and Γ_f^2, where the imposed contact conditions allow for a relative displacement (opening and sliding) between corresponding points whenever the stress state violates the selected failure criterion. More specifically, the classical Mohr-Coulomb framework is employed as the failure criterion, which enforces the following condition on Γ_f^1 and Γ_f^2:

$$f(\mathbf{t}) = \|\mathbf{t}_T\|_2 - (c - t_N \tan(\varphi)) \leq 0 \tag{2.17}$$

where $\mathbf{t} = \boldsymbol{\sigma} \cdot \mathbf{n}$ is the contact stress, with $\mathbf{t}_T = \mathbf{t} - t_N \mathbf{n}$ and $t_N = \mathbf{t} \cdot \mathbf{n}$ the tangential and normal components, respectively. $\mathbf{n}$ denotes the unit vector normal to the surface pair Γ_f^1 and Γ_f^2. In the Coulomb criterion, c and φ are the cohesion and the friction angle, respectively. The impenetrability of solid bodies is prescribed by the normal contact condition:

$$t_N g_N = 0 \tag{2.18}$$

where $g_N = \mathbf{g} \cdot \mathbf{n}$ is the normal component of $\mathbf{g}$, and $[[\mathbf{u}]]$ represents the relative displacement between Γ_f^1 and Γ_f^2, which is defined as:

$$\mathbf{g} = g_N \mathbf{n} + \mathbf{g}_T = [[\mathbf{u}]] = \mathbf{u}|_{\Gamma_f^1} - \mathbf{u}|_{\Gamma_f^2} \tag{2.19}$$

where $\mathbf{u}$ is the global displacement in Ω, as consistently computed through Eq. (2.13), and the subscript Γ_f^i refers to the corresponding surfaces. Taking

into account the friction law (Eq. (2.17)) and the principle of impenetrability of solid bodies (Eq. (2.18)), the inner boundary Γ_f can be subdivided into three portions:

1. $f < 0$ and $t_N < 0$: the fissure is in a stick state, namely the discontinuity is fully deactivated and acts as a part of the continuum;

2. $f = 0$ and $t_N < 0$: the fissure is in a slip state, where a slippage is freely allowed under a fixed tangential traction $\tau_{max} = c - t_N \tan(\varphi)$;

3. $t_N = 0$: the fissure is in an open state, i.e. both opening and slip displacements are freely allowed with zero traction.

The main challenge to finding the solution in terms of $\mathbf{u}$ and $\mathbf{t}$ lies in identifying the stick, slip, and open portions of the fissure surfaces. Although the maximum extent of the fissure is restricted to the whole surface discretized through IEs, tracking the evolution of the three different states while adhering to the updating constraints during the simulation proves challenging and makes the modelling approach nonlinear. Details about the discretization and solution strategy can be found in Franceschini et al. [2016] and Franceschini et al. [2019].

2.2 Uncertainty Quantification (UQ)

In this work, uncertainty quantification involves uncertainty propagation, parameter calibration based on Bayesian inversion, and sensitivity analysis. All these analyses are based on sampling-based methods such as the Monte Carlo (MC) technique. Given the complexity of the computational models, the MC computational burden can be prohibitively expensive. Four meta-modeling methods are proposed to address this issue by generating inexpensive proxies for the original computational model, enabling the subsequent uncertainty quantification analyses to be more cost-effective. The section is organized as follows: firstly, the four meta-modeling methods are presented, followed by the corresponding sensitivity analysis techniques. Finally, we introduce the Bayesian scheme for inferring the parameters of interest.

2.2.1 Meta-modeling

The following meta-modeling approaches are described in the following:

- sparse grid collocation,
- polynomial chaos expansion,
- gradient boost tree,
- Kriging.

The first three approaches are used to approximate a random variable, whereas Kriging provides a mean to model the realizations of a Gaussian process. Let us denote the input uncertain parameters by $\boldsymbol{x} = [x_1, \dots, x_N]$ to be independent random variables and denote their image space by $\Xi = \prod_{n=1}^{N} \Xi_n \subset \mathbb{R}^N$, with $\Xi_n \subset \mathbb{R}$. The associated joint probability density function (pdf) is the so-called prior pdf $\pi_{\text{prior}}(\boldsymbol{x}) = \prod_{n=1}^{N} \pi_n(x_n)$, where π_n is the pdf associated with x_n. Further, let us regard the numerical models introduced in the previous section as parametric maps from the input parameters to the output model. More precisely, let us consider a random space-time point $(\boldsymbol{y}, t)_i = (\boldsymbol{y}_i, t_i)$, $\boldsymbol{y}_i \in \Omega$ and $t_i \in \mathcal{T}$. We denote the mapping between input parameter $\boldsymbol{x}$ and the corresponding model solution as follows,

$$\mathcal{M} : \Xi \to \mathbb{R},\ \boldsymbol{x} \mapsto \mathcal{M}(\boldsymbol{y}_i, t_i, \boldsymbol{x}), \quad i = 1, \dots, M \tag{2.20}$$

that associates parameter values to an output derived from the model solution. For the sake of notation, we write $\mathcal{M}_i(\boldsymbol{x}) := \mathcal{M}(\boldsymbol{y}_i, t_i, \boldsymbol{x})$. In the following, we sequentially introduce three surrogate models for the approximation of the original model (2.20) by constructing a map,

$$\widehat{\mathcal{M}} : \Xi \to \mathbb{R},\ \boldsymbol{x} \mapsto \widehat{\mathcal{M}}(\boldsymbol{x}), \quad \text{such that} \quad \widehat{\mathcal{M}}(\boldsymbol{x}) \approx \mathcal{M}(\boldsymbol{x}). \tag{2.21}$$

Sparse Grid Collocation

In broad terms, a sparse-grids-based model is a polynomial approximation obtained as a linear combination of Lagrangian interpolants constructed over a series of tensor grids, each of them consisting of a small number of points. The union of the employed tensor grids is a sparse grid [Bungartz and Griebel, 2004, Babuška et al., 2007, Xiu and Hesthaven, 2005].

As a first step, let us introduce the set of univariate interpolation knots scattered over the parameter space Ξ determined by the prior distribution.

The number of knots along each variable x_n is denoted by $K_n \in \mathbb{N}_+$:

$$K_n = f(i_n) = 2(i_n - 1) + 1 \tag{2.22}$$

where $i_n \in \mathbb{N}_+$ is the interpolation level and the *"level to knots function"* is denoted by $f : \mathbb{N}_+ \to \mathbb{N}_+$. The choices of i_n and f depend on the accuracy of the approximation and the distribution of $\boldsymbol{x}$. In particular, a *2-step level to knots function* is utilized in conjunction with symmetric Leja knots to produce nested collocation knots from both uniform and normal distributions [De Marchi, 2004, Narayan and Jakeman, 2014]. Such that the set of interpolation knots along x_n can be expressed by,

$$\mathcal{T}_{n,i_n} = \{x^{j_n}_{n,f(i_n)},\ j_n = 1, \ldots, f(i_n)\}, \quad \text{for } n = 1, \ldots, N \tag{2.23}$$

while the set of interpolation knots over the entire parameters space is the tensor product of $\mathcal{T}_{n,i_n}$, and it can be denoted as $\mathcal{T}_{\mathbf{i}} = \bigotimes_{n=1}^{N} \mathcal{T}_{n,i_n}$, with a multi-index $\mathbf{i} = [i_1, \ldots, i_n] \in \mathbb{N}_+^N$,

$$\mathcal{T}_{\mathbf{i}} = \left\{ \boldsymbol{x}^{\,\mathbf{j}}_{f(\mathbf{i})} \right\}_{\mathbf{j} \le f(\mathbf{i})}, \text{ with } \boldsymbol{x}^{\,\mathbf{j}}_{f(\mathbf{i})} = \left\{ x^{j_1}_{1,f(i_1)}, \ldots, x^{j_N}_{N,f(i_N)} \right\} \text{ and } \mathbf{j} \in \mathbb{N}_+^N, \tag{2.24}$$

where $f(\mathbf{i}) = [f(i_1), f(i_2), \ldots, f(i_N)]$ and $\mathbf{j} \le f(\mathbf{i})$ means $j_n \le f(i_n)$ for $\forall n \in [1, \ldots, N]$. A tensor grid approximation of $\mathcal{M}(\boldsymbol{x})$ is obtained by global Lagrangian interpolation over the collocation knots on the sparse grid and can be written as follows,

$$\mathcal{M}(\boldsymbol{x}) \approx \mathcal{M}_{\mathbf{i}}(\boldsymbol{x}) = \sum_{\mathbf{j} \le f(\mathbf{i})} \mathcal{M}\left(\boldsymbol{x}^{\,\mathbf{j}}_{f(\mathbf{i})}\right) \mathcal{L}^{\,\mathbf{j}}_{f(\mathbf{i})}(\boldsymbol{x}), \tag{2.25}$$

where $\left\{ \mathcal{L}^{\,\mathbf{j}}_{f(\mathbf{i})}(\boldsymbol{x}) \right\}_{\mathbf{j} \le f(\mathbf{i})}$ are N-variate Lagrange basis polynomials based on the tensor product of univariate Lagrange polynomials,

$$\mathcal{L}^{\,\mathbf{j}}_{f(\mathbf{i})}(\boldsymbol{x}) = \prod_{n=1}^{N} l^{\,j_n}_{n,f(i_n)}(x_n), \quad \text{with } \ l^{\,j_n}_{n,f(i_n)}(x_n) = \prod_{k=1, k \ne j_n}^{f(i_n)} \frac{x_n - x^{\,k}_{n,f(i_n)}}{x^{\,k}_{n,f(i_n)} - x^{\,j_n}_{n,f(i_n)}} \tag{2.26}$$

Moreover, the approximation of the integral, i.e. the quadrature of $\mathcal{M}(\boldsymbol{x})$,

can be represented followed by the tensor product of univariate integral rules,

$$\begin{aligned}\mathcal{Q}_{\mathbf{i}} = \int_{\mathbf{\Gamma}} \mathcal{M}_{\mathbf{i}}(\boldsymbol{x})\pi(\boldsymbol{x})d\boldsymbol{x} &= \sum_{\mathbf{j}\leq f(\mathbf{i})} \mathcal{M}\Big(\boldsymbol{x}^{\mathbf{j}}_{f(\mathbf{i})}\Big)\Big(\prod_{n=1}^{N}\int_{\Gamma_n} l^{j_n}_{n,f(i_n)}(x_n)\pi(x_n)dx_n\Big) \\ &= \sum_{\mathbf{j}\leq f(\mathbf{i})} \mathcal{M}\Big(\boldsymbol{x}^{\mathbf{j}}_{f(\mathbf{i})}\Big)\Big(\prod_{n=1}^{N}\omega^{j_n}_{n,f(i_n)}\Big) \\ &= \sum_{\mathbf{j}\leq f(\mathbf{i})} \mathcal{M}\Big(\boldsymbol{x}^{\mathbf{j}}_{f(\mathbf{i})}\Big)\omega^{\boldsymbol{j}}_{f(\boldsymbol{i})}\end{aligned} \tag{2.27}$$

where $\omega^{j_n}_{n,f(i_n)}$ are the standard quadrature weights computed by the integrals of the corresponding univariate Lagrange polynomials. Clearly, the approximation and the quadrature calculations entail realizations of $\mathcal{M}$ on the full sparse grid $\mathcal{T}_{\mathbf{i}}$, or all collocation knots, i.e., $\prod_{n=1}^{N} f(i_n)$. The overall cost grows exponentially with N, known as the curse of dimension. Despite a moderate N, any big component i_n can lead to huge costs. To circumvent this issue, the full sparse grid approximation $\mathcal{M}_{\mathbf{i}}$ is further decomposed into a linear combination of coarse $\mathcal{M}_{\mathbf{h}}$ with $\mathbf{h} \leq \mathbf{i}$. For a better understanding, we start with decomposing an univariate:

$$\Delta_n[\mathcal{M}_{\mathbf{i}}] = \mathcal{M}_{\mathbf{i}} - \mathcal{M}_{\mathbf{i}-\mathbf{e}_i} \quad \text{with} \;\; 1 \leq n \leq N \tag{2.28}$$

where $\mathbf{e}_n$ is the n-th canonical multi-index, i.e., $(\mathbf{e}_n)_k = 1$ if $n = k$ and 0 otherwise. The decomposed form of multivariates simply applied the tensor product to Eq. 2.28,

$$\mathbf{\Delta}_n[\mathcal{M}_{\mathbf{i}}] = \bigotimes_{n=1}^{N} \Delta_n[\mathcal{M}_{\mathbf{i}}] = \sum_{\mathbf{j}\in\{0,1\}^N} (-1)^{\|\mathbf{j}\|_1}\mathcal{M}_{\mathbf{i}-\mathbf{j}} \tag{2.29}$$

where $\|\mathbf{j}\|_1 := \sum_{n=1}^{N} \|j_n\|$. And summing up the decomposed terms can gain,

$$\mathcal{M}_{\mathbf{i}} = \sum_{\mathbf{h}\leq\mathbf{i}} \mathbf{\Delta}[\mathcal{M}_{\mathbf{h}}] \tag{2.30}$$

As an example, a case with $\mathbf{i} = [2, 2]$ is illustrated,

$$\begin{aligned}\sum_{[h_1,h_2]\leq[2,2]} \mathbf{\Delta}[\mathcal{M}_{\mathbf{h}}] &= \mathbf{\Delta}[\mathcal{M}_{[1,1]}] + \mathbf{\Delta}[\mathcal{M}_{[1,2]} + \mathbf{\Delta}[\mathcal{M}_{[2,1]}] + \mathbf{\Delta}[\mathcal{M}_{[2,2]}] \\ &= \mathcal{M}_{[1,1]} + (\mathcal{M}_{[1,2]} - \mathcal{M}_{[1,1]}) + (\mathcal{M}_{[2,1]} - \mathcal{M}_{[1,1]}) \\ &\quad + (\mathcal{M}_{[2,2]} - \mathcal{M}_{[2,1]} - \mathcal{M}_{[1,2]} + \mathcal{M}_{[1,1]}) \\ &= \mathcal{M}_{[2,2]}\end{aligned} \tag{2.31}$$

If the original model $\mathcal{M}(\boldsymbol{x})$ satisfies some regularity assumptions, it's said that not all the hierarchical decomposition $\boldsymbol{\Delta}\mathcal{M}_{\mathbf{h}}$ contributes equally. Roughly speaking, the terms with large $\|\mathbf{h}\|_1$ are relatively smaller than others. For this reason, these terms can be dropped, and the approximation remains good accuracy Bungartz and Griebel [2004]. Following the above example and assuming $\|\mathbf{h}\|_1 \leq 3$, the approximation turns to,

$$\begin{aligned}\mathcal{M}_{\ [2,2]} \approx \sum_{q_1+q_2\leq 3} \boldsymbol{\Delta}[\mathcal{M}_{[h_1,h_2]}] &= \boldsymbol{\Delta}[\mathcal{M}_{[1,1]}] + \boldsymbol{\Delta}[\mathcal{M}_{[1,2]}] + \boldsymbol{\Delta}[\mathcal{M}_{[2,1]}] \\ &= -\mathcal{M}_{[1,1]} + \mathcal{M}_{[1,2]} + \mathcal{M}_{[2,1]}\end{aligned}$$

In this way, the computation cost can be considerably reduced because these higher-order sparse grid evaluations are the most costly. Such that Eq. 2.29 can be written as Wasilkowski and Wozniakowski [1995],

$$\begin{aligned}\mathcal{M}_{\mathbf{i}}(\boldsymbol{x}) \approx \mathcal{M}_{\mathcal{I}}(\boldsymbol{x}) = \sum_{\mathbf{i}\in\mathcal{I}} \boldsymbol{\Delta}[\mathcal{M}_{\mathbf{i}}(\boldsymbol{x})] = \sum_{\mathbf{i}\in\mathcal{I}} c_{\mathbf{i}}\mathcal{M}_{\mathbf{i}} \\ \text{with} \quad c_{\mathbf{i}} := \sum_{\substack{\mathbf{j}\in\{0,1\}^N \\ \mathbf{i}+\mathbf{j}\in\mathcal{I}}} (-1)^{\|\mathbf{j}\|_1}\end{aligned} \tag{2.32}$$

The same holds for the quadrature computation:

$$\mathcal{Q}_{\mathbf{i}}(\boldsymbol{x}) \approx \mathcal{Q}_{\mathcal{I}}(\boldsymbol{x}) = \sum_{\mathbf{i}\in\mathcal{I}} \boldsymbol{\Delta}[\mathcal{Q}_{\mathbf{i}}(\boldsymbol{x})] = \sum_{\mathbf{i}\in\mathcal{I}} c_{\mathbf{i}}\mathcal{Q}_{\mathbf{i}} \tag{2.33}$$

Eqs.2.32 and 2.33 are valid only if the multi-index set $\mathcal{I}$ is a downward closed set. A common choice of $\mathcal{I}$ is

$$\mathcal{I} = \{\mathbf{i} \subset \mathbb{N}_+^N : \sum_{n=1}^{N} g_n(i_n - 1) \leq w\} \tag{2.34}$$

where the level of approximation w is an integer, g_n is the anisotropic weight, a parameter used to adjust the shape of multi-index set, which allows for placing more collocation knots along the directions deemed to be more important.

Polynomial Chaos Expansion

Polynomial chaos expansion (PCE) is also a powerful meta-modeling technique aimed at providing a functional approximation of a computational

model output through its spectral representation on a suitably constructed basis of polynomial functions.

Since any random variable can be represented as a series of polynomials in independent variables [Wiener, 1938], the expansion of $\mathcal{M}(\boldsymbol{x})$ can be generalized as:

$$\mathcal{M}(\boldsymbol{x}) \approx \widehat{\mathcal{M}_p}(\boldsymbol{x}) = \sum_{\boldsymbol{\alpha} \in \mathbb{N}^N} c_{\boldsymbol{\alpha}} \Phi_{\boldsymbol{\alpha}}(\boldsymbol{x}) \tag{2.35}$$

where $\Phi_{\boldsymbol{\alpha}}(\boldsymbol{x})$ are multivariate polynomials orthogonal and normalized with respect to the joint pdf $\pi(\boldsymbol{x})$, $\boldsymbol{\alpha} = (\alpha_1, ..., \alpha_N) \in \mathbb{N}_0^N$ is a multi-index that denotes the components of the multivariate polynomial $\Phi_{\boldsymbol{\alpha}}(\boldsymbol{x})$, and $c_{\boldsymbol{\alpha}}$ are the corresponding coefficients. To realize Eq. 2.35, firstly it is needed to build the polynomial basis $\Phi_{\boldsymbol{\alpha}}(\boldsymbol{x})$ and subsequently compute $c_{\boldsymbol{\alpha}}$.

The polynomial basis $\Phi_{\boldsymbol{\alpha}}(\boldsymbol{x})$ is built from a set of univariate random ortho-normal polynomials $\phi_k(y_n)$ satisfying the orthogonality conditions [Xiu, 2007]:

$$\mathbb{E}[\phi_s(x_n)\phi_r(x_n)] = \int_{\Gamma_n} \phi_s(x_n)\phi_r(x_n)\pi(x_n)dx_n = \delta_{s,r} \tag{2.36}$$

where n denotes the index of input variable, s and r represent the corresponding degree of the polynomial family. $\delta_{s,r}$ is the Kronecker delta function and Γ_n is the support of x_n. The choice of orthogonal polynomials also relies on the distribution of the variable $\pi(x_n)$. In the multivariate case, the polynomial basis functions $\Phi_{\boldsymbol{\alpha}}(\boldsymbol{x})$ are products of the univariate orthogonal polynomials:

$$\Phi_{\boldsymbol{\alpha}}(\boldsymbol{x}) = \prod_{n=1}^{N} \phi_{\alpha_n}(x_n) \tag{2.37}$$

By the extension of Eq. 2.36, the multivariate basis is also ortho-normal:

$$\mathbb{E}[\Phi_{\boldsymbol{\alpha}}(\boldsymbol{x})\Phi_{\boldsymbol{\beta}}(\boldsymbol{x})] = \int_{\boldsymbol{\Gamma}} \Phi_{\boldsymbol{\alpha}}(\boldsymbol{x})\Phi_{\boldsymbol{\beta}}(\boldsymbol{x})\pi(\boldsymbol{x})d\boldsymbol{x} = \delta_{\boldsymbol{\alpha}\boldsymbol{\beta}} \tag{2.38}$$

In practice, Eq. 2.35 must be truncated with a finite set of polynomials based on various schemes. A straightforward approach is to limit the total degree to be less than or equal to p. The truncated PCE then becomes:

$$\mathcal{M}(\boldsymbol{x}) \approx \widehat{\mathcal{M}_p}(\boldsymbol{x}) = \sum_{\mathcal{A}} c_{\boldsymbol{\alpha}} \Phi_{\boldsymbol{\alpha}}(\boldsymbol{x}) \quad \text{with} \quad \mathcal{A} = \{\boldsymbol{\alpha} \in \mathbb{N}^N : |\boldsymbol{\alpha}| \leq p\} \tag{2.39}$$

with $|\boldsymbol{\alpha}| = \alpha_1 + \alpha_2 + \ldots + \alpha_N$. The coefficients $c_{\boldsymbol{\alpha}}$ can be computed with projection methods that use the orthogonality of the basis functions. By the

definitions of Eqs. 2.35 and 2.36, $c_{\boldsymbol{\alpha}}$ is equal to:

$$c_{\boldsymbol{\alpha}} = \mathbb{E}[\Phi_{\boldsymbol{\alpha}} \cdot \mathcal{M}(\boldsymbol{x})] \tag{2.40}$$

The calculation of expectation is a numerical integration problem that can be solved by Gaussian quadrature as presented in Eq. 2.27,

$$c_{\boldsymbol{\alpha}} = \int_{\boldsymbol{\Gamma}} \mathcal{M}(\boldsymbol{x})\Phi_{\boldsymbol{\alpha}}\pi(\boldsymbol{x})d\boldsymbol{x} \approx \sum_{i=1}^{M} \omega^{(i)}\mathcal{M}(\boldsymbol{x}^{(i)})\Phi_{\boldsymbol{\alpha}}(\boldsymbol{x}^{(i)}) \tag{2.41}$$

with $M = \binom{N+p}{p}$ the cardinality of the set $\mathcal{A}$. $\boldsymbol{x}^{(i)}$ are the integration points and the weight $\omega^{(i)}$ are its integrals derived from Eq. 2.27. In fact, sparse grid collocation is commonly used to compute the coefficients in the PCE context [Formaggia et al., 2013].

Gradient Boost Tree

In contrast to the previous two meta-modeling methods, the gradient boost tree (GBT) approach does not necessitate the regularity of $\mathcal{M}(\boldsymbol{x})$, making it suitable for discontinuous problems [Friedman, 2001]. The approximation obtained by GBT $\widehat{\mathcal{M}_t}(\boldsymbol{x})$ is based on an ensemble of base learners (e.g., weak basic models) properly chosen to minimize the average value of a specified loss function $\mathcal{L}(\mathcal{M}(\boldsymbol{x}), \widehat{\mathcal{M}_t}(\boldsymbol{x}))$, i.e.:

$$\widehat{\mathcal{M}_t}(\boldsymbol{x}) = \arg\min_{\widehat{\mathcal{M}_t}(\boldsymbol{x})} \mathbb{E}[\mathcal{L}(\mathcal{M}(\boldsymbol{x}), \widehat{\mathcal{M}_t}(\boldsymbol{x}))] \tag{2.42}$$

Similar to the previous two methods, the gradient boosting algorithm assumes $\mathcal{M}(\boldsymbol{x})$ to be in the form of a weighted sum of basic functions:

$$\mathcal{M}(\boldsymbol{x}) \approx \widehat{\mathcal{M}_t}(\boldsymbol{x}) = \sum_{m=0}^{M} \beta_m h_m(\boldsymbol{x}) \tag{2.43}$$

where M is the total boosting stage, β_m are the expansion coefficients, and $h_m(\boldsymbol{x})$ is the base learner at m-th stage.

In particular, GBT uses the decision tree as the base learner, such that $h_m(\boldsymbol{x})$ can be written as:

$$h_m(\boldsymbol{x}) = \sum_{i=1}^{I_m} b_{im}\mathbf{1}_{R_{im}} \tag{2.44}$$

where I_m refers to the number of leaves at stage m, the subscript im denotes the i-th leaf at the m-th stage, and b is the corresponding predicted value of the terminal region R_{im}. The indicator function $\mathbf{1}_{R_{im}}$ takes value 1 if $\boldsymbol{x}$ lies in the subset R_{im} otherwise is set to be 0.

Here, the loss function is taken in the form of mean squared error to facilitate the computation. Then, gradient descend algorithm is applied to fit $h_m(\boldsymbol{x})$ to the pseudo-residuals r_{jm} with the training set$\{(\boldsymbol{x}^{(j)}, \mathcal{M}(\boldsymbol{x}^{(j)}))\}_{j=1}^{J}$, i.e., intermediate error terms at the m-th stage, for the j-th sample point $(\boldsymbol{x}^{(j)}, r_{jm})$:

$$\mathcal{L}_j = \frac{1}{2}(\mathcal{M}(\boldsymbol{x}^{(j)}) - \widehat{\mathcal{M}}_{m-1}(\boldsymbol{x}^{(j)}))^2 \tag{2.45}$$

$$r_{jm} = -\frac{\partial \mathcal{L}_j}{\partial \widehat{\mathcal{M}}_{m-1}} = \mathcal{M}(\boldsymbol{x}^{(j)}) - \widehat{\mathcal{M}}_{m-1}(\boldsymbol{x}^{(j)}) \tag{2.46}$$

Afterward, the coefficient β_m can be optimized:

$$\beta_m = \arg\min_{\beta} \sum_{j=1}^{J} [\mathcal{M}(\boldsymbol{x}^{(j)}) - (\widehat{\mathcal{M}}_{m-1}(\boldsymbol{x}^{(j)}) + \beta h_m(\boldsymbol{x}^{(j)}))] \tag{2.47}$$

and the model can be updated by:

$$\widehat{\mathcal{M}}_m(\boldsymbol{x}) = \widehat{\mathcal{M}}_{m-1}(\boldsymbol{x}) + \beta_m h_m(\boldsymbol{x}) \tag{2.48}$$

Usually, some constraints are imposed on the fitting procedure by regularization methods to prevent overfitting, a common error in machine learning where the model performs extremely well on the training data but fails to fit unseen data. For example, the maximum stage of gradient boosting M in Eq. 2.43 is a natural regularization parameter that discourages learning a more complex model to avoid overfitting. Since the regularization through shrinkage provides superior results to that obtained by restricting the maximum stage [Copas, 1983], a simple shrinkage strategy is also added to Eq. 2.48:

$$\widehat{\mathcal{M}}_m(\boldsymbol{x}) = \widehat{\mathcal{M}}_{m-1}(\boldsymbol{x}) + \nu \beta_m h_m(\boldsymbol{x}) \tag{2.49}$$

Under this form, two regularization parameters are used in the gradient boosting algorithm, i.e., the learning rate ν and the number of boosting stage M.

Kriging Method

So far, we have introduced three meta-modeling methods for approximating a random variable, which can characterize a spatially homogeneous aquifer property. In contrast, Kriging is a geostatistical interpolation method used to estimate values at unmeasured points based on neighboring observed points [Matheron, 1963].

Before introducing Kriging, some basic overviews of a random field are provided. Given a random spatial coordinate in the topological space $\boldsymbol{y} \in \mathcal{D}_Y \subset \mathbb{R}^d$, the associate state variable Z can be expressed as a random variable $Z(\boldsymbol{y})$. The set of these random variables is known as a random field $Z(\boldsymbol{y}, s) : \mathcal{D}_Y \times S \to \mathbb{R}$, with s being an outcome in the sample space S. Random fields can be divided into different types according to the following properties:

1. The distribution of $Z(\boldsymbol{y}_1, ..., \boldsymbol{y}_n)$ is jointly Gaussian for any $(\boldsymbol{y}_1, ..., \boldsymbol{y}_n)$ and any $n \in \mathbb{N}$. This implies that Z is a Gaussian random field, or a Gaussian process, which is fully characterized by its mean function and covariance function, as expressed by:

$$\mathbb{E}[Z(\boldsymbol{y}, s)] = \int_S Z(\boldsymbol{y}, s) d\pi(s) \tag{2.50}$$

$$C(\boldsymbol{y}_1, \boldsymbol{y}_2) = \mathrm{Cov}[Z(\boldsymbol{y}_1, s), Z(\boldsymbol{y}_2, s)] \tag{2.51}$$

   The variance function is defined as $\mathrm{Var}(\boldsymbol{y}_1) = C(\boldsymbol{y}_1, \boldsymbol{y}_1)$. Moreover, the correlation function is defined as,

$$R(\boldsymbol{y}_1, \boldsymbol{y}_2) = \frac{C(\boldsymbol{y}_1, \boldsymbol{y}_2)}{\sigma(\boldsymbol{y}_1)\sigma(\boldsymbol{y}_2)} \tag{2.52}$$

   where $\sigma(\boldsymbol{y})$ is the standard deviation function of the random field.

2. The statistical properties of a random field, such as the mean and variance, remain invariant under translation, a property known as stationarity. In other words, the statistical properties are consistent and identical at every location within the field.

3. If the covariance only depends on $\boldsymbol{y}_1 - \boldsymbol{y}_2$, a random field is considered weak-sense stationary. Moreover, a weak stationary random field is isotropic if the dependence is solely restricted to $\|\boldsymbol{y}_1 - \boldsymbol{y}_2\|$.

Kriging is a stochastic algorithm that assumes the model output $\mathcal{M}(\boldsymbol{y})$ is a realization of a Gaussian process, which can be represented as [Santner et al., 2003, Kleijnen, 2009]:

$$\mathcal{M}^K(\boldsymbol{y}) = \boldsymbol{\beta}^T \boldsymbol{f}(\boldsymbol{y}) + \sigma^2 Z(\boldsymbol{y}, s) \tag{2.53}$$

The term $\boldsymbol{\beta}^T \boldsymbol{f}(\boldsymbol{y})$ is the mean value of the Gaussian process, known as the trend function. This trend function consists of arbitrary functions $\{f_j; j = 1, \ldots, P\}$, each multiplied by corresponding coefficients $\{\beta_j; j = 1, \ldots, P\}$. The second term represents the variance of the Gaussian process, denoted by σ^2. A stationary Gaussian process $Z(\boldsymbol{y}, s)$ is characterized by a zero-mean and a unit-variance.

It is useful to predict the value Z for a new point $\boldsymbol{y}$ given the existing measurements and their correlations. Consider a experimental design $\mathcal{Y} = \{\boldsymbol{y}^{(1)}, \ldots, \boldsymbol{y}^{(M)}\}$ and the corresponding measurements $\mathcal{Z} = \{Z(\boldsymbol{y}^{(1)}), \ldots, Z(\boldsymbol{y}^{(M)})\}$, which may be subject to noise $\boldsymbol{\varepsilon}$:

$$Z^{(i)} = \mathcal{M}(\boldsymbol{y}^{(i)}) + \varepsilon^{(i)} \quad i = 1, \ldots, M \tag{2.54}$$

Usually, $\boldsymbol{\varepsilon} = [\varepsilon_1, \ldots, \varepsilon_M]$ is assumed to follow a zero mean Gaussian distribution:

$$\boldsymbol{\varepsilon} \sim \mathcal{N}(\mathbf{0}, \boldsymbol{\Sigma}) \tag{2.55}$$

where $\boldsymbol{\Sigma}$ represents the covariance matrix of the noise, which is often in the form of a diagonal covariance matrix $\boldsymbol{\Sigma} = \sigma_\varepsilon^2 \boldsymbol{I}_M$, with $\boldsymbol{I}$ the identity matrix of dimension $M \times M$. This implies that the noise is independent and identically Gaussian distributed.

The joint Gaussian distribution formed by the predicted value $\hat{Z}(\boldsymbol{y})$ and the observed measurements reads:

$$\begin{Bmatrix} \hat{Z}(\boldsymbol{y}) \\ \mathcal{Z} \end{Bmatrix} \sim \mathcal{N}_{M+1}\left(\begin{Bmatrix} \boldsymbol{f}^T(\boldsymbol{y})\boldsymbol{\beta} \\ \boldsymbol{F}\boldsymbol{\beta} \end{Bmatrix}, \begin{Bmatrix} \sigma^2 & \sigma^2 \boldsymbol{r}^T(\boldsymbol{y}) \\ \sigma^2 \boldsymbol{r}(\boldsymbol{y}) & \sigma^2 \boldsymbol{R} + \sigma_\varepsilon^2 \boldsymbol{I}_M \end{Bmatrix} \right) \tag{2.56}$$

where:

1. $\boldsymbol{F}$ is the observation (design) matrix in terms of the trend, which can be expressed as:

$$F_{ij} = f_j\big(\boldsymbol{y}^{(i)}\big), \quad i = 1, \ldots, M; \; j = 0, \ldots, P. \tag{2.57}$$

2. $\boldsymbol{r}(\boldsymbol{y})$ is the vector of cross-correlations between the prediction point $\boldsymbol{y}$ and each one of the observations, whose elements read:

$$r_i = R\Big(\boldsymbol{y}, \boldsymbol{y}^{(i)}; \boldsymbol{\theta}\Big),\ i = 1, \ldots, M \tag{2.58}$$

where $\boldsymbol{\theta}$ is a hyperparameter characterizing the correlation between two points.

3. $\boldsymbol{R}$ is the correlation matrix between the observed points, whose elements read:

$$R_{ij} = R\Big(\boldsymbol{y}^{(i)}, \boldsymbol{y}^{(j)}; \boldsymbol{\theta}\Big),\ i, j = 1, \ldots, M \tag{2.59}$$

The mean and variance of the Gaussian variable $\hat{Z}\,(\boldsymbol{y})$ can be conditioned on the observed data as follows [Santner et al., 2003, Dubourg, 2011]:

$$\mu_{\hat{Z}}(\boldsymbol{y}) = \boldsymbol{f}(\boldsymbol{y})^T\hat{\boldsymbol{\beta}} + \boldsymbol{c}(\boldsymbol{y})^T\boldsymbol{C}^{-1}(\mathcal{Z} - \boldsymbol{F}\hat{\boldsymbol{\beta}}) \tag{2.60}$$

$$\sigma^2_{\hat{Z}}(\boldsymbol{y}) = \big(\sigma^2 - \boldsymbol{c}^T(\boldsymbol{y})\boldsymbol{C}^{-1}\boldsymbol{c}(\boldsymbol{y}) + \boldsymbol{s}^T(\boldsymbol{y})(\boldsymbol{F}^T\boldsymbol{C}^{-1}\boldsymbol{F})^{-1}\boldsymbol{s}(\boldsymbol{y})\big) \tag{2.61}$$

The following substitutions are introduced in Eq. 2.60 for a clearer representation:

$$\begin{aligned} \boldsymbol{c}(\boldsymbol{y}) &= \sigma^2\boldsymbol{r}(\boldsymbol{y}) \\ \boldsymbol{C} &= \sigma^2\boldsymbol{R} + \sigma^2_{\varepsilon}\boldsymbol{I}_M \end{aligned} \tag{2.62}$$

together with the coefficients derived from the generalized least-square method:

$$\hat{\boldsymbol{\beta}} = (\boldsymbol{F}^T\boldsymbol{C}^{-1}\boldsymbol{F})^{-1}\boldsymbol{F}^T\boldsymbol{C}^{-1}\mathcal{Z} \tag{2.63}$$

and,

$$\boldsymbol{s}(\boldsymbol{y}) = \boldsymbol{F}^T\boldsymbol{C}^{-1}\boldsymbol{c}(\boldsymbol{y}) - \boldsymbol{f}(\boldsymbol{y}) \tag{2.64}$$

In practice, the selections of the trend function and correlation function are entailed to form a Kriging predictor. The type of trend function is set to be ordinary which implies a constant mean β_0 across the entire field. The Matern 5/2 correlation function is used as it performs consistently well across different problem types with smooth (i.e. not noisy) data [Kianifar and Campean, 2020]:

$$R(y, y'; \theta) = \left(1 + \sqrt{5}\frac{|y - y'|}{\theta} + \frac{5}{3}\Big(\frac{|y - y'|}{\theta}\Big)^2\right)\exp\Big[-\sqrt{5}\frac{|y - y'|}{\theta}\Big] \tag{2.65}$$

When the dimension of $\boldsymbol{y}$ is larger than one, a multi-dimensional correlation function can be constructed from a uni-variate correlation function:

$$R(\boldsymbol{y}, \boldsymbol{y}'; \theta) = R(h), \quad h = \left[\sum_{i=1}^{d} \left(\frac{y_i - y_i'}{\theta_i}\right)\right] \tag{2.66}$$

In cases where hyperparameters $\boldsymbol{\theta}$ are unknown, they need to be estimated based on available observations, along with other unknowns such as the constant mean β_0 and the noise variance σ_ε^2. To this end, a leave-one-out (LOO) cross-validation method is employed to set up the optimization problem. Specifically, the set of observations $\mathcal{Z}$ excluding the i-th observed value, denoted as $\mathcal{Z}\backslash Z_i$, is used to form the Kriging predictor. The corresponding error in estimating Z_i can be expressed as:

$$\epsilon_i = \left(Z_i - \mu_{\hat{Z}}\left(\boldsymbol{y}_i, \boldsymbol{\beta}, \sigma_\varepsilon^2, \boldsymbol{\theta}, \mathcal{Z}\backslash Z_i\right)\right)^2 \tag{2.67}$$

and the optimal values can be obtained by minimizing the overall LOO error:

$$\{\boldsymbol{\beta}, \boldsymbol{\theta}, \sigma_\varepsilon^2\} = \arg\min_{\boldsymbol{\beta}, \boldsymbol{\theta}, \sigma_\varepsilon^2} \frac{1}{N} \sum_{n=1}^{N} \epsilon_i \tag{2.68}$$

The optimization problem is solved by a hybrid approach, where the final solutions obtained from the Genetic Algorithm serve as the initial trial for the gradient-based method.

2.2.2 Sensitivity Analysis

Sensitivity analysis aims to evaluate the effects of variations in input parameters on model outcomes. Consequently, the results of the analysis can identify the most influential input variables and offer insights into the relationships and dependencies among the inputs and outputs. As mentioned earlier, sensitivity analysis is typically conducted by utilizing surrogates of the computational model. It is worth noting that we only focus on model outcomes characterized by independent random variables rather than random fields.

Variance-based Sobol' indices

Sobol' indices are based on the idea of defining the computational model's expansion into summands of increasing dimension, such that the total variance of the model can be expressed in terms of the sum of the variances of

the summands. Assume f to be a square-integrable function of independent variables $\boldsymbol{x} = [x_i, \ldots, x_N]$, then the Sobol' functional decomposition scheme reads:

$$f(\boldsymbol{x}) = f_0 + \sum_{i=1}^{N} f_i(x_i) + \sum_{1 \le i < j \le N}^{N} f_{ij}(x_i, x_j) + \ldots + f_{12\ldots N}(x_1, x_2, \ldots, x_N) \tag{2.69}$$

where the following conditions hold for these terms:

$$f_0 = \mathbb{E}[f(\boldsymbol{x})] = \int f(\boldsymbol{x})\pi(\boldsymbol{x})d\boldsymbol{x} \tag{2.70}$$

$$\int f_{1,\ldots,s}(x_1, \ldots, x_s)\pi(x_1, \ldots, x_s)dx_k = 0, \quad 1 \le k \le s \tag{2.71}$$

The terms in the decomposition may be derived by:

$$\begin{aligned} f_i &= \mathbb{E}_{\boldsymbol{x}_{\sim i}}[f(\boldsymbol{x})] - f_0 \\ f_{ij} &= \mathbb{E}_{\boldsymbol{x}_{\sim (ij)}}[f(\boldsymbol{x})] - f_i - f_j - f_0 \end{aligned} \tag{2.72}$$

where $\boldsymbol{x}_{\sim i} = (x_1, \ldots, x_{i-1}, x_{i+1}, \ldots, x_N)$ denotes all elements of $\boldsymbol{x}$ except the i-th one. The same calculation applies to higher-degree terms.

The decomposition scheme allows us to attribute the variances to the different variables or their various degree interactions. These can be given by the partial variances:

$$V_{1,\ldots,s} = \int \cdots \int f^2_{x_1,\ldots,x_s}(x_1, \ldots, x_s)\pi(x_1, \ldots, x_s)dx_1 \ldots dx_s, \quad 1 \le s \le N \tag{2.73}$$

and similarly for higher-order terms. With the help of the partial variances, the total variance can be decomposed as follows:

$$V = \sum_{i=1}^{N} V_i + \sum_{1 \le i < j \le N}^{N} V_{ij} + \ldots + V_{12\ldots N} \tag{2.74}$$

The variance-based sensitivity is described by the ratio of the partial variances and the total variance. The first and second-order Sobol' indices are defined as:

$$\begin{aligned} S_i &= \frac{V_i}{V} \\ S_{ij} &= \frac{V_{ij}}{V} \end{aligned} \tag{2.75}$$

and similarly for the higher-order sensitivity indices. The first order indices $\{S_i\}_{i=1}^N$ measure the effect on the output variance contributed from input variable x_i alone. Higher-order indices represent the combined effect of the group of corresponding variables on the variance of the model output.

Another common sensitivity measure is the total index of the i-th variable:

$$\begin{aligned} S_{T_i} &= \sum_{\{1,\dots,s\}\supset i} S_{1,\dots,s} \\ S_{T_i} &= 1 - S_{\boldsymbol{x}\sim i} \end{aligned} \tag{2.76}$$

such that S_{T_i} accounts for the contribution to the output variance from all the terms that contain the variable x_i. In practice, the calculation usually takes the second form by excluding the variable x_i:

$$S_{\boldsymbol{x}\sim i} = \frac{\mathrm{Var}(\mathbb{E}[u|\boldsymbol{x}_{\sim i}])}{\mathrm{Var}(u)} \tag{2.77}$$

where $u = f(\boldsymbol{x} = f(\boldsymbol{x}_i, \boldsymbol{x}_{\sim i}))$. This index accounts for the sum of all the single effects as well as interactions between the variables $\boldsymbol{x}_{\sim i}$.

These Sobol' indices can be calculated by Monte Carlo methods [Saltelli, 2002, Saltelli and Annoni, 2010]. The procedure implies the generation of a $q \times 2N$ sample matrix of the input variables $\boldsymbol{x}$. The first N columns are gathered as matrix $\mathbf{A}$ and the second N columns are used similarly as matrix $\mathbf{B}$. From these two matrices, we generate N further $q \times N$ matrices ${\mathbf{A}_\mathbf{B}}^i$ by taking matrix $\mathbf{A}$ and replacing its i-th column with the corresponding column of $\mathbf{B}$. The estimators:

$$\begin{aligned} V_i(\mathbb{E}_{\boldsymbol{x}\sim i}(u|x_i)) &\approx \frac{1}{q}\sum_{j=1}^{q} f(\mathbf{B})_j (f({\mathbf{A}_\mathbf{B}}^i)_j - f(\mathbf{A})_j) \\ \mathbb{E}_{\boldsymbol{x}\sim i}(V_{x_i}(u|\boldsymbol{x}_{\sim i})) &\approx \frac{1}{2q}\sum_{j=1}^{q} (f(\mathbf{A})_j - f({\mathbf{A}_\mathbf{B}}^i)_j)^2 \end{aligned} \tag{2.78}$$

used in Eqs. 2.75 and 2.76 allows us to compute the indices S_i and S_{T_i}.

The main problem with this sampling-based method is the cost of computing $f({\mathbf{A}_\mathbf{B}}^i)$. Except for the use of surrogate models, the computational cost can be further reduced by decreasing the number of model evaluations. To this end, we substitute the ordinary Monte Carlo with the Sobol' sequence [Saltelli, 2002, Saltelli and Annoni, 2010], in which the design points

are selected with low discrepancy sequences, thus improving the convergence of the estimator.

Alternatively, PCE can be utilized with the Sobol' indices computed analytically without using the sampling-based approximation given in Eq. (2.78). Due to the orthogonality condition, the mean and the total variance of the PCE can be directly computed from the coefficients of the expansion as follows:

$$\mathbb{E}(f(\boldsymbol{x})) \approx c_{\boldsymbol{\alpha}}|_{|\boldsymbol{\alpha}|=0}, \tag{2.79}$$

$$V \approx \sum_{0<|\alpha|\leq N} c_{\alpha}^2 \gamma_{\boldsymbol{\alpha}}. \tag{2.80}$$

According to Sudret [2008], if we introduce the set of $\boldsymbol{\alpha}$ tuples $\mathcal{J}_{i_1,\ldots,i_s}$ such way that only the indices $(i_1,\ldots,i_s)$ are nonzero:

$$\mathcal{J}_{i_1,\ldots,i_s} = \left\{ \boldsymbol{\alpha} : \begin{array}{llll} \alpha_k > 0 & \forall k = 1,\ldots,N, & k \in (i_1,\ldots,i_s) \\ \alpha_j = 0 & \forall j = 1,\ldots,N, & j \notin (i_1,\ldots,i_s) \end{array} \right\}, \tag{2.81}$$

than $\mathcal{J}_i$ is defined as a set of all multi-indices that correspond to the polynomials depending only on parameter x_i.

Consequently, the Sobol' decomposition (see Eq. (2.69)) of the PCE approximation is straightforward:

$$f(\boldsymbol{x}) = f_0 + \sum_{i=1}^{n} \sum_{\boldsymbol{\alpha}\in\mathcal{J}_i} c_{\boldsymbol{\alpha}}\Phi_{\boldsymbol{\alpha}}(x_i) + \sum_{1\leq i_1<i_2\leq N} \sum_{\boldsymbol{\alpha}\in\mathcal{J}_{i_1,i_2}} c_{\boldsymbol{\alpha}}\Phi_{\boldsymbol{\alpha}}(x_{i_1},x_{i_2}) + \cdots + \sum_{\boldsymbol{\alpha}\in\mathcal{J}_{1,2,\ldots,N}} c_{\boldsymbol{\alpha}}\Phi_{\boldsymbol{\alpha}}(x_1,x_2,\ldots,x_N)$$

and thus any element of the decomposition can be written as:

$$f_{i_1,\ldots i_s} = \sum_{\boldsymbol{\alpha}\in\mathcal{J}_{i_1,\ldots,i_s}} c_{\boldsymbol{\alpha}}\Phi_{\boldsymbol{\alpha}}(x_{i_1},\ldots x_{i_s}) \tag{2.82}$$

The partial variances can be also easily computed from:

$$V_{i_1,\ldots i_s} = \sum_{\boldsymbol{\alpha}\in\mathcal{J}_{i_1,\ldots,i_s}} c_{\boldsymbol{\alpha}}^2 \gamma_{\boldsymbol{\alpha}} \tag{2.83}$$

that is, the coefficients corresponding to the polynomials that have dependence only on the selected variables have to be collected, squared, multiplied with its norm, and summed up. For the sensitivity index, this expression has to be divided by the total variance provided in Eq. (2.80).

Mean Decrease Accuracy (MDA)

Theoretically, GBT surrogates can be plugged into Eqs.2.78 for computing Sobol' indices. However, like other machine learning methods, GBT lacks interpretability, meaning the functional relationship between the input and output is not clear. Consequently, GBT and other tree-based methods are commonly associated with mean decrease accuracy (MDA), a sensitivity measure indicating how input variables contribute to the predictive performance of an estimator. Each feature importance is evaluated through a permutation-based measure following the idea of Breiman [2001] and the application in Jaxa-Rozen and Kwakkel [2018]. Moreover, unlike Sobol' indices, MDA can be applied to evaluate correlated input variables.

Given the $q \times N$ matrix $\mathbf{A}$ of the random input variables $\boldsymbol{x}$, the MDA index of the i-th feature measures the decrease of the estimator accuracy by randomly permuting the values of x_i (i-th column of input variables matrix) for K times in total and for each repetition re-computing the ensemble tree predictions with the k-th (for $k = 1, \ldots, K$) permuted column $\mathbf{A}_i$. The higher the inaccuracy, the more important the feature for the particular model. MDA of the i-th feature is defined as

$$\mathrm{MDA}_i = s - \frac{1}{K} \sum_{k=1}^{K} s_{k,i} \tag{2.84}$$

where s is the reference score and $s_{k,i}$ the score for the k-th permutation of feature x_i, where the score is obtained by computing the mean square error between predictions and observations. The feature is important if permuting its values causes a large drop in the model performance.

In the context of MC sampling, we introduce a convergence criterion proposed by Roustant et al. [2014] to evaluate the stability of the important indices. The vector $\boldsymbol{I}_q = (I_1, \ldots, I_N)$ of the variable importance indices is estimated from a sample size of q design points, where N is the number of input features. Specifically, the Euclidean norm of the vector is taken into account rather than the individual indices so that the more influential indices have more effect on the convergence measurement. The importance indices are computed sequentially over an increasing sample size at intervals of Δq. Then the convergence criterion k_q is computed by:

$$k_q = \frac{1/n_t \sum_{j=1}^{n_t} \|\boldsymbol{I}_q - \boldsymbol{I}_{q-j\Delta q}\|}{\|\boldsymbol{I}_q\|} \tag{2.85}$$

where $\| \ \|$ is the Euclidean norm and n_t is the number of total intervals. The values of Δq and n_t are case-dependent. This criterion will be imposed on the total Sobol' indices S_T and MDA.

Partial Dependence

So far, PCE and GBT surrogates have been introduced to compute their respective sensitivity measures, namelly Sobol' indices and MDA. Lastly, partial dependence is included to be incorporated with both PCE and GBT surrogates. Compared to Sobol' indices and MDA, partial dependence is more straightforward and analogous to one-at-a-time (OAT) sensitivity analysis, which assumes the model response is a function of one or two input variables and characterizes the average marginal effect on model prediction [Goldstein et al., 2015]. Owing to this feature, partial dependence plots can visually depict the relationship between model output and the parameters of interest. The partial dependence function $\overline{\mathcal{M}_i}$ reads:

$$\overline{\mathcal{M}_i}\left(\boldsymbol{x_i}\right) = \mathbb{E}_{\boldsymbol{x_j}}\left[\mathcal{M}\left(\boldsymbol{x_i}, \boldsymbol{x_j}\right)\right] = \int \mathcal{M}\left(\boldsymbol{x_i}, \boldsymbol{x_j}\right) d\pi\left(\boldsymbol{x_j}\right) \tag{2.86}$$

where $\boldsymbol{x_i}$ and $\boldsymbol{x_j}$ are respectively the feature set of interest and its complement used in the computational model $\mathcal{M}$. Generally, $\boldsymbol{x_i}$ is allowed to contain two components at most. Analogously, the computational model $\mathcal{M}$ in Eq. 2.86 can be substituted by its surrogates $\widehat{\mathcal{M}}$ and the expectation can be computed by Markovian samples.

2.2.3 Bayesian Inversion

In practical scenarios, critical input parameters such as hydraulic conductivity and compressibility typically remain elusive. One may turn to measurable quantities of interest (QoIs) that are inferable through the application of the computational model which maps these QoIs from the underlying input parameters. Consequently, we are interested in inferring plausible parameter values based on available data. This inverse problem can be tackled in the Bayesian framework, see e.g. Stuart [2010]. In this context, the goal is to derive a probability distribution of the parameters describing the plausibility of different parameter values given the information provided by the available data. The sought-after distribution is called data-informed or posterior

distribution and can be interpreted as an update of a prior parameter distribution, i.e. the distribution assumed for the parameters before incorporating information from data. We consider M independent measurements m_i of the QoI forming a set of data $\mathcal{O} = \{m_1, \cdots, m_M\}$. We assume that they correspond to the model outputs at the points $\{(\boldsymbol{y}_i, t_i)\}_{1=1}^{M}$ for an unknown value $\bar{\boldsymbol{x}} \in \Xi$ of the parameters and that they are affected by an error. We write

$$m_i = \mathcal{M}_i(\bar{\boldsymbol{x}}) + \varepsilon_i, \quad i = 1, \ldots, M, \tag{2.87}$$

where ε_i are independent and identically distributed Gaussian random variables representing the measurement errors, i.e. the discrepancy between the model response and the data. Similarly, we assume $\boldsymbol{\varepsilon} = [\varepsilon_1, \ldots, \varepsilon_M]$ to follow a joint normal distribution $\boldsymbol{\varepsilon} \sim \mathcal{N}(\mathbf{0}, \boldsymbol{\Sigma})$ with zero mean and diagonal covariance matrix $\boldsymbol{\Sigma} = \sigma_\varepsilon^2 I_M$, I_M being the identity matrix of dimension $M \times M$. Then, according to Bayes' theorem, the posterior probability density function (pdf) $\pi_{\text{post}}(\boldsymbol{x}|\mathcal{O})$ of $\boldsymbol{x}$ is obtained by:

$$\pi_{\text{post}}(\boldsymbol{x}|\mathcal{O}) = \frac{\pi_{\text{prior}}(\boldsymbol{x})\pi(\mathcal{O}|\boldsymbol{x})}{\pi(\mathcal{O})}, \tag{2.88}$$

where $\pi_{\text{prior}}(\boldsymbol{x})$ is the prior pdf of the parameters mentioned above, $\pi(\mathcal{O}|\boldsymbol{x})$ is the so-called likelihood function (denoted in the following by $\mathcal{L}(\boldsymbol{x}, \mathcal{O})$) which represents the probability of $\boldsymbol{x}$ given the set of measurements $\mathcal{O}$, and $\pi(\mathcal{O})$ is termed evidence or marginal likelihood and can be seen as a normalization constant. The posterior pdf is thus proportional to the product of the likelihood function and the prior distribution

$$\pi_{\text{post}}(\boldsymbol{x}) \propto \mathcal{L}(\boldsymbol{x}, \mathcal{O})\pi_{\text{prior}}(\boldsymbol{x}). \tag{2.89}$$

Since the errors ε_i, $i = 1, \ldots, M$ are assumed to be independent Gaussian random variables, the likelihood function can be written as follows

$$\mathcal{L}(\boldsymbol{x}, \mathcal{O}) = \prod_{i=1}^{M} \frac{1}{\sqrt{2\pi\sigma_\varepsilon^2}} \mathrm{e}^{-\frac{(m_i - \mathcal{M}_i(\boldsymbol{x}))^2}{2\sigma_\varepsilon^2}}. \tag{2.90}$$

However, in general, the variance σ_ε^2 of the measurement errors is not known and needs to be estimated according to the case study. One option is to relate the estimation of the variance to the *maximum a posteriori* (MAP) estimate, i.e. the estimate of the maximum point $\boldsymbol{x}^*$ of the posterior pdf (2.88) Carrera and Neuman [1986]. For computational reasons, it is common to turn the

maximization problem into a minimization one by introducing the so-called negative log-likelihood function (NLL) $\mathrm{NLL}(\boldsymbol{x}, \mathcal{O}) := -\ln(\mathcal{L}(\boldsymbol{x}, \mathcal{O}))$ that has the following form

$$\mathrm{NLL}(\boldsymbol{x}, \mathcal{O}) = \frac{1}{2\sigma_\varepsilon^2} \sum_{i=1}^{M} \big(m_i - \mathcal{M}_i(\boldsymbol{x})\big)^2 + \frac{1}{2} M \ln(2\pi\sigma_\varepsilon^2). \tag{2.91}$$

Then, the MAP estimate $\boldsymbol{x}^*$ is obtained by minimizing the negative logarithm of the right-hand side of Eq. 2.89:

$$\boldsymbol{x}^* := \arg\min_{\boldsymbol{x}\in\Xi} \big[-\ln(\pi_{post}(\boldsymbol{x}, \mathcal{O}))\big] = \arg\min_{\boldsymbol{x}\in\Xi} \big[\mathrm{NLL}(\boldsymbol{x}, \mathcal{O}) - \ln(\pi_{prior}(\boldsymbol{x}))\big]. \tag{2.92}$$

Note that the minimization is independent of σ_ε. Finally, the following sample variance estimation is employed

$$\sigma_\varepsilon^2 \approx \frac{1}{M} \sum_{i=1}^{M} \big(m_i - \mathcal{M}_i(\boldsymbol{x}^*)\big)^2. \tag{2.93}$$

In general, the form of the posterior pdf cannot be computed analytically and can be estimated by e.g. sampling techniques to obtain values of $\boldsymbol{x}$ distributed according to it. The class of methods to this aim are Markov Chain Monte Carlo methods (MCMC) that, roughly speaking, construct a sequence of random variables, where the current sample depends probabilistically on the previous one. In this work, we consider the slice sampling algorithm Neal [2003], which approximates the unnormalized posterior pdf, i.e. does not require calculating the normalization constant $\pi(\mathcal{O})$. Furthermore, with respect to other MCMC algorithms, it has the advantage of not requiring a proposal distribution that is usually difficult to tune and strongly affects the performance of the method. Commonly, the available data describe multiple QoIs associated with the model measured from various devices that are affected by different measurement errors (for instance, in this work we consider piezometric and InSAR measurements describing drawdown and average subsidence rate, respectively). One has then to group together measurements of the same type and extend the above-described procedure to the case of multiple sets of data. Let us consider N_g group of measurements, each consisting of M_g data, and denote them by $\mathcal{O}^{(g)}$ such that

$$\mathcal{O}^{(g)} = \{m_1^{(g)}, \ldots, m_{M_g}^{(g)}\}, \quad g = 1, \ldots, N_g.$$

Further, let us denote the error variance of each measurement group by $\sigma^2_{\varepsilon_g}$. The MAP estimation requires the following (extended) negative logarithm posterior function,

$$-\ln(\pi_{post})\big(\boldsymbol{x}, \bigcup_{g=1}^{N_g} \mathcal{O}^{(g)}\big) = \sum_{g=1}^{N_g} -\ln(\pi_{post})(\boldsymbol{x}, \mathcal{O}^{(g)}). \tag{2.94}$$

Since each term in the sum has a different weight $1/2\sigma^2\varepsilon_g$ (cf. Eq. (2.90)) the minimization is not variance-independent as above. Hence, the optimization has to be done over the parameter $\boldsymbol{x}$ and the variances $\sigma^2_{\varepsilon_g}$, $g = 1, \ldots, N_g$. We will give more details on this in the following Section 3.2.3 where two measurement variances were estimated. Finally, we observe that the computation cost associated with the computation of the MAP estimate and to sampling of the posterior pdf can be prohibitively expensive for calling for the computation model repeatedly. To overcome this issue, the original computational model is usually substituted by cheaper surrogate models.

2.3 Motivation

The thesis deals with the characterization of mechanical properties and mechanical response of complex aquifer systems to groundwater pumping. Each of the three case studies, namely the Alto Guadalentín in Spain, the Gediz Basin River in Turkey, and the Guangming village in China, requires the use of a specific physics-based numerical simulations to model the response of the aquifer system to groundwater extraction. With the aim of investigating the uncertainty characterizing the aquifer parameters, the computationally intensive modelling applications are substituted with more economical surrogates, allowing for sample-based statistical analyses at a reasonable cost.

In the case of the Alto Guadalentín basin, the phreatic aquifer system is characterized using a coupled poroelastic model, introducing nonlinearity corresponding to saturation and porosity variation. Moreover, the complexity of the discretization scheme exacerbates simulation costs. To mitigate this, sparse grid collocation is employed to accurately approximate numerical solutions with tens of interpolants. Using polynomial chaos expansion (PCE) indirectly necessitates employing the collocation technique to compute the coefficients of polynomials. In comparison, gradient boosted trees (GBT), as a machine learning technique, requires a sufficiently large sample size to ensure the performance of surrogates.

In the Gediz Basin River, the heterogeneous nature of specific storage of clay units, as suggested by the cross-comparison between the evolution of the hydraulic head and land subsidence, is mathematically represented by a Gaussian field. Thus, the Kriging method is utilized to estimate the spatial distribution of aquifer properties.

In the last section, one of goals is to assess how various factors influence earth fissure behaviors. Initially, Sobol' indices are used as a global sensitivity analysis method to fully explore the parameter space and compute high-order interactions. Apart from Monte Carlo estimation, Polynomial Chaos Expansion (PCE) serves as an alternative to compute Sobol' indices with fewer computational efforts. However, PCE is theoretically unsuitable for approximating discontinuous variables such as earth fissure opening or sliding. Therefore, Gradient Boosted Trees (GBT) are employed due to their proficiency in addressing discontinuities. Furthermore, Mean Decrease Accuracy (MDA) is performed, especially efficient for nonlinear or opaque estimators like GBT. Finally, Partial Dependence metrics offer a straightforward measure of sensitivity that can be integrated with any fitted surrogates.

In summary, the selection of meta-modeling techniques and sensitivity analysis methods is tailored to address the specific challenges of the problem at hand. In particular, the earth fissure output exhibits significant discontinuity, and hence different sensitivity measures and their corresponding surrogate techniques are adopted for cross-validation, ensuring the reliability of analyses.

2.4 Software Utilized

In this thesis, the forward groundwater flow and geomechanical models are carried out by the *FLOW3D* and *GEPS3D* simulators [Paniconi and Putti, 1994, Isotton et al., 2019, Nardean et al., 2021]. The Sobol' technique is implemented by the *SALib* library in Python environment [Herman and Usher, 2017]. *SALib* library [Zander, 2020, Friedman and Zander, 2020] is used to compute the polynomial chaos expansion and Sobol' indices [Vittek et al., 2006]. Gradient boosting tree algorithm and mean decrease accuracy computation are carried out by the *scikit-learn* module in Python with gradient boosting regression estimator and permutation feature importance function [Pedregosa et al., 2011]. The Bayesian parameter calibration was implemented in Matlab, using the *Sparse Grid Matlab Kit* [Piazzola and

Tamellini, 2023a,b] for the construction of the required sparse-grids-based surrogate models. The construction and estimation of Kriging model are carried out in *UQlab* [Lataniotis et al., 2022].

Chapter 3

Inference of Homogeneous Aquifer Properties affecting Land Subsidence

This chapter presents a novel methodology aimed at determining the basin-scale hydrogeomechanical properties of an over-exploited phreatic aquifer system experiencing significant land subsidence due to the extensive lowering of the water table. The approach involves utilizing a three-dimensional (3D) coupled non-linear poroelastic model. Soil deformation is explicitly used to quantify variations in porosity and their impact on variably-saturated groundwater flow. On the other hand, variations in pressure and water saturation influence soil deformation. The modelling approach is implemented within a Bayesian framework to infer the basin-scale hydrogeomechanical properties of the aquifer system. This framework utilizes Markov Chain Monte Carlo (MCMC) sampling algorithms, which are augmented by sparse grid-based surrogate models. Piezometric and Interferometric Synthetic Aperture Radar (InSAR) datasets provide measurements of hydraulic head variations and land displacement, which are utilized to infer the aquifer properties.

The methodology is applied to the Alto Guadalentín basin in Spain, an inner valley that has experienced land subsidence larger than 3 m in recent decades following a lowering of the water table

exceeding 100 m [Bonì et al., 2015, Ezquerro et al., 2017].

Initially, a brief overview of the study region is provided. Subsequently, the set-up of the coupled flow-poroelastic and surrogate models is presented, with a detailed description of how the Bayesian framework facilitates the estimation of parameters through the analysis of piezometric data and satellite records. Following these steps, the forward model is used to evaluate how uncertainties in input parameters influence output variability. A final comparison between the numerical solutions, derived using estimated parameters, and observations is carried out.

The proposed approach and the outcomes achieved are the basis of the publication entitled "Characterizing aquifer properties through surrogate-based Bayesian framework and InSAR measurements: A case study in the Alto Guadalentín Basin" by Li Y., Piazzola C., Zoccarato C., Bru-Cruz G., Tamellini L., Guardiola-Albert C. and Teatini P., submitted to *Water Resources Research*.

3.1 Study Area

The Alto Guadalentín Basin is an elongated tectonic depression-oriented NE-SW located in Southeast Spain, covering an approximate area of 300 km^2. The phreatic aquifer system consists primarily of Plio-Quaternary and Miocene sediments that fill the basin, limited by mountain fronts (Figure 3.1A). The ranges are controlled by large NE-SW faults [Martínez Díaz et al., 2012]. The Plio-Quaternary filling comprises two layers: a shallower clayey unit in the central part of the valley, characterized by high compressibility ("clay" in Figure 3.1B), and a lower unit consisting of coarser sandy soils and gravel, characterized by high permeability ("sand" in Figure 3.1B). For this reason, it is the main extraction layer [CHS, 2005].

The thickness and spatial distribution of the clay layer were delineated in the work of Béjar-Pizarro et al. [2016]. Beneath the Plio-Quaternary filling, the Miocene sediments comprise conglomerates, marl, and sandstones. Although some groundwater extraction occurred also from this deep unit, its permeability is considerably lower than that of the sandy layer [CHS, 1994, 2005]. The geometry of these layers was studied by Cerón-García [1995]

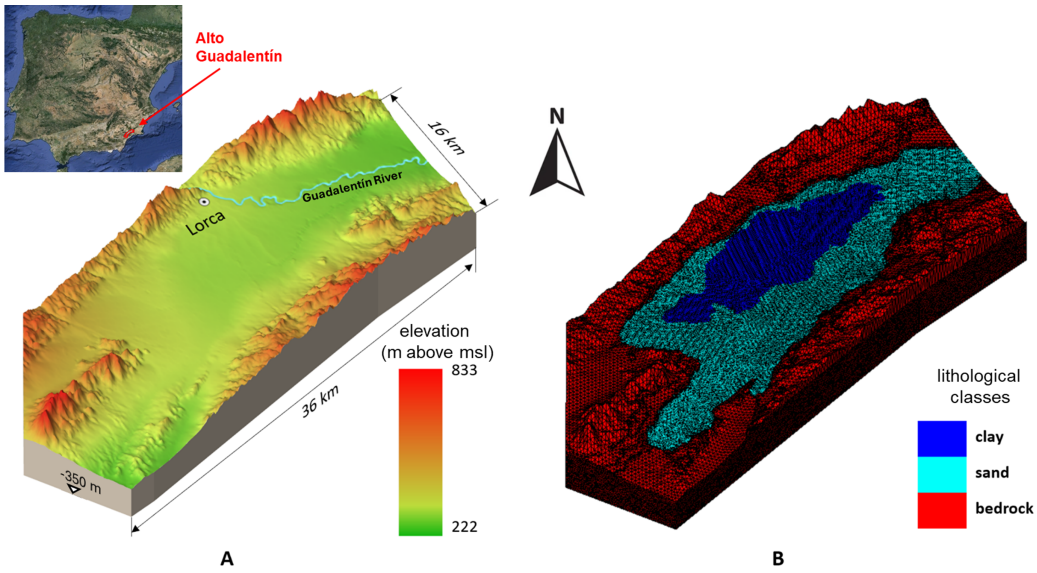

Figure 3.1: Axonometric views of: A) the 3D simulated domain with colors representative of the land elevation (m above msl); and B) the finite element discretization of the domain with colors representative of the main lithological classes.

through vertical electric soundings. Moreover, borehole information and lithostratigraphic data are available from the piezometric network of the Segura River Hydrographic Confederation (CHS) and technical reports [CHS, 2005]. The underlying basement consists of Paleozoic pre-orogenic metamorphic rocks exhibiting a horst and graben structure with depths varying between 400 to 1000 m [Cerón and Pulido-Bosch, 1996]. For the model developed in the present work, the Paleozoic and the lower Miocene layers are considered to barely participate in the hydraulic and mechanical activities of the upper layers. Figure 3.2 provides a few representative geological sections of the basin together with their representation in the numerical model.

The basin experiences a semi-arid climate, with an average annual precipitation of approximately 250 mm over the last 20 years. The main inflows to the aquifer are seasonal watercourses, being the most relevant one the Guadalentín River, which flows through the northeastern corner of the basin, at the north of the city of Lorca (Figure 3.1A). The Guadalentín River is the largest tributary of the Segura River. Other seasonal watercourses, including Nogalte, Torrecilla, and Béjar Ramblas, located at the NW and SE of the basin, become active only after periods of intense rainfall. In the

northeastern sector, the Alto Guadalentín aquifer connects laterally to the multi-layer aquifer system of the Bajo Guadalentín Basin [CHS, 2005]. Historically, groundwater flowed from the Alto Guadalentín Basin to the Bajo Guadalentín Basin. However, long-term groundwater depletion in the Alto Guadalentín Basin reversed the flow direction.

In the Guadalentín Basin groundwater extraction for agricultural purposes began in the early 1960s and rapidly increased during the mid-1970s and early 1980s, reaching its peak in the late 1980s, as shown in Figure 3.3. The largest extraction rate amounted to 8×10^7 m^3 in 1987. The excessive pumping caused a great lowering of the water table, which further raised the extraction cost. Following the long-term extraction, the water table declined not only in the sandy layer but drained the upper clay unit too, causing large land subsidence that remained unnoticed for decades. The discovery of significant subsidence rates occurred quite recently by González and Fernández [2011] who used InSAR analysis to process ERS and ENVISAT images acquired between 1992 and 2007. Indeed, this contribution and more recent papers [Bonì et al., 2015, Béjar-Pizarro et al., 2016, Ezquerro et al., 2020] highlight how this region was experiencing one of the highest subsidence rates in Europe. Cumulative land subsidence amounted to more than 3 m and, surprisingly, it did not cause any evident effects on the natural and anthropogenic environments.

The lowering of the water level, as pointed out by the piezometric network established in the area, led the government to impose strict regulations since 1989 in order to reduce groundwater pumping. Countermeasures included importing water from Tajo's basin, Central Spain, and shutting down a certain number of wells. As a result, the amount of extraction was cut more than half from 1988 to 2000 (Figure 3.3). Afterward, the extraction recovered a bit but stabilized around $4{\times}10^7$ m^3/yr around the 2010s. These new wells were drilled after 1988 in northeastern part of the basin to offset the wells abandoned in the southwest. Despite these efforts, the overall pressure head has decreased by over 150 m as of 2012.

3.2 Modelling Approach

Over the last decades, the phreatic aquifer system in the Alto Guadalentín basin has experienced a significant lowering of the water table, up to 150 m, that was accompanied by land subsidence of more than 3 m. From a me-

chanical point of view, land subsidence is due to the increase of the effective stress acting on the soil skeleton. However, according to Eq. 2.12, the effective stress variation in variably-saturated aquifer depends not only on the pore pressure change but also on the variation of the saturation degree. As this latter is always smaller than 1, it can be generally states that the contribution of unsaturated zone to land subsidence is smaller than that exerted by the pressure change within the saturated porous medium. As the water table declines, the unsaturated zone propagates downwards with S_w variations that progressively reduces in the shallower soils because of the shape of the capillary curve linking the pore pressure head to S_w. On the other side, the deformation caused by the change of the effective stress yields a porosity variation (Eq. 2.9), and consequently a variation of S_w also in the case of a constant water content.

This complex dynamics is properly accounted for in the analysis of land subsidence and the characterization of the soil parameters in the Alto Guadalentín basin. Due to the features of the aquifer system, the coupling between hydrologic and geomechanical parameters and processes cannot be neglected. Necessarily, this complexity and non-linearities make the model solution challenging and CPU demanding, requiring the development of a specific modelling approach.

It must be highlighted that the natural (e.g., rainfall recharge) and anthropogenic (i.e., groundwater pumping rates) factors driving the piezometric head evolution in this basin are highly uncertain. Although the main uncertainties are described in the following, here it is worth pointing out that this gap has suggested the use of homogeneous parameter distributions within each main geologic unit. With this assumption, the objective of the modelling effort is to ascertain the extent to which the hydrologic and mechanical behavior of the system can be captured at the "basin scale," acknowledging beforehand that local-scale "anomalous" trends recorded by individual piezometers or radar scatterers are unlikely to be satisfactorily replicated.

3.2.1 Calibration Scheme

In the present study, the focus is directed toward the two critical parameters of the aquifer system, which are the hydraulic conductivity of the sandy layer (K_s) and the oedometric compressibility of the clayey layer (c_{mc}). The

Table 3.1: InSAR stacks used to characterize land subsidence in the Alto Guadalentín Basin. The datasets are used to calibrate and validate the model.

satellite	period	modelling purpose	reference
ERS-ENVISAT	1992 - 2007		
ALOS-PALSAR	2007 - 2010	calibration	Bonì et al. [2015]
COSMO-SkyMed	2011 - 2012		
COSMO-SkyMed	2012 - 2016	validation	Ezquerro et al. [2020]

sandy layer is characterized by a hydraulic conductivity markedly larger than that of the other units filling the basin. Therefore, K_s is expected to exert a substantial impact on the distribution of pore pressure and the evolution of the water table throughout the entire aquifer system. Similarly, c_{mc} is selected for its significant role in the amount of land subsidence that affected the area. Because of the complexity of the coupled model, it has been assumed that each hydrogeologic unit is uniform, i.e. characterized by a single value of hydraulic conductivity and oedometric compressibility (i.e., elastic storage).

The measurements employed to characterize the properties of the aquifer system are categorized into two groups: piezometric records and land surface displacement observations. Regarding piezometric records, nine monitoring wells (Figure 3.4A) recorded data spanning from the 1970s to the 1980s. More recent water level data were collected from other six piezometers (Figure 3.4B). Land displacements in the study area were measured by processing four InSAR datasets spanning the period from 1992 to 2017 (Table 3.1). Figure 3.5 shows the average vertical rate ($v_z = \Delta u_z/\Delta t$) over each time interval. It is to be noted that ERS, ENVISAT, ALOS-PALSAR, and COSMO-SkyMed until 2012 are utilized for parameter inversion, while COSMO-SkyMed between 2012 and 2016 is reserved for model validation.

The calibration procedure begins by inferring K_s solely, rather than estimating both K_s and c_{mc} parameters. This choice arises from convergence challenges encountered in certain regions of the prior parameter space using the coupled model. Specifically, combinations of relatively low K_s and high c_{mc} lead to nonphysically large drawdown in the clayey layer. The result-

ing compaction, in turn, contributed to a drastic porosity collapse, thereby causing convergence failure during the coupled simulation.

Subsequent experiments revealed that the coupled model is more sensitive to variations in K_s. Moreover, piezometric records, which can more effectively constrain K_s than c_{mc}, have been available since 1972, i.e. 20 years in advance than InSAR measurements.

Consequently, K_s was calibrated first using the groundwater model only and the available piezometric data. Maintaining fixed porosity over time, the GW model converges more easily. Once the variability of the prior K_s distribution is bounded, the coupled model converges smoothly.

The calibration process for both parameters unfolds as follows:

1. Set up the GW model to investigate variations in hydraulic change (ΔH) given different K_s. The simulated time ranges from 1962 to 1988, a period encompassing early and intensified extraction phases (indicated by a green shadow in Figure 3.3);

2. Use of sparse grid collocation method to construct surrogate models capable of capture ΔH at the 9 available monitoring wells (Figure 3.4A);

3. Derivation of piezometric records noise via MAP estimation (Eq 2.92) and formulation of the posterior probability function of K_s, denoted as $\pi^1_{post}(K_s)$;

4. Approximation of $\pi^1_{post}(K_s)$ through 10,000 samples generated through MCMC simulations and calculation of statistical moments of K_s, including mean and variance;

5. Set up the coupled model designed to simulate both ΔH and the average vertical rate ($v_z = \Delta u_z/\Delta t$), considering various pairings of K_s and c_{mc} over an extended timeframe from 1962 to 2012;

6. Construction of surrogate models for approximating both ΔH at the 9 monitoring wells and v_z at the 39 locations shown in Figure 3.6) properly selected to represent the measured subsidence bowl. Notably, the prior distribution has been updated by
$\pi^1_{post}(K_s)$;

7. Estimation of noises for piezometric records and InSAR measurements through a Grid Search methodology followed by derivation of a joint

posterior probability function encompassing both parameters, i.e., $\pi^2_{post}(K_s, c_{mc})$;

8. Approximation of π^2_{post} utilizing 10,000 Markovian samples with subsequent computation of statistical moments for each parameter respectively;

9. Implementation of the coupled simulation incorporating expectations derived from the last step over a time frame extended to 2016. This step serves as validation against the InSAR dataset provided by COSMO-SkyMed from 2012 to 2016 (Table 3.1).

It is essential to point out the notable intrinsic uncertainties arising from groundwater withdrawals, natural recharge and piezometric observations, excluding aquifer properties. Concerning pumping values, rough estimations of the total annual pumping amount and the distribution of pumping wells are available, as illustrated in Figures 3.3 and 3.4. However, detailed information regarding the withdrawal rates and screen depths for each production well is unavailable, similar to the uncertainties surrounding discharging conditions. Regarding observations, piezometric records are expected to be more uncertain compared to InSAR datasets. Many monitoring wells lack full-time spans, especially during the 1980s when extraction was most intense. Additionally, the depth of monitoring wells are missing, and the precision associated with these wells, established in different periods, are also unavailable.

Considering the available information, attempting to quantify heterogeneous distributions of aquifer properties with all these uncertainties proves meaningless and impractical. Therefore, the inference of aquifer properties is simplified to two homogeneous variables, i.e. K_s and c_{mv}. This is the reason why the primary objective is not to achieve a perfect fit with all point-wise observations but rather to examine how well the predictive model aligns with data at a basin scale after inferring these two variables.

3.2.2 The Groundwater Flow Model

The primary objective of employing the groundwater (GW) model (alone) is to ascertain a relatively secure range for hydraulic conductivity (K_s) that would mitigate potential convergence issues within the coupled model.

Surrogate models are developed with the purpose of emulating solutions to GW flow, specifically changes in the hydraulic head (ΔH), utilizing sparse grid collocation methods. Hydraulic head change, rather than absolute head, is selected as the quantity of interest (QoI) due to its reduced sensitivity to initial head conditions. These surrogates serve as an efficient means to reduce the computational burden within the Bayesian framework to infer K_s.

By incorporating piezometric records, Bayesian inference enables us to derive posterior distributions for K_s, thereby allowing us to identify a range of K_s values that are consistent with observed hydraulic behavior while maintaining numerical stability in coupled simulations.

The Groundwater model setup

The geological structure of the aquifer system is conceptualized by four lithological units, i.e., clay, sand, silt, and rock. The geometry of each unit is reconstructed using the thickness contour maps available from Cerón-García [1995]. The bottom of the three-dimensional (3D) domain is fixed at -350 m above the mean sea level, where the bedrock acts as the basement for the model (Figure 3.2). This depth ensures that the prescribed boundary conditions do not affect the model solution within the upper layers.

The 3D tetrahedral mesh is developed starting from a two-dimensional (2D) triangulation of the geologic surfaces. The top of each unit is represented by applying an array of z-coordinates on the surface. An initial coarse 3D outline of geological structure is formed by stacking and connecting these 2D surfaces according to their coordinates. Lastly, this 3D structure is finely discretized into 163,333 nodes and 909,301 tetrahedra. The TetGen code [Si, 2008] was used to generate the boundary constrained conforming (Delaunay) discretization. The characteristic element size varies across the lithological units. The clay layer is discretized by the smallest elements, whose characteristic size amounts to a few meters to accurately reproduce the evolution of the water content a pore pressure. The element size of bedrock exceeds 1,000 m, while the size of sand and silty layers falls within the range of clay and bedrock layers.

As regards the boundary conditions, the lateral and bottom surfaces, which predominantly consist of bedrock, are generalized as no-flow boundaries. The northern boundary, hydraulically connected to the Bajo Guadalentín Basin, is prescribed as a Dirichlet boundary. The variation of the hy-

draulic head is estimated by linear regression analysis on piezometric records available from wells located near the boundary between the two basins. Note that precipitation and irrigation recharge are not considered in the simulation due to their low significance. Indeed, the presence of a thick clay layer, combined with a depth to the water table exceeding tens of meters in the sandy area, substantially prevents precipitation and return irrigation water from infiltrating and recharging the aquifer.

Pumping wells (Figure 3.7A) and the Guadalentín River inflows (Figure 3.7B) are designated as Neumann boundaries in the GW model. The annual recharge rate is evenly distributed among the respective finite elements. To prevent water extraction from unsaturated areas, each pumping well is represented by a series of vertically aligned nodes within the sandy layer with an elevation lower than 230 m above msl. Due to the lack of specific information, the annual pumping rate provided in Figure 3.3 is equally divided between the various wells. The initial hydraulic head distribution is obtained from a pre-development map of the water table elevation after Ezquerro et al. [2017]. The values are first interpolated on the 3D mesh assuming a hydrostatic distribution. A few-year warming-up period without discharging conditions is initially run to initialize the groundwater flow model with an equilibrium condition. Finally, Table 3.2 lists the hydraulic properties of each unit from top to bottom, with values derived from previous studies carried out in the area [Ezquerro et al., 2017, Fernandez-Merodo et al., 2021]. Notice that K_s is the only non-deterministic parameter. Moreover, the silt layer is subdivided into an upper 50 m layer, characterized by higher permeability where extraction can occur, and a lower layer that is nearly impervious. Concerning the parameters of the capillary curves (Eqs. 2.7 and 2.8), the following parameters have been used [Fernandez-Merodo et al., 2021]: $\alpha = -0.54$ m^{-1}, $n = 1.25$, and $S_{wr} = 0.13$. Due to the lack of more specific data, these values are associated with both the sand and clay units.

Sparse-grids-based surrogate model

In this section, we aim to approximate the relationship between hydraulic conductivity (K_s) and drawdown (ΔH) at a set of space-time points $\{(\boldsymbol{y}_i, t_i)\}_{i=1}^{M}$, corresponding to the nine monitoring wells shown in Figure 3.4A and at time points between 1972 to 1988, thus $M = 9 \times 16$.

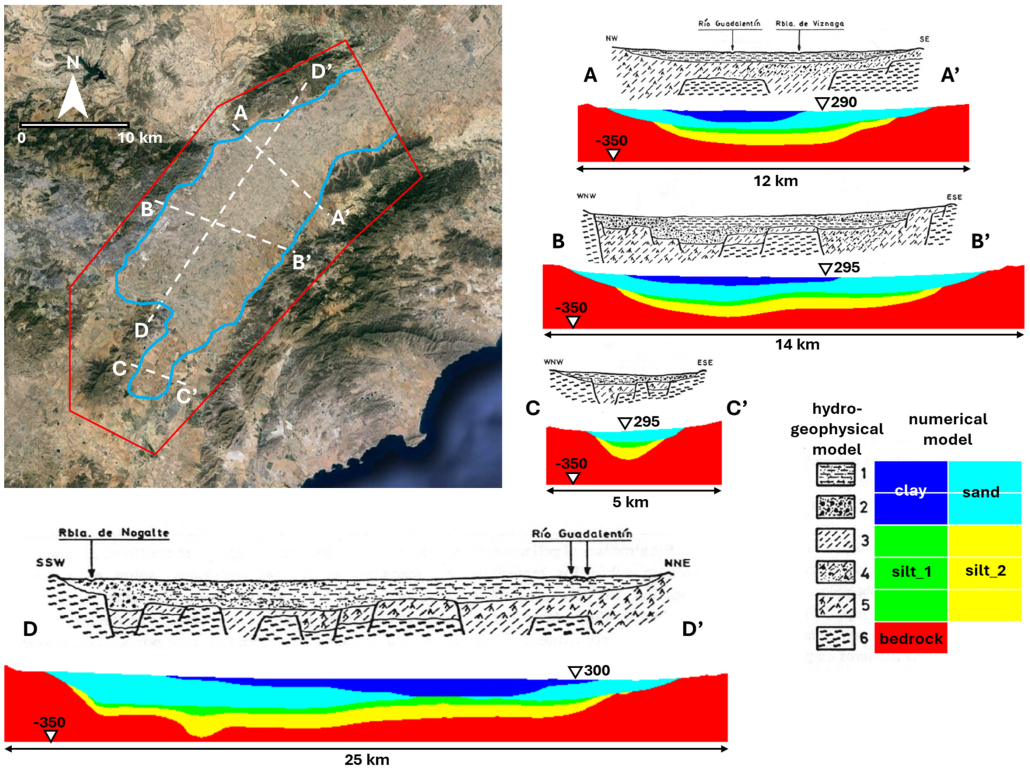

Figure 3.2: Comparison between the NW-SE geologic profiles as published in Cerón-García [1995] and reconstructed in the numerical model. The soil classification is the following. 1: clay, limestone, sand and gravel; 2: sand, gravel and conglomerate; 3: marl; 4: marl with sand and conglomerate; 5: marl with gypsum; 6: metamorphic substratum. The elevation values inserted in the sections are in m above mean sea level (msl). The correspondence between the legend by Cerón-García [1995] and the one used in the numerical model is provided.

Table 3.2: Hydro-geomechanical properties of the lithological units used in the GW model

unit	hydraulic conductivity K (m/d)	compressibility c_m (kPa^{-1})
clay	$5 \cdot 10^{-3}$	$2 \cdot 10^{-5}$
sand	$U[0.03, 3]$	$5 \cdot 10^{-6}$
silt_1	$1 \cdot 10^{-3}$	$2.5 \cdot 10^{-6}$
silt_2	$1 \cdot 10^{-8}$	$1.8 \cdot 10^{-7}$
bedrock	$1 \cdot 10^{-9}$	$1.8 \cdot 10^{-7}$

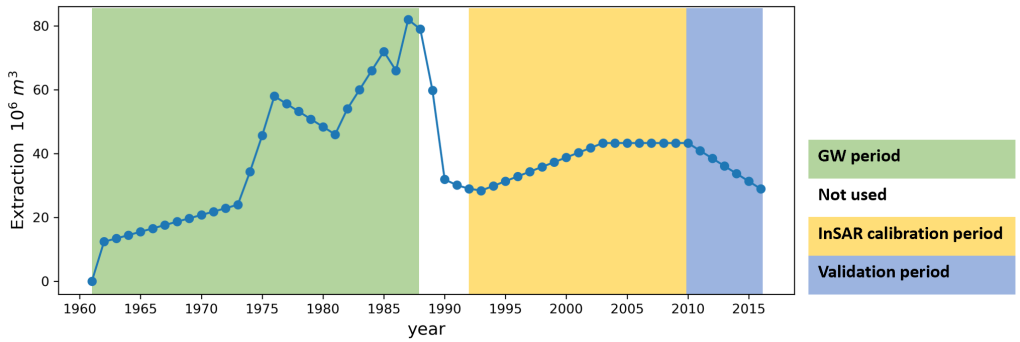

Figure 3.3: Yearly groundwater withdrawal from the Alto Guadalentín aquifer system over the time interval from 1962 to 2016 spanned by the study. The color shadows indicate the periods used for the groundwater flow calibration (green), coupled model calibration (yellow), and model validation (blue).

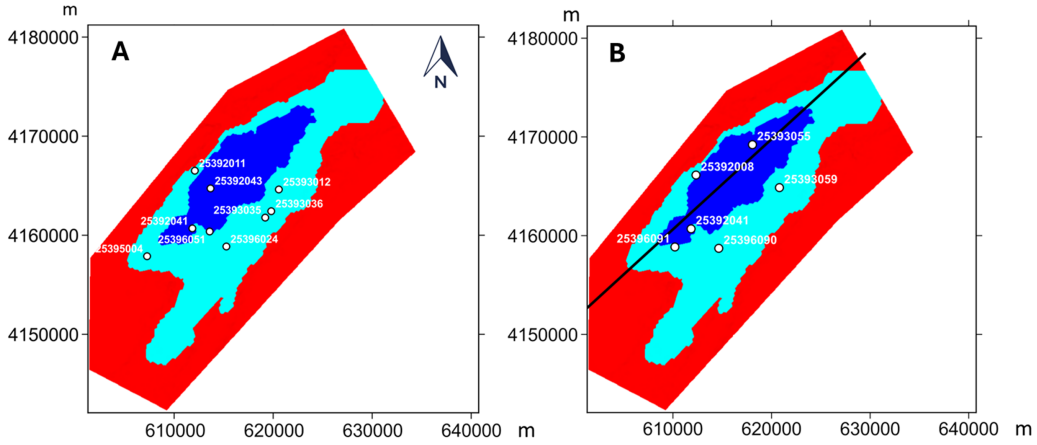

Figure 3.4: A) Location of the 9 monitoring wells where piezometric records are available from 1972 to 1988 and are used for model calibration. B) Location of the six monitoring wells where piezometric records are available between 1988 and 2012. These data are used for model validation. The black line in B marks the profile selected to present the calibrated model outcome in terms of S_w.

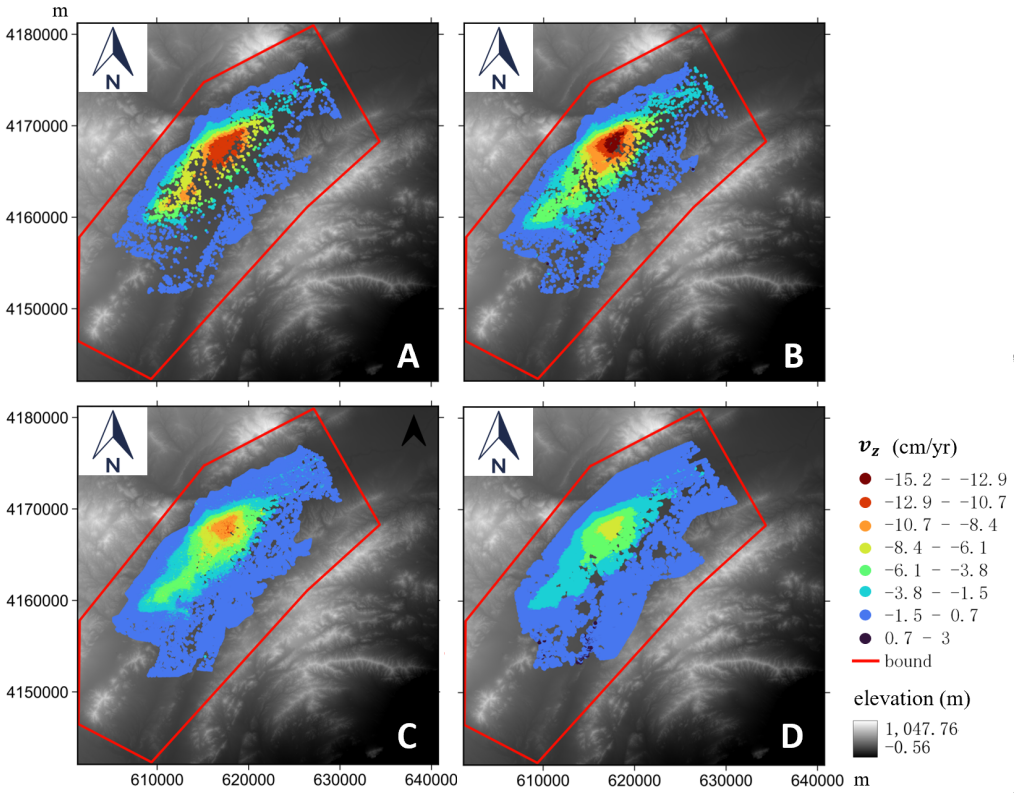

Figure 3.5: Average vertical displacement rates $v_z = \Delta u_z/\Delta t$ measured by InSAR over the period A) 1992-2007, B) 2007-2010, C) 2011-2012, and D) 2012-2016. Redrawn after Bonì et al. [2015] and Ezquerro et al. [2020].

We assume that K_s follows a uniform prior distribution, i.e., $K_s \sim U(0.03, 3)$ m/d (Table 3.2), with thresholds determined through the previous study Ezquerro et al. [2017]. Moreover, the prior is transformed into a log-uniform form, i.e., $\log(K_s/3) \sim U(-2, 0)$, facilitating comprehensive exploration over the parameter space that spans two orders of magnitude, especially in the lower range. Specifically, according to the notation introduced in Sections 2.2.1and 2.2.3, we set $N = 1$ and $x = \log(K_s/3)$. Then, we consider the models $\mathcal{M}_i(x) = \mathcal{M}(\boldsymbol{y}_i, t_i, x)$, $i = 1, \ldots, M$ (cf. Eq. 2.20) and corresponding surrogate models $\widehat{\mathcal{M}}_i(x) \approx \mathcal{M}_i(x)$ (cf. Eq. 2.21).

Suitable collocation knots for uniform random variables are symmetric Leja knots (see Piazzola and Tamellini [2023a] and Section 2.2.1) with the appropriate level-to-knots function provided in Eq. 2.22. Their nested structure ensures the reuse of existing knots in higher refinement levels, as shown

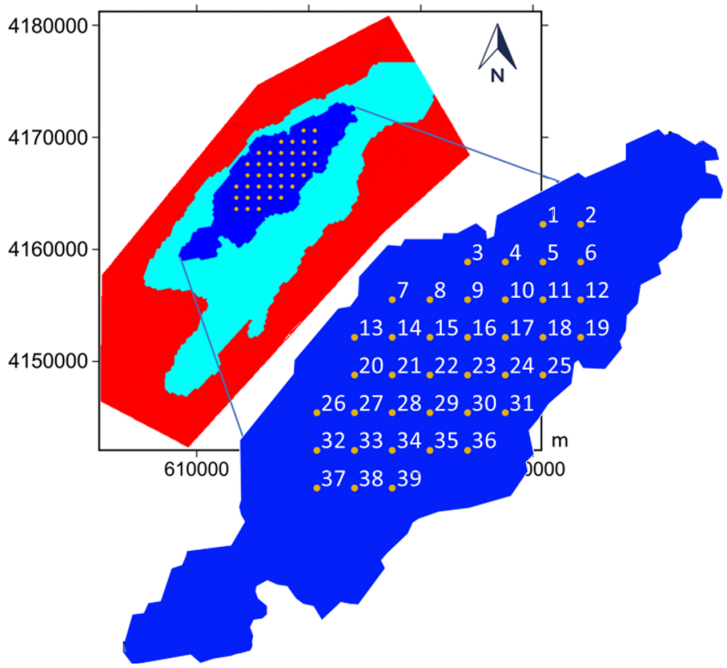

Figure 3.6: Locations of the 39 sites (corresponding to surface nodes of the FE mesh) used to calibrate the coupled model.

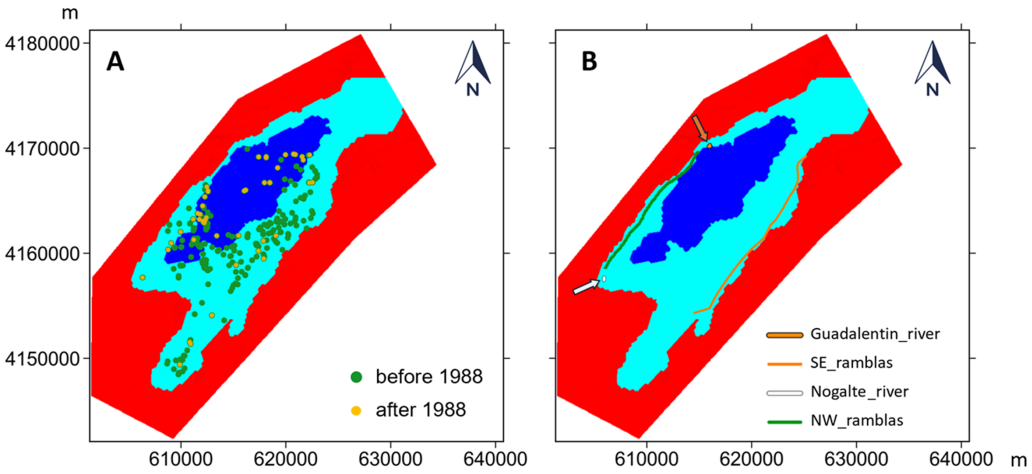

Figure 3.7: Distributions of hydraulic boundary conditions. A) location of the pumping wells over two periods. B) Lateral recharges represented by the Guadalentín and Nogalte rivers and distributed ramblas.

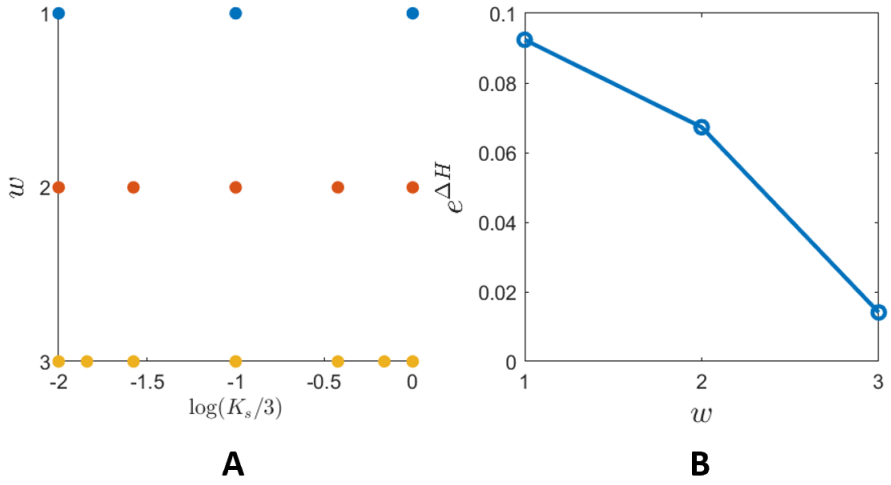

Figure 3.8: A) Collocation knots on $x = \log(K_s/3)$ at refinement levels $w = 1, 2, 3$. B) Mean relative error e with an increasing refinement level w.

in Figure 3.8A, where the knots corresponding to increasing refinement levels $w = 1, 2, 3$ as shown in Eq. 2.34.

The corresponding surrogates are obtained according to Eq. 2.32, using the full model (GW) solutions for the prescribed collocated knots. Note that, since the knots are computed for $x = \log(K_s/3)$, the corresponding values of K_s must be derived and input in the simulations. The quality of the three surrogates is assessed by evaluating the mean relative error e as follows:

$$e = \frac{1}{L}\sum_{l=1}^{L}\sum_{i=1}^{M}\left|\frac{\mathcal{M}_i(x^l) - \widehat{\mathcal{M}}_i(x^l)}{\mathcal{M}_i(x^l)}\right| \tag{3.1}$$

The value of e is evaluated by randomly selecting $L = 6$ validation designs x^l, $l = 1, \ldots, L$ from the prior uniform interval $[-2, 0]$. The refinement level w was increased until e fell below the threshold value of 0.05. Figure 3.8B shows the decrease in relative error with increasing w, reaching the criterion for $w = 3$. The corresponding surrogates require seven collocation knots, see Figure 3.8A.

With the aid of surrogates, the responses of each monitoring well over different K_s were readily generated, as shown in Figure 3.9. Note that, the secondary horizontal axis is obtained by stacking different yearly surrogate outcomes, which aims to elucidate the temporal responses of the aquifer sys-

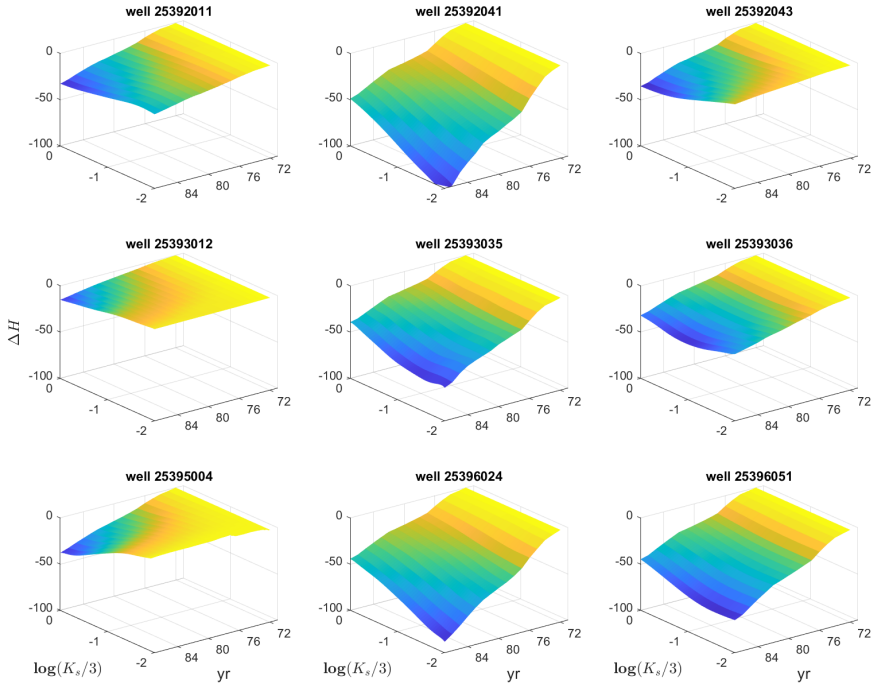

Figure 3.9: Surrogate model outcomes ΔH (m) at nine monitoring wells (Figure 3.4A) with the refinement level $w = 3$. Notably, the approximation is inherently a one-dimensional problem, as denoted by $\widehat{\mathcal{M}}_i(\log(K_s/3))$. The secondary horizontal axis represents temporal progression, constituted by an ensemble of surrogates for different years.

tem. The monitoring wells could be divided into two groups based on their pressure head behaviors. The first group, including *well 25392041*, exhibited a positive correlation between drawdown and time, indicating their proximity to the extraction wells. They quickly responded to groundwater pumping with noticeable drawdown. In contrast, the second group, exemplified by *well 25392011*, demonstrated the opposite behavior, with drawdown surfaces decreasing as hydraulic conductivity and time increased. These wells were farther from the extraction wells, and they experienced significant drawdown only when the aquifer was more permeable. As K_s decreased, these monitoring wells became less affected by groundwater extraction, resulting in smaller drawdown.

Bayesian calibration for hydraulic conductivity with piezometric records

Unfortunately, the temporal continuity of the piezometric dataset is compromised due to missing records in various years for each monitoring well, thus the aggregate size of drawdown measurements is reduced to 82, i.e., $\mathcal{O} = \{m_1, \ldots, m_M\}$ with $M = 82$. As described in Section 2.2.3, to perform the Bayesian calibration we need first to estimate the noise variance of the piezometric data. Since we assume a uniformly distributed prior for $\log(K_s/3)$, the MAP estimation simply requires minimizing the sum of squared errors between model solutions and observations:

$$x^* = \underset{x\in[-2,0]}{\arg\min} \sum_{i=1}^{M} \big(m_i - \widehat{\mathcal{M}}_i(x)\big)^2.$$

Then, the variance of the piezometric noise $\sigma^2_{\varepsilon_{\Delta H}}$ can be approximated by Eq. 2.93.

The optimization problem is solved by the gradient descent algorithm with various initial guesses to avoid the local minimum, resulting in $x^* = -0.91$. Correspondingly, we obtained $\sigma_{\varepsilon_{\Delta H}} \approx 16.63$ m/yr. Subsequently, the slice sampling method (see Section 2.2.3) is employed to sample from the posterior pdf. We discarded the first 1,000 samples, known as *burn-in* to ensure convergence, and thereafter drew 10,000 samples using the GW surrogates. The resulting Markovian samples suggest that the parameter follows a Gaussian distribution, i.e., $\log(K_s/3) \in \mathcal{N}(-0.94, 0.24^2)$. Hence, K_s follows a log-normal distribution, as depicted in Figure 3.10B. The median of the log-normal pdf, which corresponds to the mean of $\log(K_s/3)$, is considered the most likely value of K_s given the available piezometric records.

3.2.3 The Coupled Model

The coupled model is utilized to represent the relationship between two input variables and two quantities of interest (QoIs): the variation in hydraulic head and average vertical displacement rate. The relationship can be represented as $[\Delta H, v_z] = \mathcal{M}(K_s, c_{mc})$. This computational model serves as the forward model within a Bayesian framework to deduce the probability function of the two input parameters. In practical applications, cost-effective surrogate models, $\widehat{\mathcal{M}}_{\Delta H}$ and $\widehat{\mathcal{M}}_{v_z}$, are developed using sparse grid collocation technique. These surrogates facilitate the generation of an extensive set

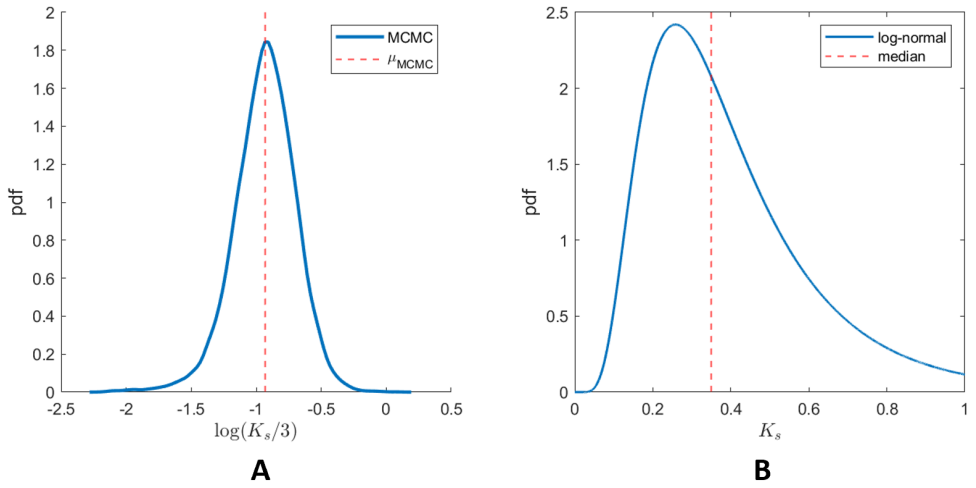

Figure 3.10: A) Posterior pdf π^1_{post} and mean of $\log(K_s/3)$ as derived from the Markovian samples. B) Corresponding log-normal distribution of K_s

of Markovian samples that characterize the statistical properties of the input parameters.

The subsequent sections delineate the set-up of the coupled model and describe the implementation of sparse grid collocation. Thereafter, a Bayesian inferential process is employed to ascertain the posterior distribution of these parameters.

The coupled model setup

The configuration of GW model is nearly retained in the coupled model. The FE grid, unit zonation, and hydraulic conditions are the same as in the previous analysis. The coupled simulations extend to 2012 during the calibration phase, and the model validation ends in 2016. Within the extended periods, the distribution of hydraulic boundaries is identical to that of the GW model, with the exception of the pumping wells as indicated in Figure 3.7A. The temporal variations of boundary conditions are updated in the same manner as introduced in the GW model.

As for the mechanical part, horizontal displacements are precluded along the lateral boundaries with a traction-free top plane and zero displacements on the bottom. The density of the soil bulk is 2,000 kg/m^3. We assume the minimum (maximum absolute value) σ_1 and maximum σ_3 (minimum ab-

Table 3.3: Hydro-geomechanical properties of clayey and sandy units used in the coupled model.

unit	hydraulic conductivity K m/d	compressibility c_m kPa^{-1}
clay	$5 \cdot 10^{-3}$	$U(4 \cdot 10^{-6}, 4 \cdot 10^{-5})$
sand	log-normal$(-0.94, 0.24^2)$	$5 \cdot 10^{-6}$

solute value) principal stresses coincide with the vertical $\hat{\sigma}_v$ and horizontal $\hat{\sigma}_h$ stress, respectively. The initial σ_v increases with a depth in proportion to the specific weight of the overlying sediments. The initial $\hat{\sigma}_v$ obtained by Eq. 2.12 is set to be the preconsolidation stress, namely the maximum historical vertical effective stress $\hat{\sigma}_{z,\max}$. Besides, the ratio between $\hat{\sigma}_h$ and $\hat{\sigma}_v$ is fixed equal to $\nu/(1-\nu)$ with Poisson's ratio $\nu = 0.25$. In this work, clay and sand layers are both prescribed as bi-elastic materials whose c_m varies depending on $\hat{\sigma}_{z,\max}$ as presented in Eq. 2.16. The other units behave elastically whose compressibility c_m is provided in Table 3.2. Table 3.3 summarizes the hydraulic and oedometric compressibility values adopted in the coupled model.

Sparse-grids-based surrogate model

The use of surrogate models becomes a necessity as the CPU cost of coupled models is very large, with a single run needing more than 3 days on a computer equipped with Intel Core i7-10700 2.90GHz. The focus is placed on two input parameters, namely the hydraulic conductivity of the sand unit K_s and the compressibility of the clay unit c_{mc}, alongside two quantities of interest (QoIs): the drawdown ΔH and the average subsidence rate v_z. The surrogate models are designated as $\widehat{\mathcal{M}}_i^{\Delta H}(\boldsymbol{x})$ and $\widehat{\mathcal{M}}_j^{v_z}(\boldsymbol{x})$, for which $i = 1, \ldots, M_{\Delta H}$ and $j = 1, \ldots, M_{v_z}$ denote indices within their respective sets.

The measurement set $\mathcal{O}_{\Delta H}$ corresponds to an array of space-time points similar to that discussed in preceding sections. In contrast, InSAR datasets offer a more comprehensive array of measurements represented by the movement of the Permanent Scatterers (PS). However, it is technically impracticable to represent all the PS using mesh nodes due to the PS excessive density. Given that the primary focus is on the parameter c_{mc}, we select 39 uniformly distributed observation points within the trace of the clay layer, i.e. within the area experiencing a significant land subsidence, as illustrated

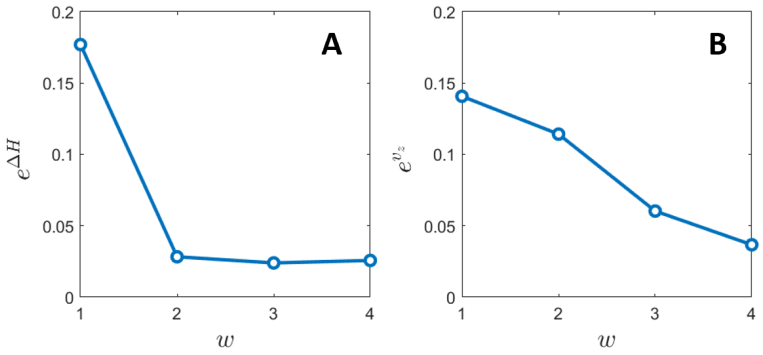

Figure 3.11: Mean relative errors A) $e^{\Delta H}$ and B) e^{v_z} with an increasing refinement level $w = 1, 2, 3, 4$.

in Figure 3.6.

The logarithm of K_s, specifically $\log(K_s/3)$, is assumed to follow the Gaussian prior distribution derived from the prior calibration of K_s only (GW model). The parameter c_{mc} is supposed to follow the uniform distribution $c_{mc} \sim U(4 \cdot 10^{-6}, 4 \cdot 10^{-5})$ kPa^{-1}. For an easier notation, let us define $c'_{mc} = 10^5 c_{mc}$. Thus, the parameter vector $\boldsymbol{x}$ is represented as $[\log(K_s/3), c'_{mc}]$, constrained within the domain $\Xi = \mathcal{N}(-0.94, 0.24^2) \times U(0.4, 4)$.

In the following analysis, the *2-step* level-to-knots function with symmetric Leja points is utilized again to establish collocation points. Figure 3.11 shows that the surrogate models yield accurate approximations when the refinement level w is augmented to 4. The accuracy is quantified by calculating the mean average error, as defined in Eq 3.1, for four validation designs ($L = 4$). These errors are denoted as $e^{\Delta H}$ and e^{v_z} for drawdown and average subsidence rate, respectively. The errors are below the threshold value of 0.05 at an refinement level of 4.

The construction of a two-dimensional sparse grid warrants attention. Figure 3.12 displays the multi-index $\mathbf{i}$ corresponding to $w = 4$, derived from Eq 2.34. It is important to mention that Leja points, weighted by the Gaussian measure (referenced in Piazzola and Tamellini [2023a]), have been employed for sampling the hydraulic conductivity parameter K_s. Given that K_s was estimated during previous calibration, it is considered more imperative to calibrate compressibility c'_{mc}. Therefore, a greater number of knots are allocated along this dimension. This approach implies an anisotropic sampling strategy within the parameter space. Figure 3.13A shows the sparse

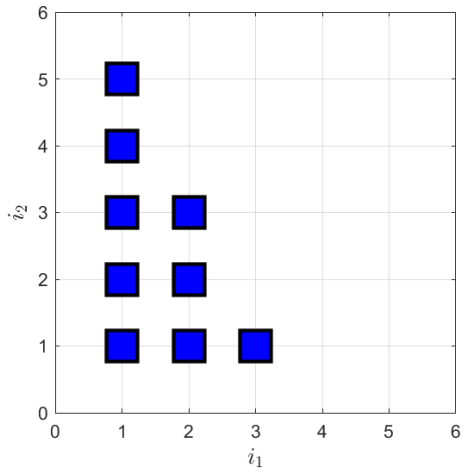

Figure 3.12: Multi-index **i** of the final tensor grid. More knots were drawn from c_{mc}, which corresponds to i_2, using an anisotropic sampling strategy.

grid employed for the approximation based on 21 collocation knots with the refinement level $w = 4$. Figures 3.13(B-G) depict the set of tensor grids that contribute to the final sparse grid. Notice that specific tensor grids of lower order involved in Figure 3.12, such as $\mathcal{T}_{[1,1]}$, are included within tensor grids of higher order and are consequently omitted from representation in Figure 3.13.

Bayesian calibration for parameters with measurements

The InSAR observations are utilized by selecting the values from the closest PS to the node of the finite element mesh at 39 locations as depicted in Figure 3.6, over three time periods. If the distance between the node under investigation and the nearest PS exceeded 100 m, it was assumed that no measurement is available at that space-time node. As a result, the aggregate number of InSAR measurements amounted to 78 ($M_{vz} = 78$). In addition to the InSAR data, the same set of piezometric records ($M_{\Delta H} = 82$) used in the GW analysis are utilized to infer two input parameters.

In this setting, the $-\ln(\pi_{post})$ has to take into account the two sets of measurements, see Eq. (2.94). Specifically, we can introduce a hyper-parameter $\lambda \in \mathbb{R}$ that takes into account the ratio between the variances,

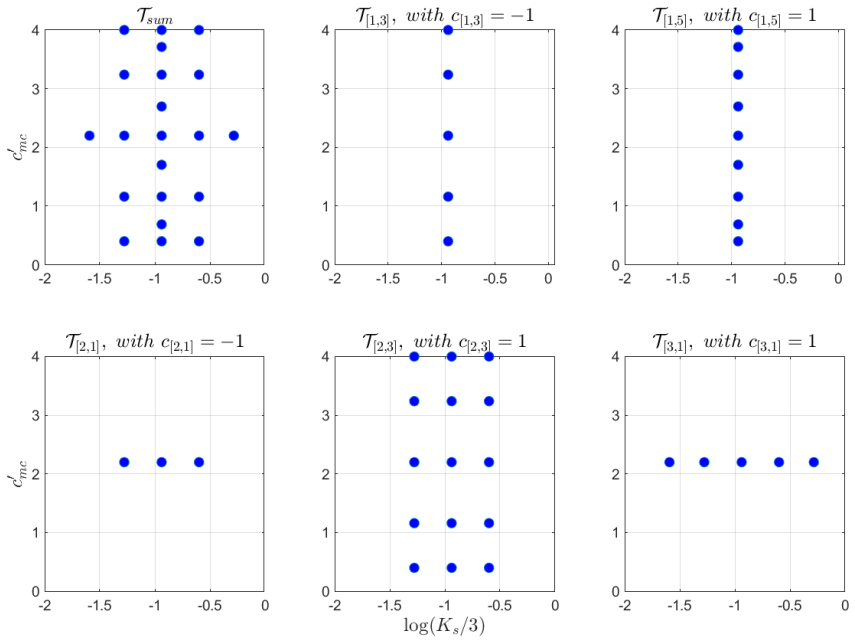

Figure 3.13: A) Final sparse grid. B-G) Decomposition of the final sparse grid into tensor grids. Some repeated knots were discarded in the final sparse grid.

i.e. $\lambda := \sigma^2_{\varepsilon_{\Delta H}}/\sigma^2_{\varepsilon_{v_z}}$ and write the$-\ln(\pi_{post})$ as follows:

$$
\begin{aligned}
-\ln(\pi_{post}) &= \mathrm{NLL}(\boldsymbol{x}, \mathcal{O}^{\Delta H} \cup \mathcal{O}^{v_z}) - \ln(\pi_{prior}) \\
&= \sum_{i=1}^{M_{\Delta H}} \left(m_i^{\Delta H} - \mathcal{M}_i^{\Delta H}(\boldsymbol{x})\right)^2 + \lambda \sum_{j=1}^{M_{v_z}} \left(m_i^{v_z} - \mathcal{M}_i^{v_z}(\boldsymbol{x})\right)^2 \\
&+ \frac{1}{2} M_{\Delta_H} \ln(2\pi\sigma^2_{\varepsilon_{\Delta_H}}) + \frac{1}{2} M_{v_z} \ln(2\pi\sigma^2_{\varepsilon_{v_z}}) + \frac{\sigma^2_{\varepsilon_{\Delta H}}}{0.24^2}(x_1 + 0.94)^2
\end{aligned}
\tag{3.2}
$$

where $x_1 = \log(K_s/3)$. The constant terms that come from the prior pdf are dropped here. Due to the presence of the Gaussian prior pdf, λ cannot be directly solved as shown in Porta et al. [2014]. Alternatively, we employ a Grid Search method in which we propose several possible combinations for $[\sigma^2_{\varepsilon_{\Delta H}}, \lambda]$ based on prior information, including the last estimation of $\sigma^2_{\varepsilon_{\Delta H}}$ and InSAR precision. For each selected $[\sigma^2_{\varepsilon_{\Delta H}}, \lambda]$, we compute the corresponding MAP that minimizes Eq. 3.2. In this way, we estimated $\sigma^2_{\varepsilon_{\Delta H}} = 254$ m^2 and

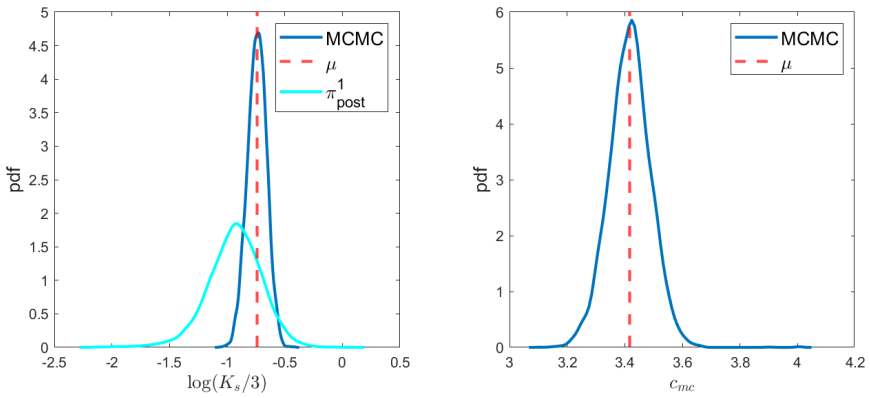

Figure 3.14: Marginal posterior pdfs and corresponding means for the two input parameters A) $\log(K_s/3)$ and B) c'_{mc} as obtained by inference with piezometric and InSAR measurements. The Gaussian pdf of $\log(K_s/3)$ obtained by inference with piezometric records only is denoted by the light blue line in panel A.

$\lambda = 57$.

Similarly to the GW analysis, 10,000 samples with 1,000 *burn-in* are drawn using the same slicing MCMC method (cf. Section 2.2.3). It reveals that both parameters follow Gaussian distributions, i.e., $\log(K_s/3) \in \mathcal{N}(-0.74, 0.08^2)$ and $c'_{mc} \in \mathcal{N}(3.42, 0.07^2)$. In comparison to the preceding calibration outcome, as depicted by the light blue line in Figure 3.14A, a substantial reduction in the variance of $\log(K_s/3)$ was observed. Additionally, there was a certain shift in the distribution toward higher values. These discrepancies underscore the enhanced characterization of hydraulic conductivity attributable to the incorporation of InSAR measurements. It is imperative to acknowledge that an understanding of the interaction between hydraulic dynamics and deformation is crucial for mitigating biases inherent within computational models.

In addition to solving the inverse problem, surrogates also allow us to evaluate the effects of input parameter uncertainties on the uncertainty of the model outputs at a reduced computational cost. Therefore, the Markovian samples are used to compute the corresponding drawdown and subsidence rate using the surrogates.

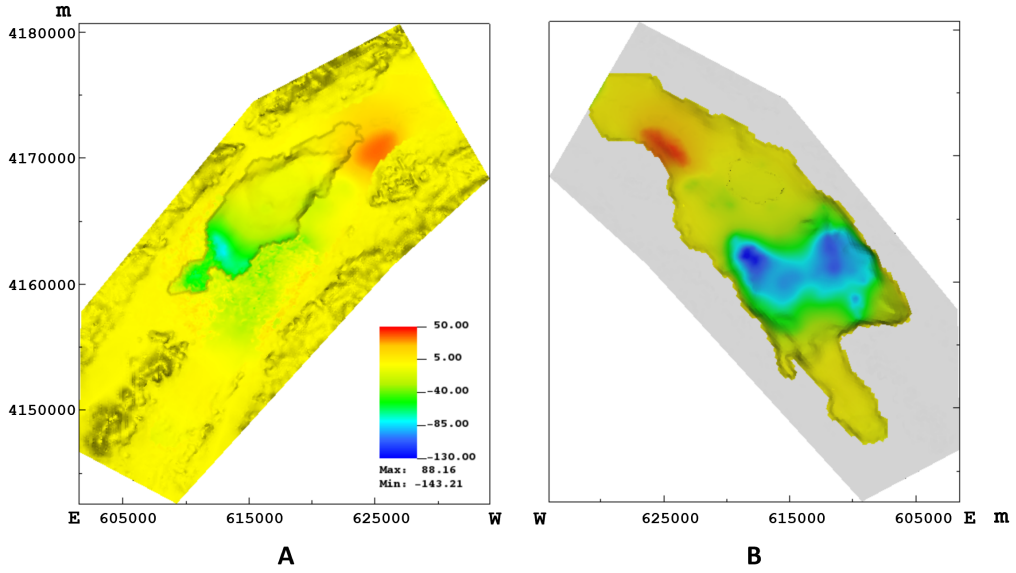

Figure 3.15: Hydraulic head variation (m) within the sandy layer from 1962 to 1988. A) ΔH on the top and B) on the bottom of the geologic unit. The gray area in B) denotes the bedrock.

3.3 Model Outcomes

The expectation of Markovian samples is frequently regarded as a robust estimator for the true parameter values. The outcomes derived from the coupled model with the latest inferred values, i.e., $K_s = 0.54$ m/d and $c_{mc} = 3.42 \cdot 10^{-5}$ kPa^{-1} are presented. The numerical outcomes are compared with the available measurements.

3.3.1 Hydrological Behavior

Figure 3.15 shows the hydraulic head change from 1962 to 1988 as obtained on the top and bottom of the sandy unit, which is the layer experiencing the largest drawdown. Notably, ΔH exhibited pronounced values in the south-western region, as the consequence of the larger concentration of pumping wells, and progressively propagated towards the northeastern basin. At the end of 1988, drawdown exceeded 100 m in southern regions while reaching approximately 30 m in northern sectors.

The variations of the hydraulic head within the clay layer were relatively smaller due to the lower permeability of this unit. Particularly, the upper

part of the clay was barely affected in 1988. A region to the north-east adjacent to zones of lateral recharge and near the northeastern basin contiguous with the Bajo Guadalentín Basin exhibits an increase in hydraulic head (denoted by warmer colors in Figure 3.15). The rise of the hydraulic head can be explained by the imposed boundary condition in terms of lateral recharge and by a pre-existing inflow from the northeastern boundary associated with an approximated initial condition. Unfortunately, no piezometric wells are located in that region to better condition and calibrate the aquifer system.

A comparative analysis between the model outputs and the piezometric measurements in terms of hydraulic change ΔH is displayed in Figure 3.16. The figure reveals a generally good agreement between the model and observations on *piezometers 25392041*, *25395004*, *25396024* and *25396051*. For the remaining piezometers, discrepancies primarily arise from inconsistencies between the imposed withdrawal conditions and piezometric records. Take piezometer *25392011* as an example, where only a few wells are located in the surroundings, as illustrated in Figures 3.7 and 3.4. Additionally, the cumulative extraction was evenly distributed between all the wells, leading to an underestimated pressure decline, similar to *wells 25392043* and *25393012*. Conversely, piezometers *25393035* and *25393036* were surrounded by more wells, but their hydraulic head records are characterized by a stable behavior.

Unfortunately, as highlighted above, data are limited for both pumping and monitoring wells, and additional information would be necessary to accurately reproduce their responses, in particular the specific pumping amount from each wells. Overall, the comprehensive spatio-temporal piezometric data during the critical period in the 1980s are scarce. Therefore, any inversion efforts based solely on these sparse datasets may be biased and incomplete.

Notice in Figure 3.16 that the model outcomes as obtained from the GW and coupled approaches differ negligibly. Despite characterized by a higher permeability, the coupled model predicted a gently larger hydraulic head decline than that computed by the GW model. This phenomenon can be attributed to the porosity decrease induced in the coupled model by land subsidence. The finding presented herein highlights the bidirectional relationship between hydraulic dynamics and aquifer deformation: not only the former exert an influence on the latter, but alterations in aquifer porosity due to soil deformation also affect the hydraulic dynamics.

The cumulative outcomes in terms of drawdown over the entire simulated

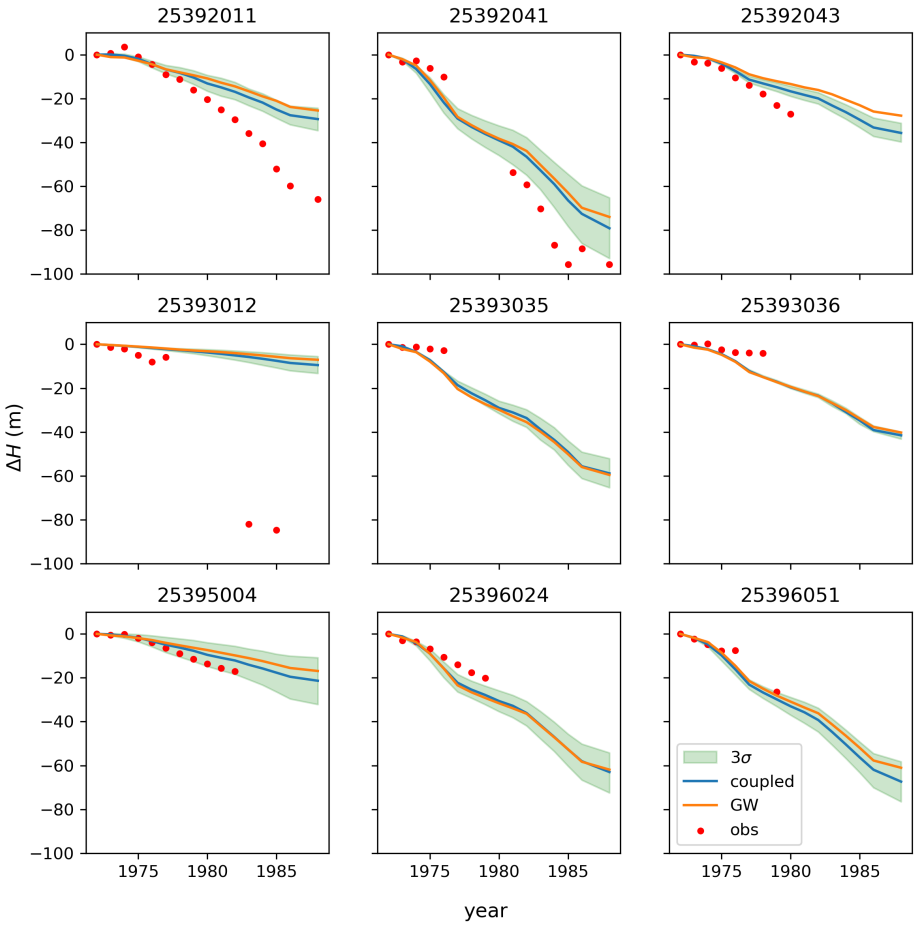

Figure 3.16: Comparison between the measured and simulated hydraulic head change ΔH from 1972 to 1988. Blue and orange lines represent the outcome obtained by the GW and coupled solutions, respectively, while red dots indicate the piezometric observations. The green-shaded areas provide the ΔH uncertainty $[\mu - 3\sigma, \mu + 3\sigma]$ as quantified using surrogate predictions on Markovian samples (Section3.2.3). Each subplot refers to one of the nine observation wells shown in Figure 3.4A).

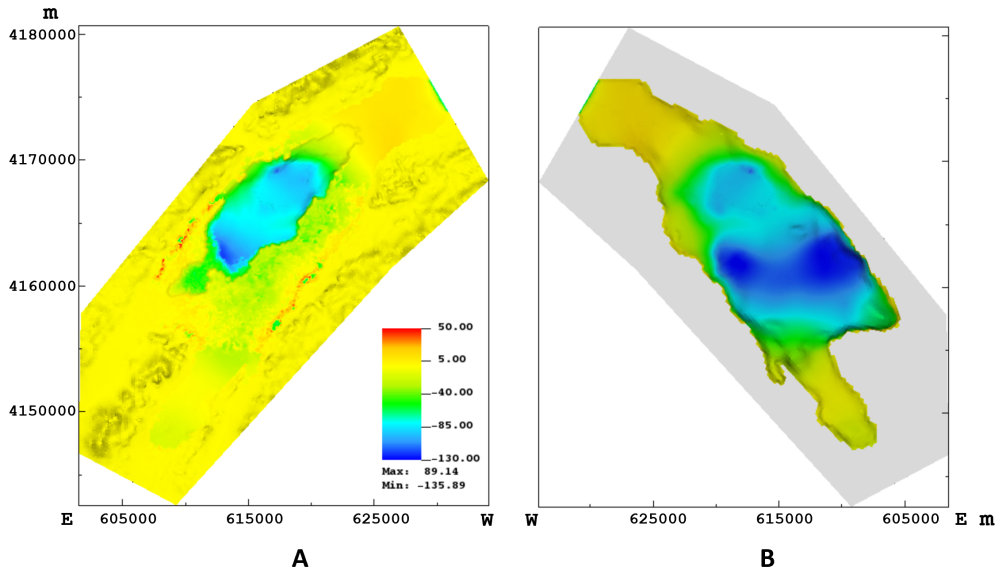

Figure 3.17: Hydraulic head variation (m) within the sandy layer from 1962 to 2016. A) ΔH on the top and B) on the bottom of the geologic unit. The gray area in B) denotes the bedrock.

period from 1962 to 2016 is presented in Figure 3.17. The model highlights the two drawdown centers that correlate with the well locations during the two extraction phases (Figure 3.7). The maximum decline of the hydraulic head amounted to more than 130 m.

Figure 3.18 displays the saturation distribution along a vertical section crossing the basin along a southwest-to-northeast direction. The results refer to the years 1962 (initial condition, 1988 (in correspondence with the maximum annual pumping rate), and 2016 (at the end of the simulated period). Notice how the saturation degree within the clay layer reduced significantly only during the last period.

Figure 3.19 presents a comparison in terms of hydraulic head change from 1988 to 2012 at the six monitoring wells available over the last simulation interval (Figure 3.4B). These data were used for model validation and were not incorporated into the calibration process. The model simulations indicate that all six wells experienced a certain decrease in hydraulic head before the 1990s, followed by a certain recovery during the early 1990s due to the significant decrease of the pumped volume during those years (Figure 3.3), and subsequently a further gentle decline until the end of the

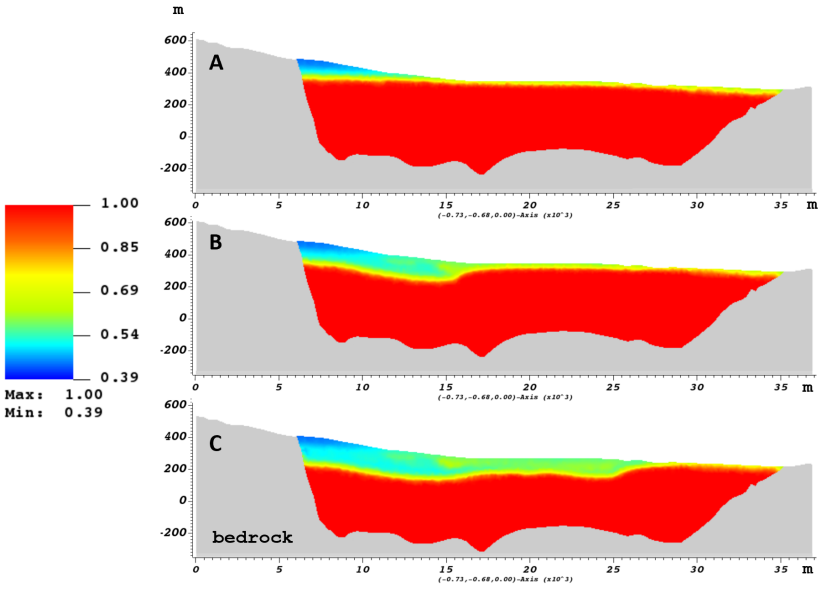

Figure 3.18: Saturation degree S_w along the profile indicated in Figure 3.4B) in A) 1962, B) 1988, and C) 2016. The grey areas denote the bedrock.

simulation period. As outlined before, the uncertainty in terms of pumping conditions primarily lead to the discrepancies between piezometric records and simulation outcomes. For instance, *piezometers 25392008* (Figure 3.4B) and *25392011* (Figure 3.4A) are spatially close. The corresponding piezometric records suggest that this area experienced more intensive pumping after 1988. However, Figure 3.3 shows that the estimated extraction rates significantly dropped during the 1990s, which explains why the model fails to align with the piezometer. *Well 25393055* recorded a head recovery, whereas the simulation assumes pumping activities nearby, and InSAR measurements also indicate a huge subsidence rate (larger than 7 cm/yr) in this area over the 1990s and 2000s.

3.3.2 Geomechanical Behavior

The outcomes of the coupled model in terms of land displacements are discussed in this section. In the following, vertical displacements are denoted by u_z, while the modulus of horizontal displacements, which includes the displacements in both east-west and north-south directions, are denoted as $u_h = \sqrt{u_{ew}^2 + u_{ns}^2}$. Due to variations in reference years across datasets, Δu_h

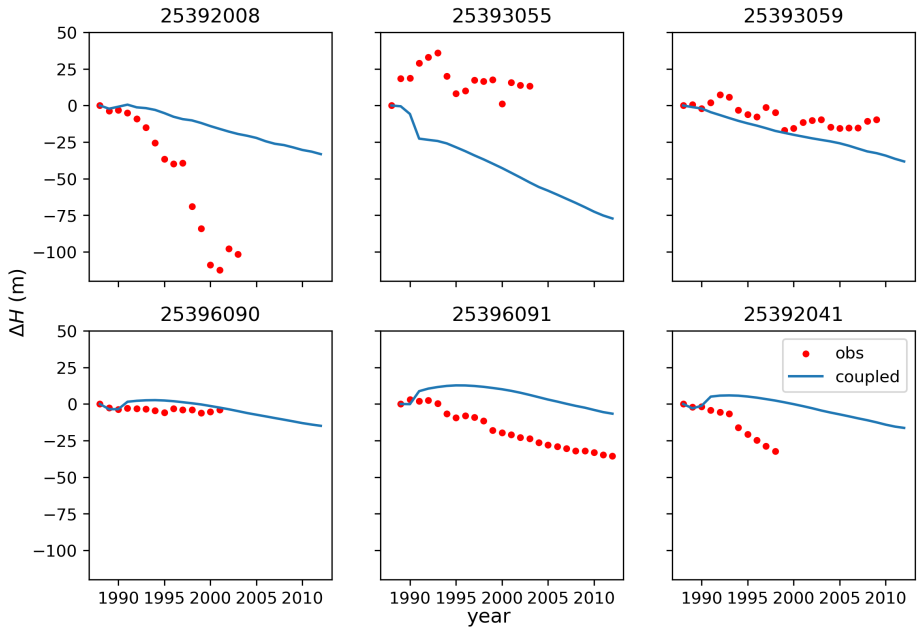

Figure 3.19: Comparisons between coupled model outcomes and piezometric records on ΔH from 1988 to 2012 at six validation wells are shown in Figure 3.4B. Notice that *well 25390241* is the only one with records available since 1972 (Figure 3.16).

may assume negative values when indicating a reduction in horizontal displacement relative to the preceding interval. Average displacement rates over a certain time interval are denoted as v_z and v_h.

In agreement with the hydraulic head drop, the maximum land subsidence over the period between 1962 to 1988 is computed in the southern clay areas (Figure 3.20A), with an average subsiding rate reaching up to 10 cm/year. Figure 3.20B shows that the area surrounding the subsidence bowl is also affected by horizontal displacements at rates up to 1 cm/year. Notice that no measurements are available to evaluate the reliability of these amounts.

After the year 1988, stringent regulatory measures were instituted to limit groundwater withdrawals. A notable number of extraction wells, especially those situated in the southern sector of the valley were closed. Despite the reduction in total extraction volumes, groundwater withdrawal intensified from the wells in the northern basin. This unsustainable use of the subsurface resources continued to cause a further decline of the piezomet-

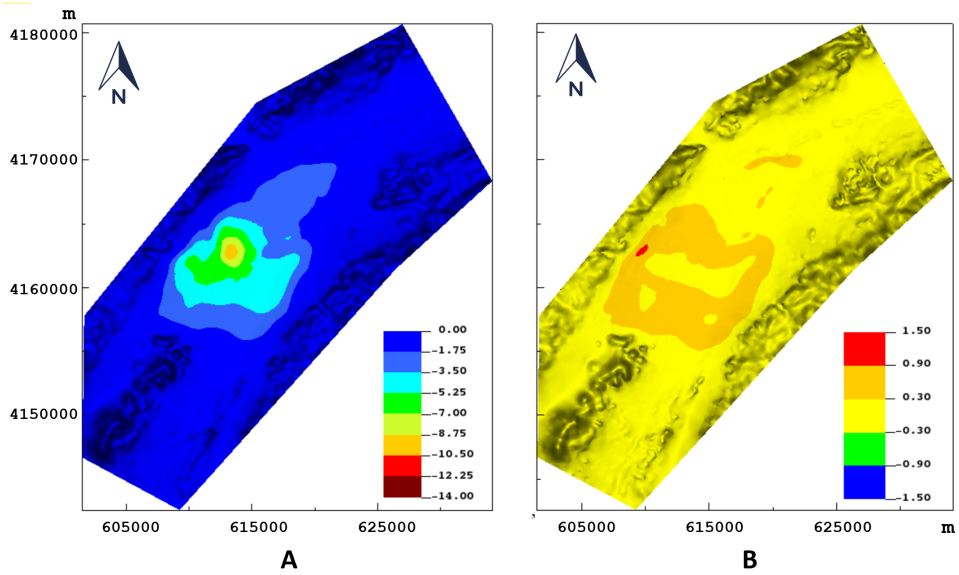

Figure 3.20: Average displacement rates (cm/yr) as computed by the coupled model over the period from 1962 to 1988. A) Vertical movements v_z, and B) horizontal movement v_h.

ric levels, especially in the northern basin, thereby triggering subsidence in this region. Between 1992 and 2007, the average rate of land subsidence as computed by the coupled model reached up to 14 cm/yr (Figure 3.21A), in agreement with InSAR measurements (Figure 3.5A). The most significant horizontal displacements around the subsiding area amounted to approximately 1.5 cm/yr (Figure 3.22A), i.e. about one order of magnitude smaller than v_z.

From 2007 to 2010, groundwater extraction persisted at a rate of 4.3×10^7 (m^3/yr) (Figure 3.3), leading to a further decrease in hydraulic head and resulting in a peak subsidence rate of 15 cm/yr (Figure 3.21 B). The rate of horizontal displacements stabilized with a certain southward shift corresponding to areas experiencing the steeper gradients of land subsidence (Figure 3.22B). Both drawdown and land subsidence rates experienced a progressive increase during this timeframe.

A decline in extraction rates was recorded after 2010 Figure 3.3), which was responsible for a slight reduction in land subsidence rates, particularly within the northwestern extents of clay deposits (Figure 3.21C). Notice that land subsidence amounts are directly correlated with the thickness of the clay

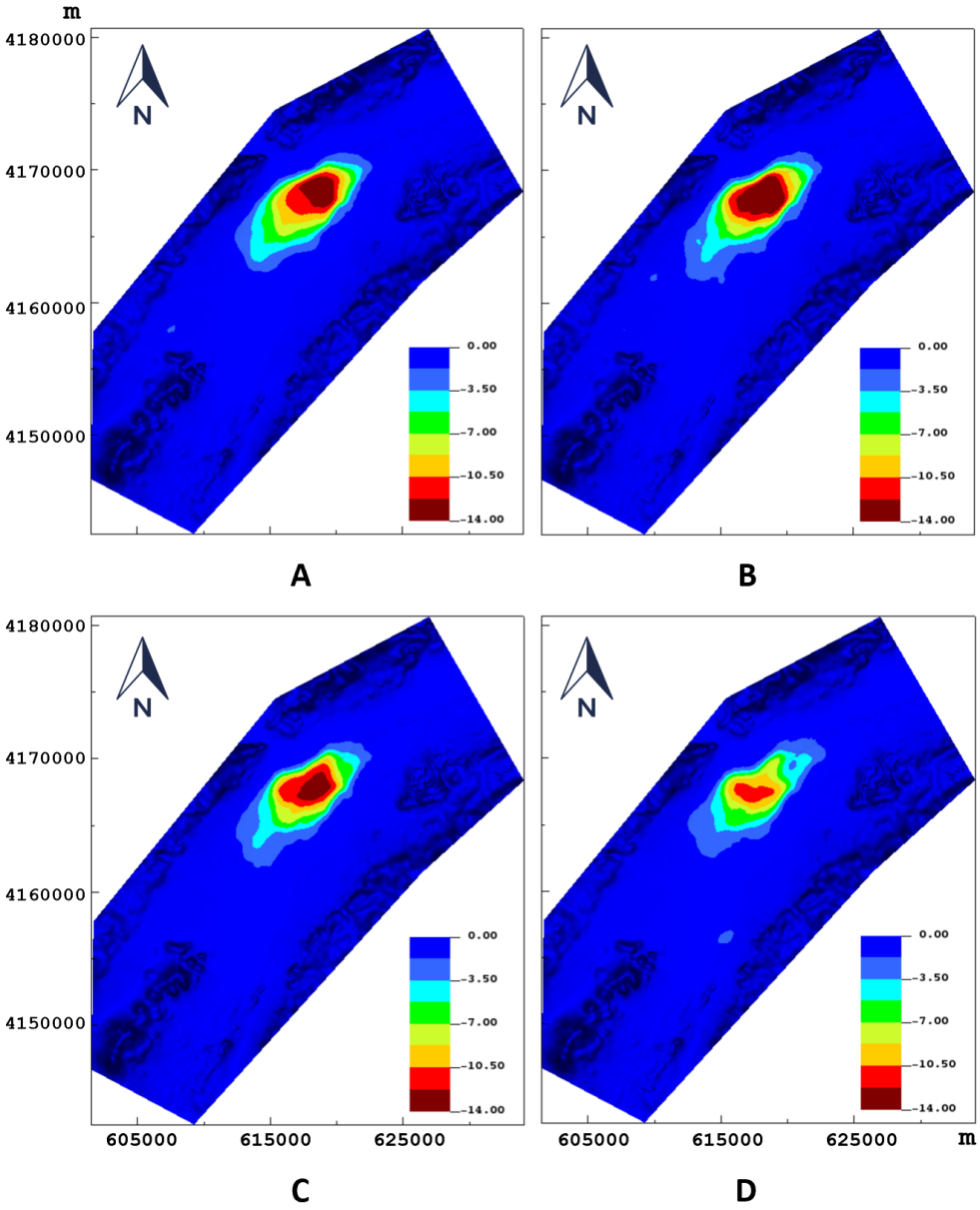

Figure 3.21: Average vertical displacement v_z (cm/yr) as computed by the coupled model over the four periods monitored by InSAR: A) 1992-2007, B) 2007-2010, C) 2011-2012, and D) 2012-2016.

unit. The maximum horizontal displacements predominantly occurred along southwest-northeast alignments in correspondence to the clay boundaries (Figure 3.22C). During the period between 2012 and 2016, the effects of the reduction of aquifer exploitation became evident. Average subsidence rates exhibited appreciable reductions with maximum annual rates decreasing to approximately 11.5 cm/yr (Figure 3.21D). Similarly, the horizontal displacement rates decreased from an annual rate of 1.5 cm/year to approximately 1.1 cm/year (Figure 3.22D), with a reduction also of areas experiencing the movements.

Recently, Bru et al. [2022] processed Sentinel-1 images acquired in ascending and descending orbits over the period 2015-2021. Decomposition of the LOS displacements has allowed us to derive the average displacement rate along the west-east direction. Figure 3.23 compares these v_{we} measurements with the same displacement rate as computed by the model over the period from 2012 to 2016. Although the two-time intervals do not overlap, the displacement pattern and amount are in good agreement, supporting the validity of the model calibration.

The cumulative vertical and horizontal displacements as computed by the coupled model over the whole simulated period between 1962 and 2016 are presented in Figure 3.24. The coupled hydrogeological model successfully represented the two main subsidence bowls corresponding to the two separate extraction phases (Figure 3.7). It is evident that spatial characteristics of clay, most notably its thickness, exert a predominant influence on patterns and magnitudes of land subsidence compared to hydraulic head decline. In summary, the results derived from the coupled simulation suggest that the total land subsidence reached an impressive amount of 4.7 m. The maximum horizontal displacements peaked at 0.6 m at the inlet of the Guadalentín river in the valley, i.e. in correspondence with the city of Lorca.

Furthermore, Figure.3.25 shows the porosity distribution on a representative vertical section at the beginning and the end of the simulation. As indicated by Eq. 2.9, porosity generally decreases within the Quaternary fillings due to the declining pore pressure and consequent deformation. This is particularly particularly notable within the lower portion of the clayey layer, which is closed to the exploited aquifer. The cumulative volume loss resulting from compaction is estimated around 2.2 km^3, obtained by summing the product of volume and porosity reduction over all elements in Quaternary fillings. This reduction in porosity undermines the permeability of soil,

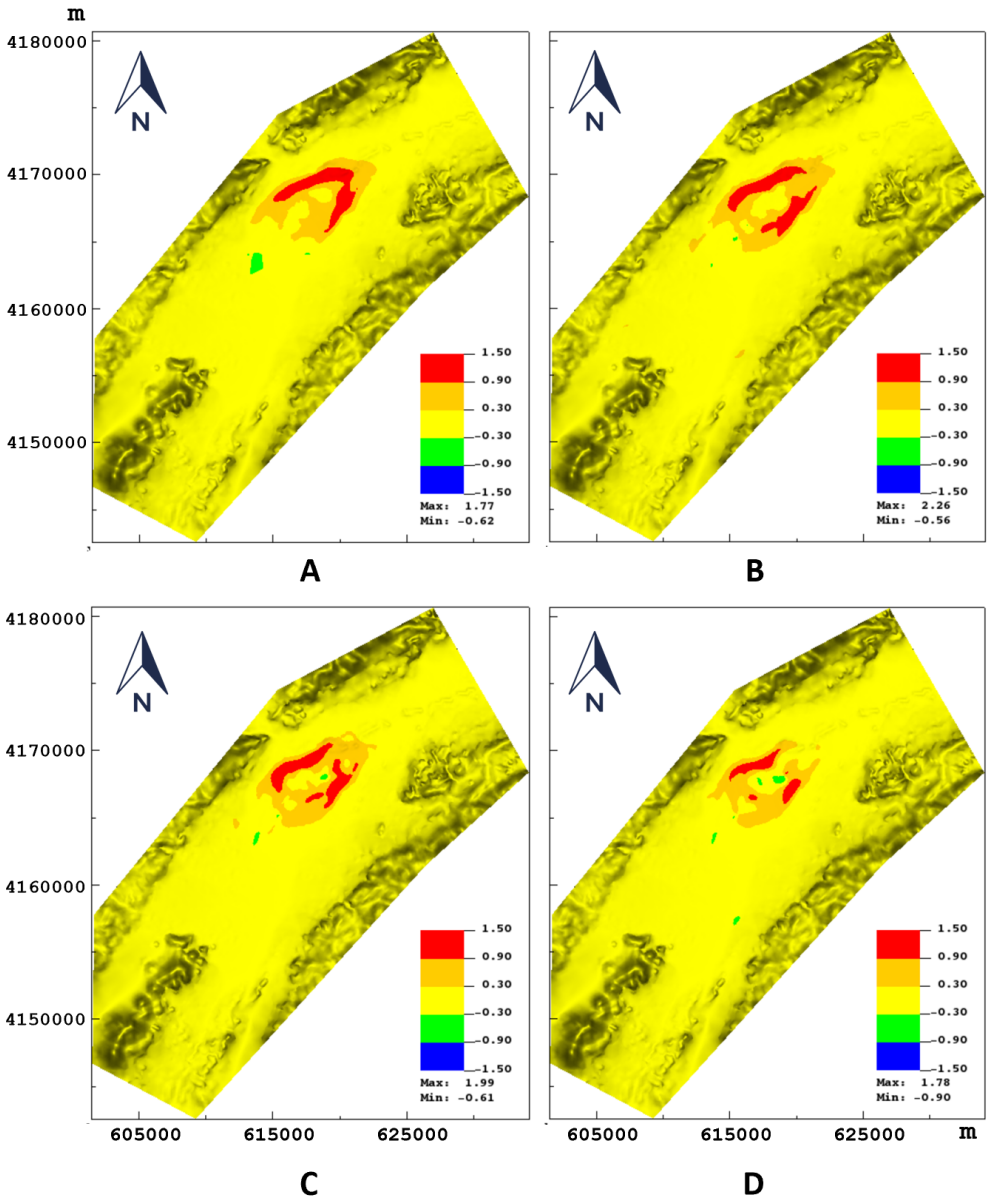

Figure 3.22: Average horizontal displacement v_h (cm/yr) as computed by the coupled model over the four periods monitored by InSAR: A) 1992-2007, B) 2007-2010, C) 2011-2012, and D) 2012-2016.

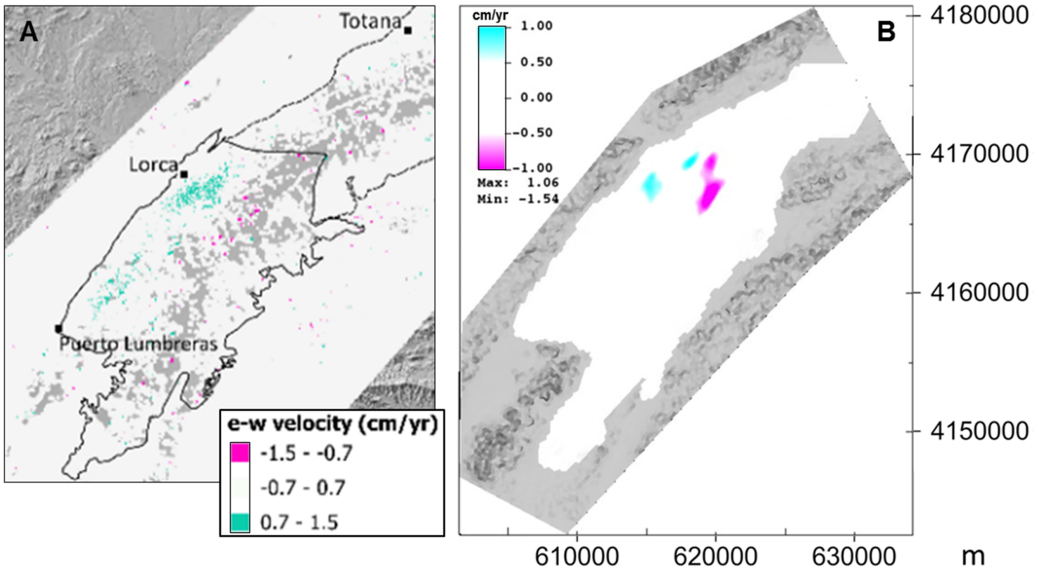

Figure 3.23: Average west-east displacement v_{we} (cm/yr) A) as derived from InSAR by Bru et al. [2022] on Sentinel-1 images acquired from 2015 to 2021 and B) by the coupled model over the period between 2012 and 2016.

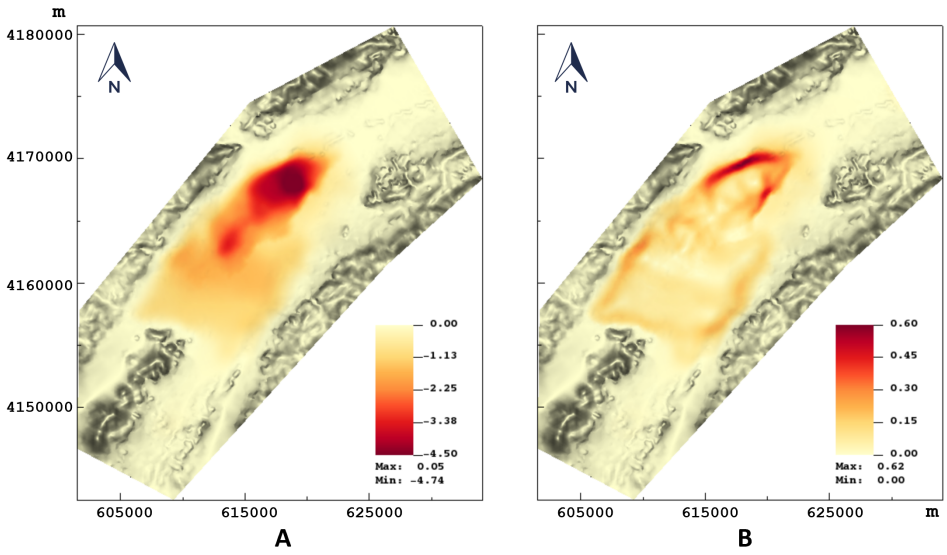

Figure 3.24: Cumulative A) vertical (u_z) and B) horizontal (u_h) displacements (m) as computed by the coupled model from 1962 to 2016.

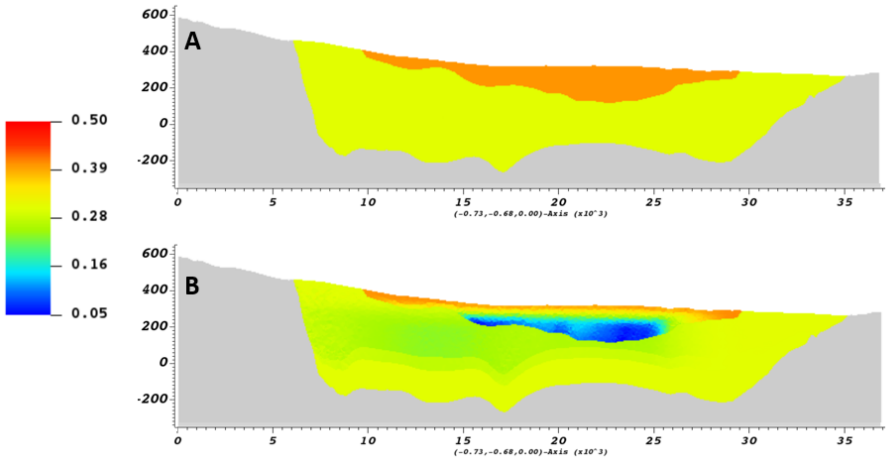

Figure 3.25: Porosity ϕ along the profile indicated in Figure 3.4B) in A) 1962 and B) 2016. The grey areas denote the bedrock.

demonstrating why the coupled model is attributed to higher permeability but predicts gently greater decline in hydraulic head compared to the GW solutions, as shown in Figure 3.16. The findings presented herein highlight the bidirectional relationship between hydraulic dynamics and aquifer deformation: not only the former exert an influence on the latter, but alterations in aquifer porosity due to soil deformation also affect the hydraulic dynamics.

Finally, Figure 3.26 shows a comparison between the simulated and observed vertical displacement rates at the 39 observational points highlighted in Figure 3.6. Notice that in Figure 3.26 the abscissa in the left row represents the sequence of observational points and not a temporal progression or coordinates. The figure demonstrates that the simulation results capture both the general spatial distribution and magnitude of the vertical displacements recorded by satellite observations, especially during the first three InSAR periods.

The comparison of the spatial distribution of land subsidence over the four-time intervals (Figure 3.26) suggests that the area affected by the loss of land elevation did not change significantly over time, with the land subsidence magnitude strongly correlated with the clay thickness.

A certain discrepancy between the model outcome and InSAR data is also evident in Figure 3.26. The green-shaded areas depicted in the first

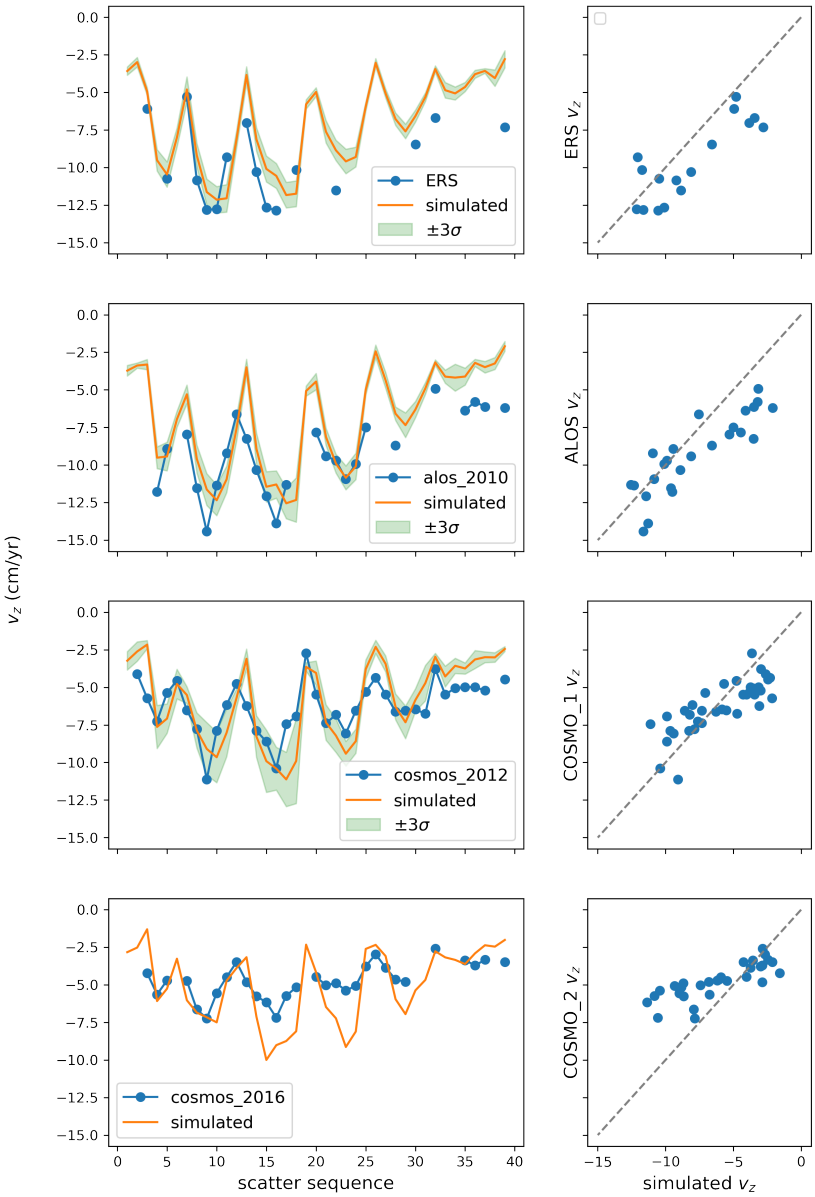

Figure 3.26: Comparisons between the numerical outcomes and InSAR measurements in terms of subsidence rate v_z on the 39 observation points shown in Figure 3.6 over the four InSAR spans: 1992-2007, 2007-2010, 2011-2012, and 2012-2016. The left panels presents observed and simulated v_z in spatial sequence. Green-shaded bands in the three periods used for the inversion represent the 3-standard deviation interval of QoI, i.e., $\mu \pm 3\sigma$, obtained using surrogate predictions on Markovian samples. Subplots in the last row represent the behavior during the validation period in which the surrogate model is not available to compute the model uncertainty.

three rows of Figures 3.26 represent the 3 standard deviation interval associated with the mean, i.e. the 99.7% of the model outcomes lie within this interval, as calculated using surrogate modeling with Markovian samples. Observations falling outside these bounds (green areas) mainly correspond to points with a number ID greater than #30. There is an underestimation of subsidence in the southern portion of the sinking zone. These discrepancies may be attributed to factors related to model configurations, such as underestimation of the clay thickness or pumping rates in this local area.

The marked decrease in subsidence rates observed in the COSMO-SkyMed image implies a substantial reduction in groundwater extraction rates, potentially allowing for pressure head recovery and deceleration of delayed compaction within low-permeability clay layers. It is plausible that current model assumes overestimated extraction rates, yielding simulated subsidence larger than observed. Alternatively, the aquifer system is regarded as elastic materials with constant compressibility, overlooking the fact that soil may become stiffer after long-term compaction. This oversight could lead to an exaggeration of subsidence over time, particular during the last time period.

In summary, despite the discussed inconsistencies, there is general consistency between numerical simulations and observations concerning both patterns and magnitudes of land subsidence, a fact that corroborates the fidelity of calibration outcomes and endorses the integrated modeling approach employed herein. To enhance model accuracy, the incorporation of additional data such as current extraction volumes and extended InSAR datasets would be advantageous.

3.4 Discussion

The modelling study presented in this chapter has yielded significant insights into the spatiotemporal evolution of hydraulic head and land subsidence in the Alto Guadalentìn basin. The simulation reveals that hydraulic head drawdown affected only partially the clay layer from the 1960s to the 1980s, resulting in localized land subsidence only in the southwestern sector of the basin. However, after 1988, the drawdown began to influence the entire clay layer, causing significant subsidence rates. Over the monitored three decades, the cumulative land subsidence exceeded 3 m, as highlighted by the InSAR observations. From 1962 to 2016 the model predicts a maximum land subsidence of almost 5 m. Despite these substantial ground displacements,

structural damage to buildings was not observed and only some minor effects in terms of reduction of hydraulic efficiency of the drainage network were reported.

Because of the peculiarity of the case study, other researchers in the last few years have engaged in developing numerical models for simulating subsidence in the area. Ezquerro et al. [2017] used MODFLOW to simulate the pressure evolution in the aquifer system over the period from 1960 to 2012. They used a similar aquifer system geometry but heterogeneous distributions of the saturated hydraulic conductivity and elastic storage were implemented. Land subsidence was computed through an empirical relationship between groundwater changes, soft soil thickness, and surface deformation. This relationship has been validated with the displacement data from ERS and COSMO-SkyMed satellites. The resulting regression function is then used as an empirical subsidence model to estimate a first approximation of the deformation of the aquifer system since the beginning of the groundwater extraction, reaching 5.5 m in 52 years. This amount is in line with the maximum total land subsidence computed in this study.

Fernandez et al. [2018] computed surface displacement in the Alto Guadalentín basin using Geerstma's nucleus of strain model in a half-space. Given that Geertsma's model is linear and the entire subsurface was assumed to be isotropic, superposition is allowable. The computation of surface deformation was based on the superposition of many prismatic blocks within the compacting aquifer system. The joint inversion of LOS measurements acquired on ascending and descending orbits between November 2015 and February 2017 was used to estimate the volume changes of the water table (volume and geometry) assuming a given pressure change value equal to -3 MPa and aquifer compressibility.

More recently, Fernandez-Merodo et al. [2021] used MODFLOW to reproduce groundwater evolution in the aquifer system since 1960 and a generalized plasticity state parameter-based model calibrated on oedometer laboratory tests of compressible materials extracted from a 300-m drilled borehole located in the area of maximum subsidence to simulate land subsidence. Specifically, land subsidence was assessed through a partially saturated 1D vertical finite element model, solving Biot equations reproducing the slow vertical drainage and vertical consolidation processes with the clay unit. The 17-parameter dependent constitutive model and the pressure variation at the column bottom as obtained by MODFLOW were used to run the simula-

tion. Finally, the subsidence model was adjusted to match the displacement datasets acquired by ERS, ENVISAT, COSMO-SkyMed satellites and the global positioning system GNSS. The proposed calibrated subsidence model reproduced the 3.1 m subsidence monitored in the period 1992-2018, and quantifies historical subsidence (since 1960) in the Alto Guadalentín Basin area at around 5.8 m.

The model approach developed in this thesis appears to be the most comprehensive and effective. Along with the model by Fernandez-Merodo et al. [2021], this is the only approach that utilizes a physics-based model for both the hydrologic and geomechanical processes. Moreover, it is the only simulator that implemented a fully 3D approach, with a coupled scheme that links pressure change to deformation and this latter to variation of the hydrologic parameters. For instance, this coupling approach enables the estimation of storage capacity loss due to groundwater depletion across the entire basin. With respect to Fernandez-Merodo et al. [2021], it implements a much more simple constitutive model (3 parameters, i.e. c_{mc}, ν, and the ratio r between soil compressibility in loading and unloading condition, with respect to 17 parameters) that allows anyway to match satisfactorily the observed land subsidence. Moreover, the statistical framework allows quantifying the uncertainty associated with the key parameters governing the hydrogeomechanical response of the aquifer system, which are the hydraulic conductivity of the sandy unit and the oedometric compressibility of the clay formation.

Nonetheless, discrepancies between model predictions and observations suggest potential deficiencies in the current simulation ability to fully capture the complexity of the aquifer behavior. It is crucial to acknowledge inherent limitations and uncertainties associated with both modeling and observational data. For instance, predictions of drawdown and subsequent subsidence hinge on withdrawal conditions, particularly well locations and annual extraction rates, which were insufficiently detailed in this case study. The discrepancies between discharge and observations primarily contributed to disparities between numerical outcomes and piezometric levels, along with significant piezometer noise exceeding typical precision expectations, and the exaggerated subsidence observed in the most recent InSAR period.

On the other hand, the agreement between numerical outcomes and InSAR measurements regarding subsidence spatial distribution suggests limited spatial variability in hydraulic conductivity and oedometric compressibility. In other words, the uncertainty associated with withdrawal conditions

may surpass that of aquifer properties.

Furthermore, a linear constitutive law is adopted to describe soil deformation to reduce the complexity of the modeling approach. However, the assumption of compressibility independent of pressure may contribute to an overestimation of subsidence over time. Consequently, this simplification yields a final porosity smaller than the common range observed for clay, potentially resulting in an overestimation of storage capacity loss.

In conclusion, this study delineates a methodological approach for inverse estimation of principal parameters affecting land subsidence at a basin scale through a 3D poroelastic model accounting for aquifer compaction due to groundwater extraction. This methodology operates within a Bayesian framework employing Markov Chain Monte Carlo (MCMC) sampling algorithms facilitated by surrogate models alongside InSAR datasets for robust calibration metrics. The Alto Guadalentín basin serves as an illustrative case study where significant land subsidence has been recorded over recent decades.

Key findings from this research include:

1. Sparse grid collocation methods employed as surrogates for computationally intensive models have been demonstrated to be accurate; they enable enhanced approximation accuracy while maintaining computational feasibility, facilitating implementations of sampling-based approaches like MCMC algorithms.

2. Integration of piezometric data into GW models reduces uncertainties associated with hydraulic conductivity but may introduce bias if deformation effects on hydraulic dynamics are neglected; incorporating surface deformation measurements further diminishes parameter variability, highlighting the advantages of diverse measurement types in inverse and validation exercises.

3. Remote sensing techniques, particularly InSAR, significantly enrich the information available for aquifer characterization. The proposed inversion framework has successfully quantified the uncertainty of aquifer properties by incorporating the poroelastic model with InSAR measurements. Furthermore, the numerical solutions with inferred Maximum A Posteriori (MAP) hydraulic conductivity and compressibility allow for the reproduction of the fourth InSAR image. These satisfac-

tory outcomes demonstrate the great potential of this methodology for regional groundwater management.

Future research directions could encompass validating aquifer properties, inferring discharge conditions using more recent InSAR datasets to improve the knowledge of the study area and investigating other constitutive laws to precisely characterize aquifer deformation. Methodologically, improvements could include addressing heterogeneities in aquifer properties such as permeability through controlled synthetic cases; and integrating model inadequacy into inversion frameworks to enhance the reliability of outcomes.

Chapter 4

Storage Quantification in Heterogeneous Compacting Aquifers

This chapter introduces an original methodology designed to address this issue in cases where InSAR measurements are available. The use of this EO product is particularly effective in characterizing the heterogeneous distribution of aquifer properties, primarily the elastic storage S_s (or oedometric compressibility c_m). In fact, it must be noticed that the mechanical response of an aquifer system is more sensitive than the hydrologic response to S_s. Therefore, measurements derived from InSAR above exploited aquifers are valuable information to infer soil compressibility if pressure variations are available. This is especially important for aquifer systems where field characterization, e.g. through pumping tests, and lab testing, e.g. through oedometric tests, lack or are scarce.

Central to the proposed approach is the application of Kriging, a geostatistical predictor that treats parameters as Gaussian processes. The strength of Kriging lies in its capacity to provide a mathematical formulation that facilitates the interpolation of variables across a spatial domain. It utilizes the measurement covariance structure to estimate unknown values based on the spatial correlation of available observations. Observation availability is mandatory to use Kriging, and this study incorporates

the use of Terzaghi's one-dimensional consolidation equation as a way to analytically derive "measurements" of S_s from InSAR outcomes.

The effectiveness of the proposed framework is illustrated and tested to estimate the spatial distribution of S_s in the confined aquifer system of the Gediz River Basin (GRB) in Turkey. Firstly, the chapter provides a general overview of the study area, followed by a description of the numerical modelling used to simulate the hydrologic and geomechanical behavior of the area and how Kriging is operated within this research context. Finally, the integration of the estimated S_s distribution into a 3D bi-elastic GM model (see Section 2.1.2) allows to compare the simulated land subsidence rates to the actual InSAR-derived subsidence data.

The proposed approach and the outcomes achieved are the basis of the publication entitled "Characterizing hydro-geomechanical properties of ungauged aquifer systems by InSAR-based land subsidence observations" by Li Y., Elçi A., Caylak B., Zoccarato C., C. Meisina, and Teatini P. in preparation for submission to *Hydrogeology Journal*.

4.1 Hydrogeological features of the Gediz River Basin

The Gediz River Basin, situated in western Turkey (Figure 4.1A), derives its name from the primary river within its expanse, the Gediz River, which extends approximately 400 km along a west-east direction.

This region typifies a Mediterranean climate, characterized by warm and arid summers, with cold and rainy winters. The average annual temperature stands at 15.2°C, and the basin experiences an average annual precipitation of 617 mm, as reported by [Elçi et al., 2015]. Precipitation exhibits variability across the basin, ranging from 440 to 672 mm annually. January and February notably experience the highest precipitation, whereas July and August emerge as the driest months.

This study focuses on the alluvial aquifer located in the easternmost part

of the basin, covering an area of approximately 320 km^2. The alluvial aquifer is affected by significant land subsidence, mainly attributed to extensive groundwater extraction for agricultural purposes. Aligned in the WN-ES direction, the alluvial aquifer corresponds to the underlying Gediz Graben, also recognized as the Alasehir Graben. The basement rocks of the graben consist of Paleozoic-aged metamorphic gneiss, schist, and marble derived from the Menderes Massif. These metamorphic rocks are widespread along the perimeters of the alluvial aquifer (Figure 4.1C), except for the northwest boundary that intersects the GRB basin. Bounded by active faults, the study area is frequently affected by earthquakes.

The alluvial aquifer encompasses Neogene and Quaternary sedimentary layers, with the thickness of the alluvial sediments ranging from 20 to a maximum of 320 m. These sedimentary layers predominantly comprise sandstone, conglomerate, claystone, limestone, and volcanic layers. Quaternary unconsolidated deposits blanket these formations throughout the plain, consisting of clay, clayey sands, and gravel [Hacıoğlu et al., 2021, Üner and Dogan, 2021].

The primary surface runoff in the alluvial aquifer is contributed by the Alasehir Creek, which also serves as a main tributary of the Gediz River. Within the study site, Alasehir Creek converges with three minor tributaries. The alluvial aquifer system in the GRB relies primarily on two groundwater recharge sources: surface recharge from precipitation and lateral recharge originating from the surrounding mountains enclosing the alluvial plain (Figure 4.1B). Both forms of recharge exhibit evident seasonal variability, influenced by the climatic conditions of the area. Additionally, the return flow from irrigation practices constitutes a significant recharge source to the aquifer system.

The alluvial aquifer system has been reconstructed from a number of borehole stratigraphies and geophysical sections scattered throughout the valley Navarro-Hernández et al. [2023]. The multi-aquifer comprises five hydrogeological units. Beginning from the top, the uppermost layer (L1) represents a permeable unconfined aquifer consisting of silty sand materials. Layer L2, situated beneath L1, comprises clays and sandy clay materials, forming a confining layer. The subsequent aquifer layer (L3) is permeable, and primarily composed of sand and gravel. Below L3, layer L4 acts as a confining layer made up of sandy clay. The deepest aquifer unit (L5) is a clayey gravel layer. The alluvial system is bounded to the North-West,

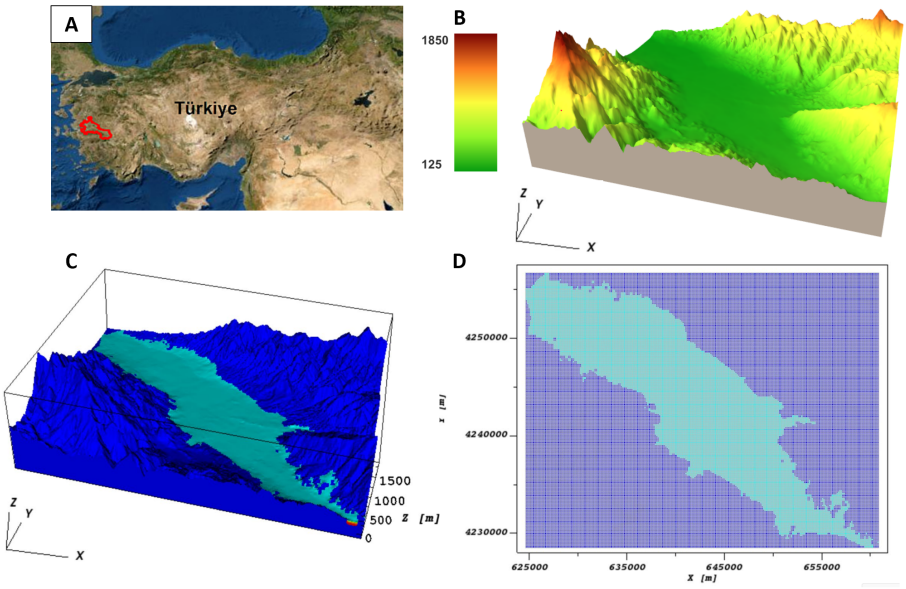

Figure 4.1: A: Location of the Gediz River Basin (GRB) denoted by a red polygon. B: Digital elevation model (m above msl) of the study domain. C: Conceptual model of the study domain with the alluvial system in light blue and the surrounding mountain ranges in dark blue. D: horizontal discretization of the study domain.

South-East, and at the bottom by rocky mountain ranges The DEM of the area was derived from SRTM (https://www2.jpl.nasa.gov/srtm/).

Groundwater extraction in this region is primarily for agricultural irrigation purposes, followed by supplying drinking water to urban areas, and lastly, industrial use. However, a notable challenge in this study arises from the lack of knowledge regarding the actual annual pumping amount, as a considerable number of irrigation wells operate without proper licenses. According to SYGM [2017], the estimated groundwater-dependent water demands for both urban and rural areas in the larger Alasehir-Sarigol sub-basin, extending beyond the model domain, amount to $2.48 \cdot 10^7$ m^3/yr. Furthermore, the estimated groundwater demand for irrigation purposes in the basin is approximately $3.58 \cdot 10^7$ m^3/yr, based on an irrigated land area of 6050 hectares. The water demand estimation for animal husbandry and industrial processes amounts to $2.90 \cdot 10^6$ m^3/yr and $1.90 \cdot 10^6$ m^3/yr, respectively.

Groundwater depletion is considered the primary cause of land subsi-

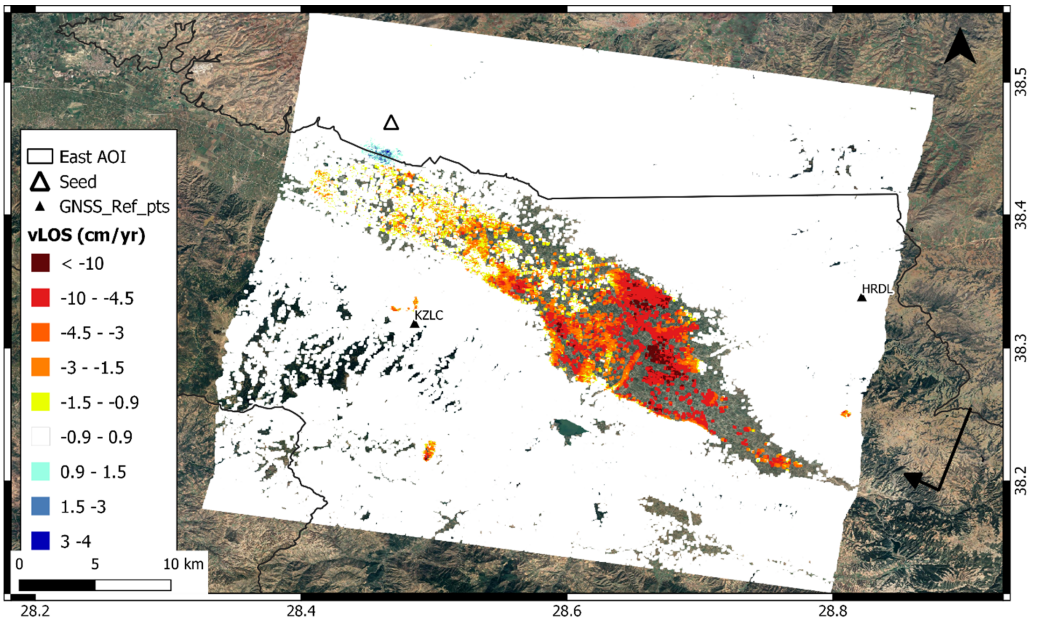

Figure 4.2: Average LOS displacement rate (v_{LOS}) obtained from a stack of descending 158 Sentinel-1 images acquired between January 2019 and August 2021. The CPT InSAR processing chain [Blanco-Sánchez et al., 2008] was used. After Bru et al. [2021].

dence in the valley despite intense tectonic activity. Navarro-Hernández et al. [2023] used independent components analysis to identify two spatiotemporal displacement trends from the InSAR time series: the primary trend is positively correlated to the soft soil thickness, while the other shows significant seasonal fluctuations that correspond with the seasonal recharge. The InSAR processing by Bru et al. [2021] detects a LOS (line of sight) peak equal to -18.9 cm/yr in the center of the alluvial basin (Figure 4.2), i.e. far from the main faults distributed along the mountain foothills, further supporting that groundwater withdrawal is the main process responsible for land subsidence.

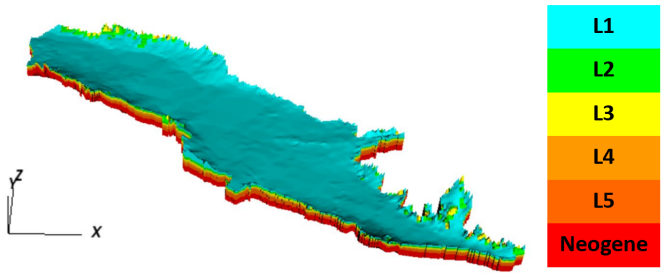

Figure 4.3: GW grid (active cells) representing the GRB alluvial aquifer system.

4.2 Numerical Modelling

4.2.1 Groundwater Flow Model

The groundwater flow model of the GRB was developed by Dokuz Eylül University (DEU), Turkey. The 3D simulated domain takes the form of a prismatic volume, with the lateral constituted by the rock ranges, representing a no-flow condition (Figure 4.1C).

The domain is vertically discretized based on aquifer layering and horizontally by uniform 150 × 150 m squares, resulting in 188 rows and 242 columns (Figure 4.1D). Overall, the grid is made of 227,480 cells, 70,088 of which are active. The alluvial aquifer system as represented in the GW model is provided in Figure 4.3. The simulated period spans from October 2013 to December 2022, i.e. including the entire period monitored by InSAR, with a 1-month time step to accurately capture the seasonal fluctuation of precipitation. Rainfall represents a main component of the water balance in this case.

The GW simulations are carried out using ModelMuse [Winston, 2022], applying various packages to characterize different boundary conditions [Elçi et al., 2022]. The lateral boundary of the alluvial aquifer is prescribed as general-head boundary (GHB) with specified head and conductance. The Recharge (RCH) package is employed to delineate primary recharge sources. The behavior versus time and space of monthly recharge is derived through a water balance approach supported by EO data, with precipitation provided by two meteorology stations, actual evapotranspiration derived from Terra Net Evapotranspiration database, changes in soil water content and surface

runoff obtained from ERA5-Land products processed using Google Earth Engine scripts. The average annual recharge obtained for the study area is 72 mm/yr. River recharge including Alasehir Creek and other branches, are delineated by the River (RIV) package.

Discharge primarily occurs through pumping wells, classified into two types: irrigation wells and public water supply (PWS) wells. All pumping wells are assumed to withdraw water from layers L3 and L5, given the high permeability of these units. PWS well locations are accurately documented, and pumping rates are approximated based on population data. However, the challenge arises with irrigation wells, as most are unlicensed, requiring estimation of both locations and pumping rates. For simplicity, irrigation wells are uniformly distributed across the alluvial aquifer area, and production rates are obtained through interviews with local farmers. Further details on each boundary condition setting are available in Elçi et al. [2022].

The initial hydraulic head distribution is obtained by running a separate transient simulation of the same model for a warm-up period of 4 years, implementing recursive hydrologic conditions from the first simulation year. The flow model was calibrated using the PEST parameter estimation computer code [Doherty, 2003], with Tikhonov regularization implemented to improve numerical stability in over-parameterized inverse problems and the use of pilot points for the estimation of the spatial distribution of the aquifer hydraulic conductivity [Doherty et al., 2010]. Apart from the hydraulic conductivity of the aquifers and the compressibility of aquitards, other properties are considered to be homogeneously distributed. PEST is utilized to estimate the aquifer hydraulic conductivity and its anisotropy ratio, as well as the conductance of rivers and boundary conditions, using hydraulic head values measured over the selected time interval in 24 piezometers scattered in the study area.

4.2.2 Geomechanical Model

The geomechanical simulations are carried out using GEPS3D (Geomechanical Elasto-Plastic Simulator 3D), a simulator developed at Dept. ICEA, University of Padova (UNIPD), implementing tetrahedral and hexahedral finite elements [Isotton et al., 2019]. GEPS3D has been applied in various geomechanical studies over the last decades [e.g. Teatini et al., 2006a, 2011a, Ochoa-González et al., 2018, Ye et al., 2018, Zoccarato et al., 2019, Zhu

et al., 2020, Gazzola et al., 2023].

The geomechanical model is developed using the same static model as implemented in the GW model (Figure 4.4). The use of hexahedra, i.e. 8-node finite elements, has the matching of the geometry of the ModelMuse finite difference grid. Therefore, no interpolation between the pressure field computed by ModelMuse and that in input to GEPS3D has been required, thus keeping the solution accurate. A specific driver converting the finite different grid into the equivalent hexahedral mesh has been developed.

The need to prescribe the (null-displacement) boundary conditions sufficiently far from the bottom of the alluvial system has required the insertion of the Neogene stratigraphic unit (L6) below which the rock basement is located. The Neogene is composed of sandstone and conglomerate, making this layer barely contributing to aquifer recharge and land subsidence. Globally, the 3D GM model is made of 7 geologic (and FE) layers, totaling 363,968 nodes and 315,469 hexahedra (Figure 4.4). Notice that the bedrock bounding the alluvial aquifer system laterally and at the bottom is an "active" unit in the geomechanical computation, although characterized by a compressibility much smaller than that of the alluvial soils.

The aquifer deformation computed by the GM model is driven by the GW outcomes, specifically the pore pressure changes, which are explicitly prescribed as the forcing factor. The geomechanical model runs with a 1-month time step, consistent with the GW model. However, the time frame spanned by the former differs from that simulated by ModelMuse, as the InSAR displacement measurements cover only the period from January 2019 to August 2021, corresponding to the 63^{rd} and 95^{th} steps, respectively, in the GW analysis.

From the mechanical point of view, the GRB aquifer system is assumed to exhibit a bi-elastic behavior, where the compressibility value depends on the actual effective stress $\hat{\sigma}_v$ with respect to the pre-consolidation stress $\hat{\sigma}_{v,pre}$, i.e. the maximum vertical effective stress experienced by the soil. Meanwhile, the GW outcomes and piezometric records indicate a general decline in pore pressure head with significant seasonal fluctuations. To properly account for this trend in the head distribution, and consequently correctly initialize $\hat{\sigma}_{v,pre}$, it is decided to initiate the GM simulations two years before the first InSAR acquisition, i.e. in January 2017. This choice enables the proper characterization of loading/unloading conditions at the onset of the period monitored by InSAR and simultaneously reduces the computation burden

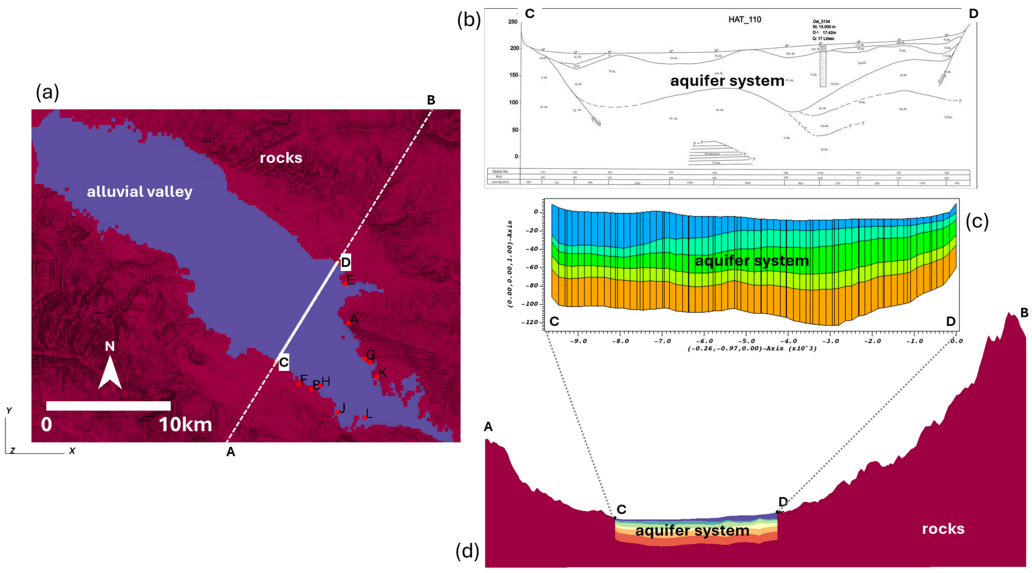

Figure 4.4: Set-up of the GM model of the GRB aquifer system. (a): Horizontal view of compressible (alluvial valley) and incompressible (rocks) materials. (b): Example of one of the geophysical sections (along alignment CD depicted in (a)) utilized to delineate the aquifer system architecture. (c) Aquifer system layering and discretization as implemented in the GW model along alignment CD depicted in (a). (d) Vertical section of the simulated domain along alignment AB depicted in (a). The "rocks" material represents inactive cells in the GW model and stiff FEs in the GM model.

required to solve a linear system with more than 1,000,000 unknowns.

As outlined in Eq. 2.16, the ratio r between compressibility in loading and unloading conditions is equal to 5. The aquifers are assumed homogeneous with $S_s = 10^{-4}$ m^{-1}, and the bedrock is homogeneous and elastic with $S_s = 10^{-8}$ m^{-1}. The specific storage of the aquitards (L2 and L4 layers), which is assumed heterogeneous, is derived using the procedure described in the following sections. The compressibility of grains and water is assumed negligible. The soil bulk density is set at 2,000 kg/m^3. The maximum (absolute value) σ_1 and minimum σ_3 principal stresses coincide with the vertical $\hat{\sigma}_v$ and horizontal $\hat{\sigma}_h$ stresses, respectively. The total vertical stress σ_v increases linearly with depth and the initial $\hat{\sigma}_v$ distribution is set as the initial pre-consolidation stress $\hat{\sigma}_{v,pre}$. Additionally, the ratio between $\hat{\sigma}_h$ and $\hat{\sigma}_v$ is fixed at $\nu/(1-\nu)$, with the Poisson ratio $\nu = 0.25$.

The following boundary conditions are imposed: null vertical displace-

ment on the model bottom, and null horizontal displacements on the model bottom and the lateral boundaries, while the model top is a traction-free surface.

4.3 Employed Strategy for Uncertainty Quantification

4.3.1 Rationale

The objective of the modelling study for the GRB is to quantify uncertainties in hydrogeological properties crucial for aquifer management and associated land subsidence, namely the hydraulic conductivity K_g of the main exploited aquifers (layers L3 and L5) and the specific storage S_{sc} of clayey aquitards (layers L2 and L4). As outlined in Eq. 2.6, the specific storage is linearly correlated to the oedometric compressibility c_m if the porosity ϕ is constant.

Despite sharing common aims, the GRB study differs significantly from the Alto Guadalentín study for several reasons. Firstly, upon cross-referencing the records of hydraulic head variations ΔH, thickness d of the layers constituting the multilayer system, and measured subsidence u_z, it becomes apparent that both K_g and S_{sc} in the RGB aquifer system should exhibit high spatial heterogeneity. This renders the earlier Bayesian scheme unusable due to the curse of dimensionality. Secondly, the study period for the RGB spans from 2013 to 2022, an 8-year interval during which ΔH has been considerably less than that recorded in the multi-decadal analysis carried out in the previous chapter for the Alto Guadalentín aquifer. This supports the assumption of using a constant porosity over time in the modelling approach. Lastly, the Spanish aquifer is predominantly a phreatic system, whereas the main developed units in Turkey constitute a confined multi-aquifer. Consequently, variations in saturation degree can be neglected in the latter case. As a result, also considering the outcomes from previous hydro-geomechanical analyses on large aquifer systems [e.g. Gambolati et al., 2000], the GW and GM models can be decoupled due to the limited feedback between hydraulic and mechanical behaviors over the decadal duration investigated for the GRB.

An iterative approach has been developed to optimally utilize the available measurements in constraining uncertain parameters (Figure 4.5). Specif-

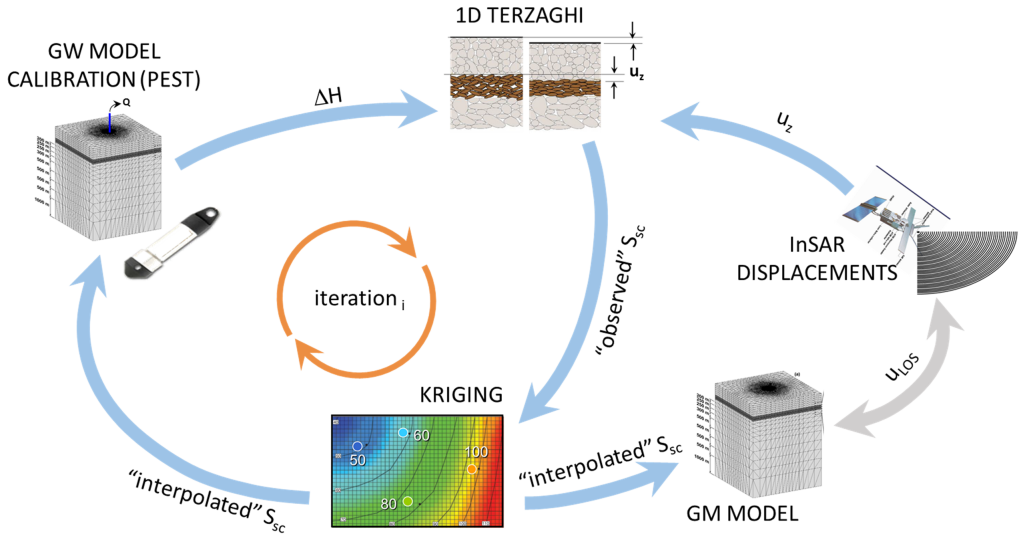

Figure 4.5: Workflow of the calibration procedure.

ically, piezometric head measurements collected at available piezometers provide fundamental information to quantify K_g through the GW model, given the linear dependence between ΔH and K_g in a confined aquifer system. Additionally, the displacement measurements of the land surface provided by InSAR are used in the GM model to constrain c_m, and consequently, S_{sc}, as u_z is linearly dependent on c_m in an elastic porous medium. The effort is a collaboration between DEU and UNIPD, with DEU applying the GW model and UNIPD applying the GM model. Here, the focus is on the methodology employed to estimate the statistical moments of S_{sc} by integrating "observation" of the specific storage with Kriging and the GW model.

The "observation" of S_{sc} are obtained by rearranging the one-dimensional (1D) Terzaghi consolidation equation [Terzaghi et al., 1996] as follows:

$$S_{sc} = \frac{u_z}{\Delta H \times d} \tag{4.1}$$

where u_z is the vertical displacement of a PS as measured by InSAR, ΔH is the hydraulic head change within the aquitards L2 and L4 as provided by the GW model with calibrated K_g in correspondence with the PS location, and d is the sum of the L2 and L4 thickness at the same location as readily derived from the mesh.

The use of Eq. 4.1 is based on the assumption that the contribution of aquifer compaction to the measured land subsidence is negligible, a premise

typically valid in shallow aquifer systems. Moreover, the compressibility of L2 and L4 are assumed to be equal. The uncertainty introduced by this 1D approximation is treated as measurement noise and assessed in the subsequent Kriging analysis. Assuming S_{sc} as a Gaussian random field allows for the efficient and accurate characterization of the spatial distribution of this aquitard feature interpolating the "observation" available at the PS locations. The Gaussian process in this chapter is assumed to be stationary and isotropic, implying that the correlation between any two points in the domain depends solely on their distance. Finally, both ΔH from the GW model and the mean distribution of S_{sc} are used in the 3D GM model to compute the 3D displacement field. The root mean squared error ($RMSE$) is adopted to evaluate calibration results and model accuracy quantitatively:

$$RMSE = \sqrt{\frac{1}{N_{mn}} \sum_{i=1}^{N_{mn}} (v_{LOS,meas} - v_{LOS,model})_i^2} \tag{4.2}$$

where N_{mn} is the number of monitoring nodes, $v_{LOS,meas}$ and $v_{LOS,model}$ are the average displacement rates along the LOS from January 2019 to August 2021 as provided by InSAR and the GM model, respectively. Thereafter, the mean and variance of updated S_{sc} are fed back to the GW model to start a new iteration.

4.3.2 Steps

Specifically, the developed procedure consists of the following steps:

1. Resampling the InSAR measurements on the mesh nodes. Unlike the pore pressure head variation ΔH and thickness d, the locations of InSAR PS points are not consistent with the mesh nodes. Therefore, resampling is necessary before using Eq. 4.1. Specifically, a mesh node is associated with the closest PS if their distance is less than 100 m, otherwise, no measurement is available on that node. The procedure is limited to the nodes on GW active cells. Consequently, a number of 5349 nodes with available displacement measurements are detected (Figure 4.6) and denoted as "nodes_initial".

2. Approximating ΔH at the "nodes_initial" over the period monitored by InSAR. Due to seasonal fluctuation, ΔH can not be simply derived as the differences between H in January 2019 and August 2021.

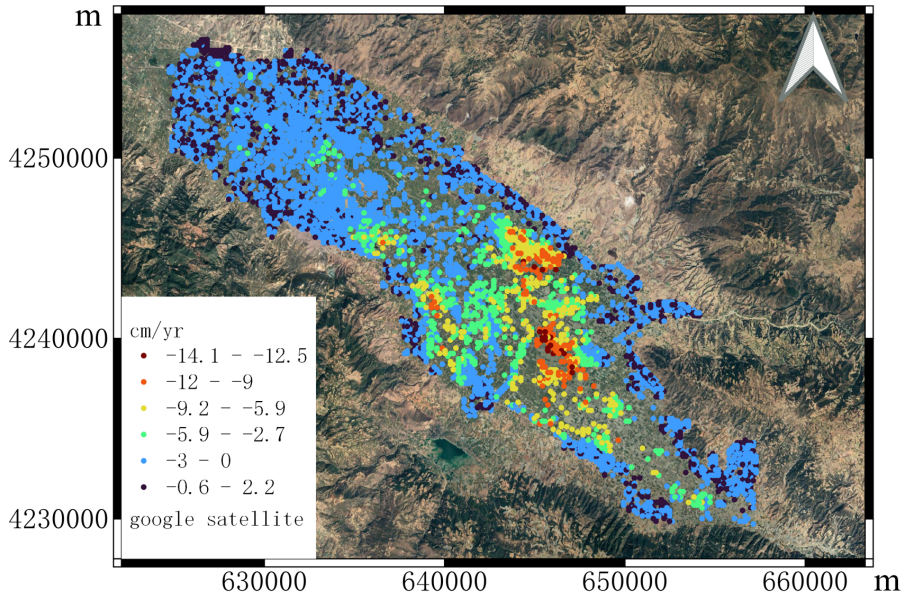

Figure 4.6: Average LOS displacement rate (v_{LOS}) between January 2019 and August 2021 as obtained from resampling the InSAR outcome (Figure 4.2) on the active nodes of the GW model. A number of 5349 nodes with measurable deformation were detected.

Meanwhile, involving the full-time series seems redundant in the implementation of Eq. 4.1. Therefore, the trend of ΔH is obtained by a linear regression model to exclude the seasonal pattern, as shown in Figure 4.7.

3. Estimating the minimal hydraulic head, namely $\hat{\sigma}_{v,pre}$, on the "nodes_initial" at the beginning of the InSAR monitoring interval. This is obtained by running the GM model over the January 2015-January 2017 "warm-up" period. It is important to note that ΔH over the InSAR time interval cannot suffice to establish the loading condition. For example, the hydraulic head at node #108715 in Figure 4.7 slightly drops within the InSAR interval, as indicated by the regression line, but shows a general recovery over the whole time interval. In such cases, compressibility in the unloading condition can be adopted, irrespective of the actual H between January 2019 and August 2021.

4. Computing S_{sc} on the "nodes_initial" and screening for consistency.

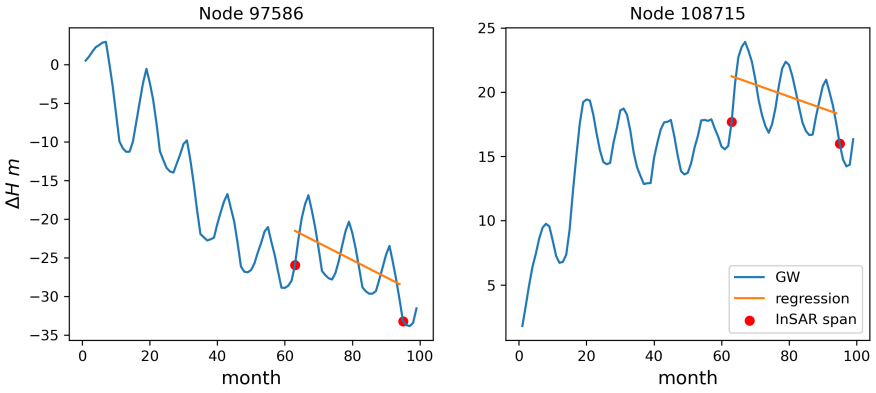

Figure 4.7: Evolution of ΔH obtained from the GW model (blue lines) and corresponding regression approximation (orange lines) for two representative nodes.

Eq. 4.1 is used to compute S_{sc} on the "nodes_initial", with d extracted from the mesh (Figure 4.3) and ΔH as provided by step 2. However, some unrealistic results occur. This happens when i) the sign of ΔH is inconsistent with that of v_{LOS} as provided by step 1 (for example, a decrease in hydraulic head corresponds to land uplift), and ii) ΔH takes a very small value leading to an unrealistically large S_{sc}. These nodes are ruled out and the remaining N_{mn} nodes are denoted as the "nodes_effective". Since the distribution of ΔH is updated by the GW model at each iteration, "nodes_effective" may differ at each iteration.

5. Applying the Kriging predictor to quantify the expected S_{sc} and its uncertainty over the whole domain. The fundamental idea is that S_{sc} at "nodes_effective" serve as "observation". Notice that $\log(S_{sc})$ is utilized to facilitate the computation. The hyperparameters in the trend and correlation functions must be estimated before implementing a Kriging predictor. More details about the estimation are provided in the forthcoming section. Subsequently, a Gaussian field of S_{sc} is obtained by the Kriging predictor where the uncertainty at unknown points can be characterized based on the field correlation as suggested by the "observation". The uncertainty refers to the key statistical moments of the field, i.e., the mean and variance.

6. Modelling the 3D geomechanical response of the GRB aquifer system.

The mean S_{sc} obtained in step 5 is viewed as the most likely distribution and is used in the 3D GM model together with the S_s deterministic value of aquifers and bedrock as defined in Section 4.2.2. GW model is run with the actual time series of ΔH as computed by the GW model. The computed displacements are projected along the InSAR LOS, and the quality of Kriging characterization is quantified by the $RMSE$ between the numerical solution and the InSAR outcome on the "nodes_effective".

7. Closing the iterative procedure. First, the outcomes of step 5, namely the spatial mean and variance values of S_{sc}, are used to re-run the GW model. A new K_g calibration and an updated ΔH are obtained. Before starting a new iteration, the GM model is re-run with the new ΔH and the latest S_{sc} and $RMSE$ is re-evaluated. Since this $RMSE$ is obtained before the calibration of S_{sc}, it is denoted as "$RMSE$-before", while the updated one, i.e., that computed through steps 2 to 6, is denoted by "$RMSE$-after" (Table 4.1). When $RMSE$-before and $RMSE$-after become sufficiently close, convergence is assumed to be achieved. Otherwise, a new iteration starts from step 2.

4.3.3 Specific Storage Mean and Variance by Kriging

The ordinary trend function and the Matern 5/2 correlation function (Eq. 2.65) are utilized to construct Kriging predictors which requires estimating the trend coefficient β_0 and correlation hyperparameter θ. It is important to note that here θ is a constant as S_{sc} is assumed to be horizontally isotropic. Table 4.1 provides a comprehensive summary of the Kriging parameters and $RMSE$ values at each iteration. Each row reports the number of "nodes_effective", the hyperparameter θ in the correlation function, the mean β_0, the noise variance σ_N^2, and the $RMSE$ values for every iteration. The iterative process concludes after four iterations, during which the difference ($RMSE$-before - $RMSE$-after) reduces to less than 0.5 mm/yr. An important note is that the iteration started with a homogeneous S_{sc} value of 0.001 m^{-1}, leading to an initial underestimation of the measured displacements (Figure 4.8A).

Figure 4.9 provides S_{sc} mean and variance distributions from the last iteration, where a number of 1931 "nodes_effective" are detected. The distribution of S_{sc} exhibits significant heterogeneity, varying up to three orders

Table 4.1: Kriging parameters and $RMSE$ values for each iteration of the developed procedure.

Iteration	N_{mn}	θ	β_0	σ_N^2	$RMSE$-before (mm/yr)	$RMSE$-after (mm/yr)
1	3346	0.173	-3.500	0.1367	3.34	2.11
2	2557	0.173	-3.500	0.1367	3.53	2.01
3	2445	0.173	-3.500	0.1367	3.40	2.54
4	1931	0.172	-3.672	0.1120	1.90	2.30

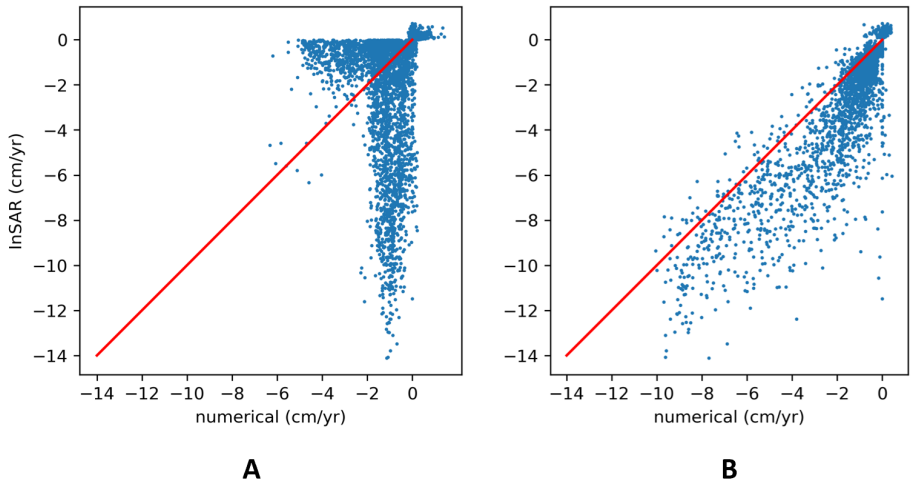

Figure 4.8: Measured versus computed v_{LOS}. A) Initial distribution as obtained with a homogeneous S_{sc}; B) Final distribution as obtained with the optimal distribution S_{sc} shown in Figure 4.9.

of magnitude. The mean distribution from Kriging correlates with the v_{LOS} distribution (Figure 4.6). For instance, areas with S_{sc} greater than 0.001 m^{-1} in the central portion of the basin experienced a v_{LOS} exceeding 10 cm/yr. Small spots with extreme S_{sc} values (larger than 10^{-2} m^{-1} and smaller than 10^{-5} m^{-1}) are associated with small ΔH and v_{LOS}, respectively. Regarding variance, it primarily depends on the distribution of "nodes_effective", with smaller uncertainty in areas with denser "observation".

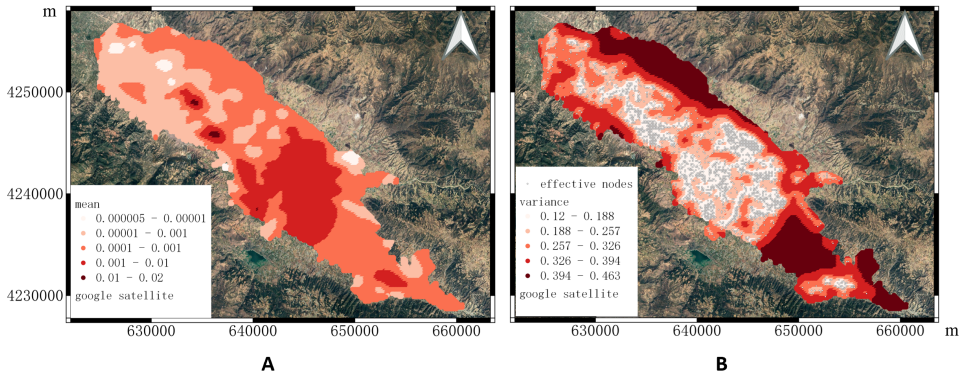

Figure 4.9: Distribution of A) expected and B) variance of S_{sc} as obtained by the calibration procedure. The black dots in B denote the "nodes_effective" locations.

4.4 Numerical Outcomes

Figure 4.10 shows the GW outcomes from the last iteration, presenting ΔH over the time interval spanned by InSAR for aquifer L2 and aquitard L3. The pattern of ΔH is quite consistent across all layers, with the largest hydraulic head decline, up to 20 m, in the northwestern portion of the GRB and much smaller in the central area. Notably, a certain head increase in the southeastern sector could be attributed to lateral recharge.

Figure 4.11A depicts the average displacement rates along the vertical direction as computed by the calibrated GM model over the monitored InSAR time interval. The results reveal significant land subsidence in the central portion of the basin, aligning well with the InSAR measurements (Figure 4.6). The maximum subsidence rate reaches 14 cm/yr.

Furthermore, the 3D GM simulator enables the quantification of the horizontal components of the land displacement as well. Figure 4.11B shows the average rate of the modulus of horizontal displacements, revealing smaller magnitudes compared to vertical displacements. The maximum values, around 0.4 cm/yr, are concentrated along the edges of the subsidence bowls, coinciding with the regions affected by the greatest displacement gradients.

The vertical displacement exhibits an evident seasonal fluctuation (Figure 4.12), corresponding to the evolution of ΔH (Figure 4.7). It is interesting to note the variation of the descending slope showing the influence of the preconsolidation stress on the behavior of aquifer deformation. Moreover, the

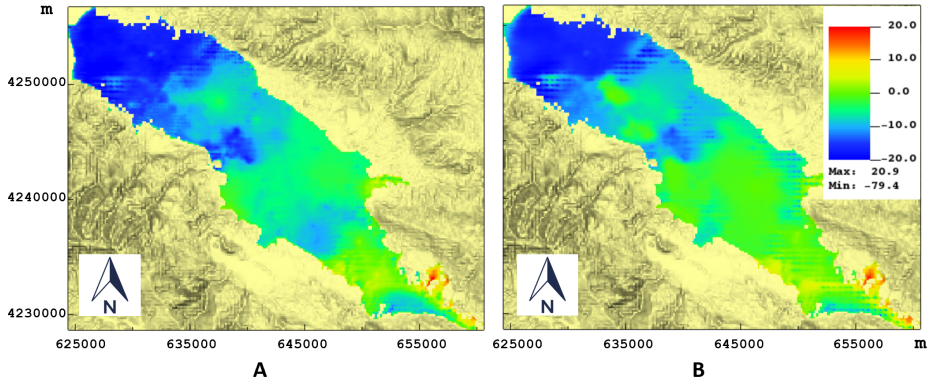

Figure 4.10: Hydraulic head change ΔH (m) as obtained by the calibrated GW model A) within aquifer L2 and B) within aquitard L3 over the time interval spanned by the InSAR analysis.

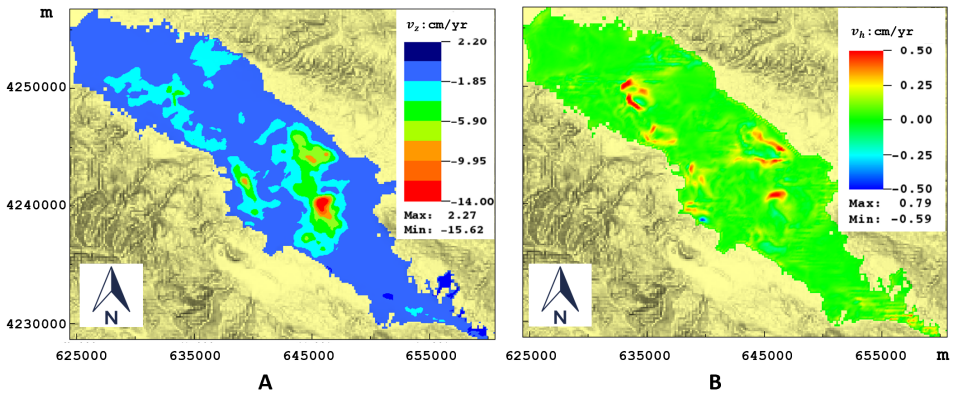

Figure 4.11: Simulated displacements as obtained by the calibrated 3D GM model: A) average rate along the vertical direction (v_z: cm/yr) and B) average rate of the modulus of the horizontal displacement (v_h: cm/yr).

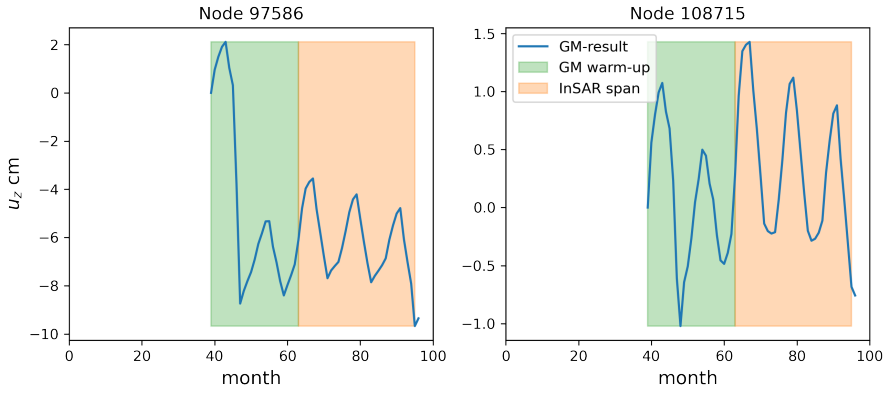

Figure 4.12: Evolution of simulated vertical displacement u_z at nodes 97586 and 108715

effect of updating $\hat{\sigma}_{v,pre}$ from the initial value during the "warm-up" period is obvious from the exaggerated land subsidence at node #97586 during the first phase of hydraulic head reduction. Consequently, it is important to focus on the state variables only within the interval spanned by InSAR, which is indicated by an orange block in Figure 4.12, rather than considering the entire temporal behavior.

The comparison of measured versus simulated LOS displacements, with the latter provided by the calibrated models, is presented in Figure 4.8B. The figure suggests a satisfactory match, with a significant improvement of the initial condition (Figure 4.8A). However, the GM model slightly underestimates the measured displacements. This can be attributed to several factors. First, discrepancies between the distributions of ΔH and InSAR measurements. The GW outcomes provide hydraulic head declines smaller than 2 m where InSAR measures LOS rate larger than 10 cm/yr, suggesting unrealistic large S_{sc} that have been manually bounded. Second, the 1D Terzaghi's consolidation equation assumes the deformation at each node is independent of that of the surrounding nodes. This contrasts with the 3D GM simulation, where the motion of a node is affected by those of the nearby nodes due to continuity. Thus, the 3D model tends to smooth the displacement field. This preference for smoothness is also evident in Kriging's estimation, which perceives extreme values of S_{sc} as noise and corrects them toward the mean.

Table 4.2: Hydraulic properties of each hydrogeologic unit as obtained at the end of the calibration procedure.

Unit	K_x=K_y (m/d)	S_s (m^{-1})
L1 (phreatic)	0.4	0.01 - 0.2
L2 & L4 (aquitards)	$5 \cdot 10^{-2}$	$5 \cdot 10^{-6}$ - $2 \cdot 10^{-2}$
L3 & L5 (aquifers)	0.07 - 657	10^{-4}

4.5 Discussion

The study presented in this chapter employs an iterative strategy to characterize the highly heterogeneous specific storage in the Gediz River Basin taking advantage of InSAR datasets. The heterogeneous distribution is suggested by the occurrence of the largest displacements in the central portion of the basin where the hydraulic head decline is small. Conversely, ΔH is significant in the northeastern where the measured displacements are negligible. Given the tabular setting of the hydrogeological system, with the stratigraphic units characterized by limited variability in terms of thickness, a significant variability of the specific storage is necessary.

The use of the 1D consolidation equation facilitates the derivation of a set of S_{sc} at the radar scatterers, enabling the estimation of spatial correlations within the study domain. Subsequently, the Kriging predictor generates a reasonable distribution of S_{sc} and characterizes variance based on their correlations. Table 4.2 lists the hydraulic properties for each unit of the aquifer system as obtained by the calibration procedure.

While this approach is simple and straightforward, it relies on three assumptions:

1. the aquifer deformation can be described by a linear constitutive law;
2. the main compaction occurs in the confined system, specifically in the aquitards, with a minimal contribution from the phreatic layer;
3. the variation of porosity due to aquifer system deformation is negligible.

On the other hand, the small horizontal displacements computed by the 3D GM model support the use of 1D Terzaghi's equation (Eq. 4.1) to quantify the specific storage.

Furthermore, the integration of geological information, InSAR observations, and groundwater (GW) solutions is crucial for implementing the 1D

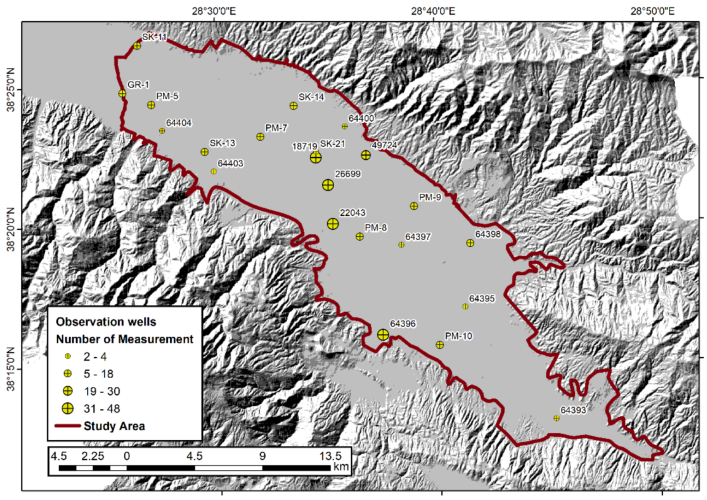

Figure 4.13: Locations of monitoring wells and number of measurement records available for each well in the study area. After Elçi et al. [2022].

consolidation equation. The thickness of stratigraphic units is derived from 118 boreholes distributed in the valley, ranging from 10 to 100 m depth. In terms of InSAR observations, the stability threshold is estimated to be around $\pm$ 0.9 cm/yr based on the noise standard deviation [Bru et al., 2021].

In comparison to these two sources, the change in hydraulic head (ΔH) as derived from GW modeling is considered less reliable. Many piezometric records have limited temporal coverage, with only a few extending to the period monitored by InSAR, which makes it challenging to capture ΔH during this time (Figures 4.13 and 4.14). Due to the limited availability of piezometric records, the GW model yields large drawdown in northwest zone, where InSAR indicates small subsidence, leading to a extremely small S_{sc}. Whereas InSAR suggests significant subsidence in the areas where the GW solution provides negligible ΔH, resulting in extremely large S_{sc}. Consequently, the range of S_{sc} varies over three orders of magnitude which is unusual for alluvial aquifer systems [Teatini et al., 2006b, Ye et al., 2016, Faunt et al., 2016].

On the other side, the uncertainty of S_{sc} is introduced to the calibration of hydraulic conductivity in the GW model, iterations may exaggerate biases. A large S_{sc} implies a significant storage capacity, resulting in a smaller decline in the hydraulic head under the same pumping condition and consequently yielding a greater S_{sc} as per Eq. 4.1. To mitigate this issue, the performance

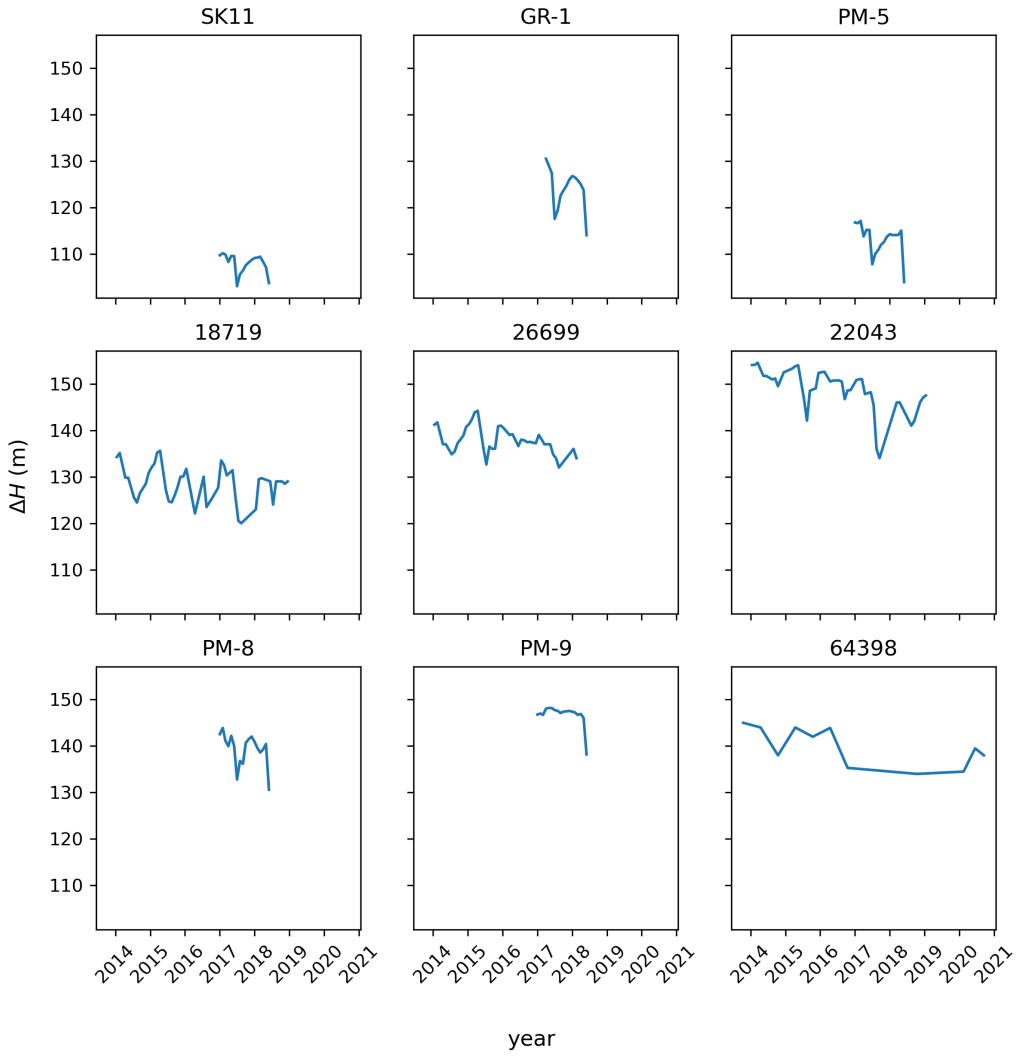

Figure 4.14: Time series of representative monitoring wells in different regions. The wells in the first row are selected in the northwest basin where InSAR presents subsidence rate less than 1 cm/yr and the GW solution suggests the largest ΔH. The opposite for the last four wells. Notice that all wells record similar ΔH

of the GW model must be continuously validated against piezometric records to ensure accuracy for subsequent procedures.

In summary, the proposed approach leverages the extensive coverage of InSAR measurements to effectively characterize heterogeneous specific storage on a basin scale. However, certain assumptions restrict its applicability, and the variance analysis quantifies uncertainties arising the from GW model and InSAR observations in the form of observation noises. Continuous improvement through additional information is advocated to enhance the reliability of the outcomes.

Chapter 5

Uncertainty Quantification in Discontinuous Geomechanical Modeling

This chapter focuses on a systematic investigation of the discontinuous mechanical behaviors observed in over-exploited aquifers, namely earth fissures. From a mathematical perspective, an earth fissure can be represented as a dual-interface configuration within a continuous medium, governed by the Mohr-Coulomb failure criterion. The analyses are carried out using a three-dimensional geomechanical and earth fissure model (geomechanical-earth fissure model, see Sections 2.1.2 and 2.1.3), designed to incorporate such discontinuities into continuous finite element discretization of an aquifer system.

The geomechanical-earth fissure model model is initially applied, in the framework of a deterministic approach, to replicate the evolution and geometric features of three earth fissures occurred in Guangming, China. Then, the modelling analysis progresses with a stochastic analysis aimed at examining the influence exerted by various hydrogeologic parameters on the behavior of these aseismic geological features. This investigation employs three methodologies for global sensitivity analysis, which are the conventional sampling-based Sobol' sensitivity analysis, along with polynomial chaos expansion (PCE), and gradient boost tree

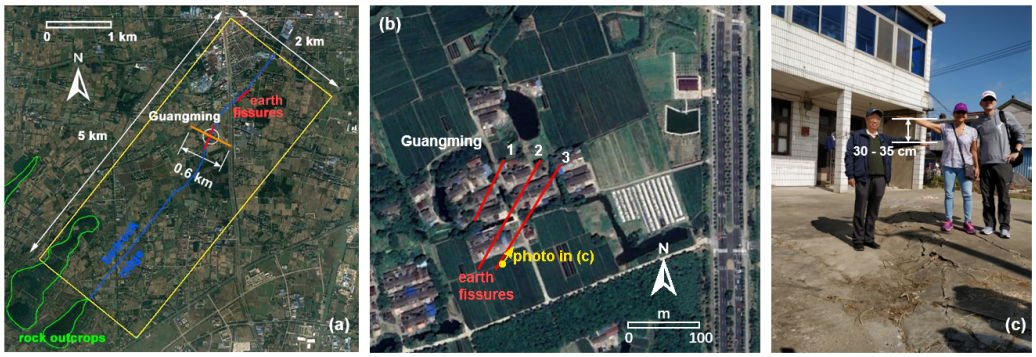

Figure 5.1: (a) Landsat image of the Wuxi area around Guangming with the hills outcropping in the Yangtze plain ≈3 km to the southwest of the village. The yellow box represents the trace of the model domain simulated by Ye et al. [2018], the 600 m long orange alignment orthogonal to the buried ridge the domain of the 2D geomechanical model-earth fissure model developed in this thesis work. (b) Sketch of the three earth fissures crossing the Guangming village. (c) Photo at fissure 3 with people highlighting a slip of about 30-35 cm between the two sides of the fissure. After Li et al. [2021].

(GBT) algorithms.

The concluding section critically compares these analytical methodologies, outlining their respective strengths and weaknesses. The objective is to provide clarity on their utility in enhancing our understanding of earth fissure behavior and to inform future research directions in this field.

The content of the chapter is based on the publications by Li et al. [2021] and Li et al. [2022].

5.1 Earth Fissures in Guangming, China

The study area is situated in the Yangtze River delta (Figure 5.1(a)), where multiple earth fissures formed over the past decades [Ye et al., 2015]. The extensive groundwater extraction in the region, referred to Su-Xi-Chang (SXC), caused marked land subsidence up to 2.5 m in 2013. The intensity of the groundwater withdrawals can be divided into three stages: *i*) a gentle exploitation stage (1970-1990), *ii*) an accelerated stage (1990-2000), and *iii*)

a recovery phase due to wells shutdown imposed by the government (since 2000).

Unlike the other two case studies presented in the previous chapters, this region is seismically inactive. Notably, the emergence of fissuring coincided with the period of intensified groundwater extraction over the 1990s. This temporal correlation suggests that the formation of fissures is a direct consequence of the severe anthropogenic land subsidence induced by excessive pumping of groundwater.

Since regulations prohibiting further withdrawal were implemented in the year 2000, there has been no increase in the number of fissures within the SXC area, with stabilization at a total count of twenty-five. While most of them have stopped growing, the multi-fissure system at Guangming village remains active. The first rupture was discovered in 1998 and was followed by two additional fissures extending over 150 meters each. These fissures crossed the village and caused damages to the buildings (Figure 5.1(b)).

Previous investigations [Ye et al., 2018] suggested that these fissures are associated with an underlying bedrock ridge given their southwest-northeast orientation parallel to the buried rocky ridge. However, the fissures at Guangming are not generally evident at the land surface due to the continuous remediation activity of the farmers living in the village. Cracks in the houses and the nearby pavement allow for quantifying in 20-30 cm the sliding of one of the external fissures (Figure 5.1(c)).

5.1.1 The Geomechanical-Earth Fissure Model Setup

The first 3D geomechanical-earth fissure model model of the area was developed by Ye et al. [2018]. This thesis has elected to develop a plane strain stress analysis by simulating the mechanical behavior on a vertical section orthogonal to the bedrock ridge and the fissure alignments. This simplifying hypothesis is fully warranted by the outcome of the previous 3D model and allows us to refine the mesh around the ridge to reproduce in more detail the dynamics of the multi-fissure development. The hydrogeological setting and piezometric evolution in space and time are obtained from this previous research by Ye et al. [2018].

The model domain extends 600 m and 165 m along the x-horizontal and z-vertical direction, respectively (Figure 5.2). A 50-m thickness is assumed along the y-direction. Based on the borehole lithostratigraphies provided by

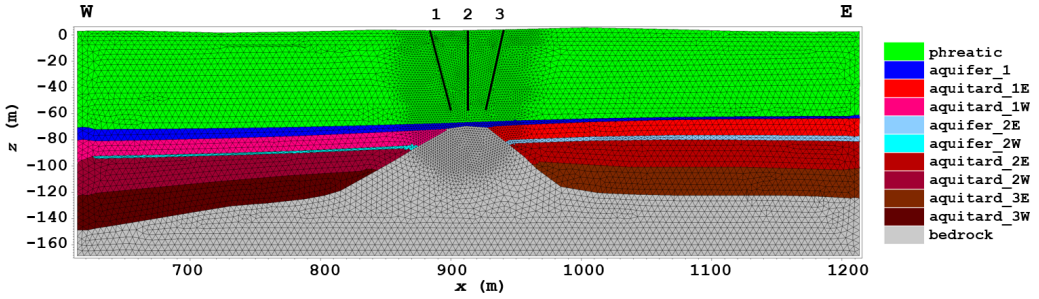

Figure 5.2: FE-IE mesh used for the geomechanical-earth fissure model application at Guangming. The colors are representative of the various hydrogeologic units. The upper "phreatic" aquifer sums up the upper layers where the piezometric level did not change significantly. The black lines above the bedrock ridge represent the IEs alignments. After Li et al. [2021].

Jiangsu Geological Survey, the groundwater system can be divided into an upper unconfined aquifer and a confined aquifer system, the latter composed of first shallower and second deeper aquifers separated by clayey aquitards. The groundwater was mainly withdrawn from the second confined aquifer whose average depth is 80 m.

The bedrock ridge is in the middle of the simulated domain, with the ridge tip about 70 m deep below the ground surface. The ridge intercepts the second confined aquifer and the adjacent aquitards and cuts them into two portions hydraulically disconnected (Figure 5.2).

The IE alignments inserted within the FE mesh to simulate the possible multi-fissure development are shown in Figure 5.2. Earth fissures are numbered from #1 to #3 from west to east. Fissure locations are known at the land surface only (Figure 5.1(a)). Therefore, the traces are extended underground following the suggestion obtained through a simplified model developed in Li et al. [2021].

The FE mesh consists of 52,236 nodes and 253,830 tetrahedra with a characteristic dimension ranging from 2 m around the bedrock ridge to 5 m at the boundaries. Each potential fissure is represented through 198 IEs with characteristic length in the x-z plane equal to about 2 m (Figure 5.2).

The simulation spans 20 years, from 1980 to 2000, with 20 equal time steps. The piezometric variation is uniformly distributed within each layer according to the results by Ye et al. [2018]. The behavior versus time is shown in Figure 5.3. Due to the bedrock ridge, the piezometric drawdown

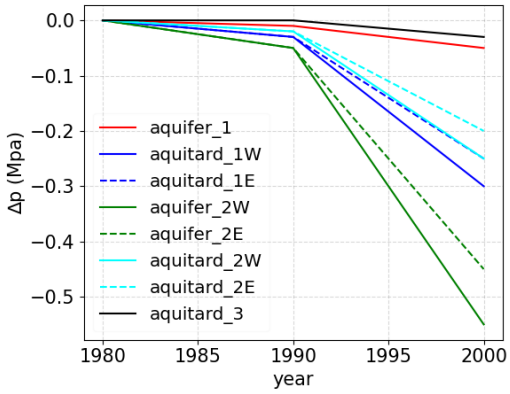

Figure 5.3: Pore pressure changes in the aquifer system at Guangming from 1980 to 2000. The temporal evolution can be divided into two phases, i.e. before 1990 and after 2000, with a linear behavior in each phase. The trends are obtained by simplifying the outcome of a groundwater flow model by Ye et al. [2018]. After Li et al. [2021].

within the deeper units was slightly greater on the west side than on the east side. Following Ye et al. [2018], all the aquifers are assumed to be elastic, with the parameter values summarized in Table 5.1.

The following boundary conditions are applied: horizontal displacements along the lateral boundaries are restricted to the component parallel to the surface, the top plane is a traction-free surface, and zero displacements are prescribed on the bottom. The maximum (absolute value) σ_1 and minimum (absolute value) σ_3 principal stresses coincide with the vertical $\hat{\sigma}_v$ and horizontal $\hat{\sigma}_h$ stress, respectively. The vertical total stress σ_v increases linearly with depth in agreement with a soil bulk density set at 2,000 kg/m^3. The initial $\hat{\sigma}_v$ distribution is set as the initial pre-consolidation stress $\hat{\sigma}_{v,pre}$. Additionally, the ratio between $\hat{\sigma}_h$ and $\hat{\sigma}_v$ is fixed at $\nu/(1-\nu)$, with $\nu = 0.25$. Cohesion c and friction angle φ are set equal to 0.01 MPa and 30°, respectively.

5.1.2 Numerical Outcomes

Figure 5.4 shows the displacement and stress fields of the aquifer system in 1991, immediately prior to the initiation of fissuring. The presence of the ridge reduces the thickness of the compressible units, causing the vertical

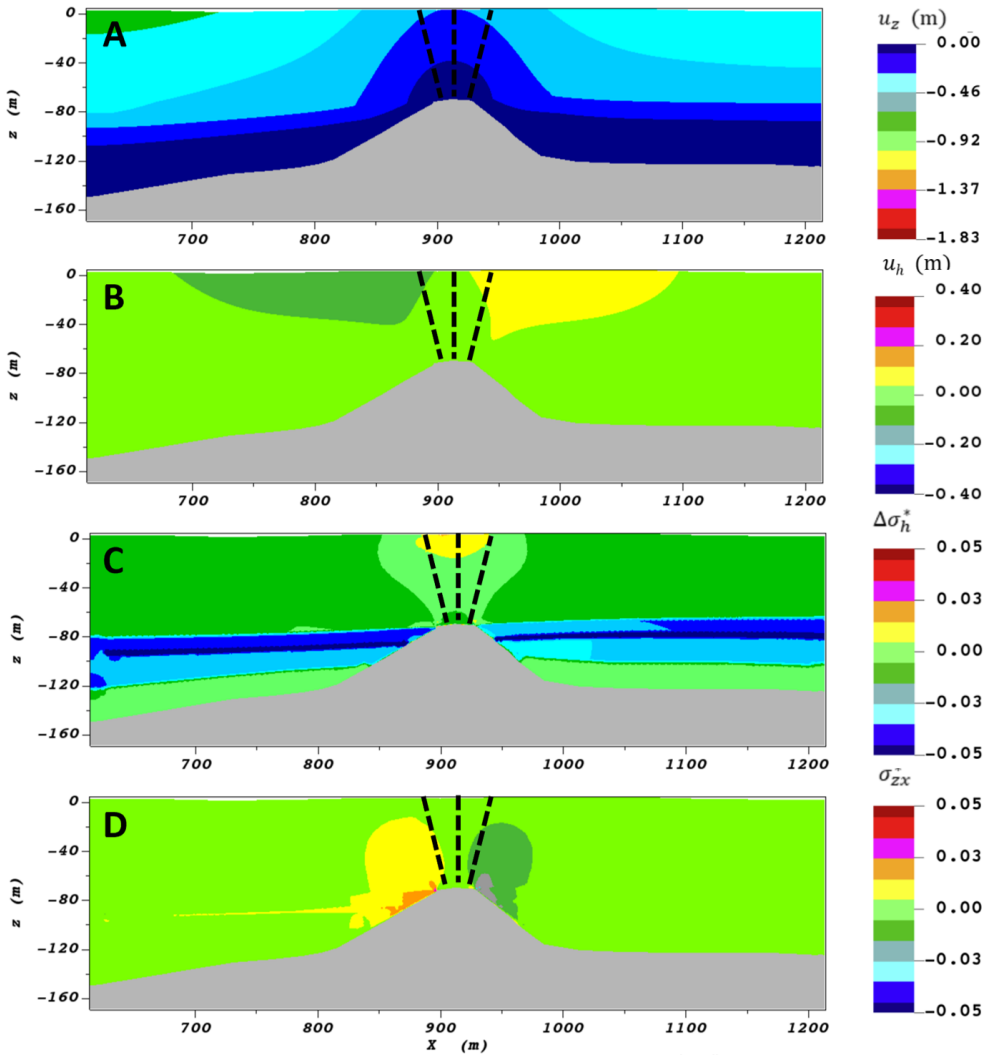

Figure 5.4: Outcomes of the geomechanical model (GM) model in 1991. (a) Vertical and (b) horizontal displacements u_z and u_x, respectively; (c) dimensionless horizontal stress variation with respect to the initial values $\Delta\sigma_h^* = \Delta\sigma_x/\Delta p$; and (d) dimensionless shear stress $\sigma_{zx}^* = \sigma_{zx}/\Delta p$.

Table 5.1: Uniaxial vertical compressibility and Poisson's ratio of the lithological units characterizing the simulated Guangming subsurface. The values were derived from Shi et al. [2007] and Zhang et al. [2016].

Units	c_m (MPa^{-1})
bedrock	$1.0 \cdot 10^{-6}$
aquifers	$2.5 \cdot 10^{-2}$
aquitards	$1.25 \cdot 10^{-1}$

movements u_z to be highly variable, being proportional to the thickness of aquifers (Figure 5.4A). Above the slope of the ridge u_z displacements are accompanied by significant horizontal movements u_x with direction away from the ridge tip, above which u_x=0 (Figure 5.4B). Correspondingly, Figure 5.4C shows the development of tensional horizontal stress above the ridge as a result of stretching. In contrast, most of the aquifer system experiences an increase in compressive horizontal stresses, as indicated by negative values stemming from compaction. In this peculiar geologic setting, the pore pressure depletion leads to the development of significant shear stress, primarily within the portions of the aquifers in contact with the ridge flanks, and extending upwards (Figure 5.4D). The magnitude of shear stress is correlated with the gradient of the vertical displacements. Therefore, shear stress remains negligible within the central area of the aquifer system above the ridge tip.

The development and increase of tensile and shear stress above the bedrock ridge have been responsible for the fissure formation. Figure 5.5 shows the results of the geomechanical-earth fissure model model in 2000, at the end of the simulation. The model reproduces the formation of all three earth fissures as observed at Guangming.

Compared to 1991, the maximum subsidence values on the west and east sides of the ridge increase to 1.9 m and 1.8 m (Figure 5.5A), respectively, consistent with the findings by Ye et al. [2018]. The maximum horizontal displacements on the land surface increase to 0.4 m (Figure 5.5B). Notice the presence of evident jumps in u_z and u_h across the IE alignments, indicating the occurrence of significant fissuring. The variation of the horizontal stress is characterized by a pattern more complex than in 1991 (Figure 5.5C). Negative values (i.e., compression) still characterize most of the area, while the central area above the ridge tip near the interfaces undergoes tensile stress.

However, it is important to note that $\Delta\sigma_h^*$ vanishes within the shallowest portion of the soil above the tip of the ridge where the central earth fissure opens. Consequently, the maximum tensile stress moves downwards to the bottom of the fissure. Generally, shear stress σ_{zx}^* significantly increases too (Figure 5.5D). The largest values concentrate around the ridge slopes, with a more complex pattern accounting for the different pressure changes, the geomechanical properties of the various hydrogeologic units, and the fissure development. At shallow depth, σ_{zx}^* is nearly zero above the ridge tip because of the quasi-symmetric setting and it concentrates along the two lateral earth fissures indicating a certain sliding.

The stress distributions highlight the predominant effect exerted by the ridge. The undulating shape of the ridge causes differential subsidence, which in turn leads to high-magnitude stresses accumulated directly above the ridge tip or along the bedrock sides. Specifically, the middle interface above the ridge tip is always impacted by the tensile stress as the differential subsidence goes.

By contrast, the same interface initially is free of shear stress which indicates that tensile stress prevails on the initiation of fissure #2. By the same reasoning, fissures #1 and #3 are mainly activated by shear stress. Despite some stress variations during the development of fissures, every interface is controlled by the same type of stress since the beginning. Furthermore, because the tensile and shear strength of soils are low, the potential for earth fissures to form above and around the ridge is high.

The model outcomes on the IEs allow us to comprehensively reproduce the evolution of the fissure characteristics over time (Figures 5.6 and 5.7).

Figure 5.6 shows the earth fissure characteristics in 2000 as computed by the geomechanical-earth fissure model model. Given the marked tensile stress and minimal shear stress, the middle fissure (fissure #2) mainly opens (about 60 cm at the land surface) and slides negligibly (tensile rupture), with an activation depth of approximately 17 m. Conversely, sliding characterizes the two side fissures (fissures #1 and #3) with maximum values approximately equal to 55 cm and 40 cm, respectively (shear rupture). This latter value is quite consistent with the estimated field value (Figure 5.1(c)). Their activation depth amounts to about 40 and 50 m, respectively. Notice that opening is null on fissure #1 and amounts to a few cm only on fissure #3. Here, the opening depth is much smaller (a few meters only) than the sliding depth, meaning that the condition in Eq. 2.18 with $t_N = 0$ develops

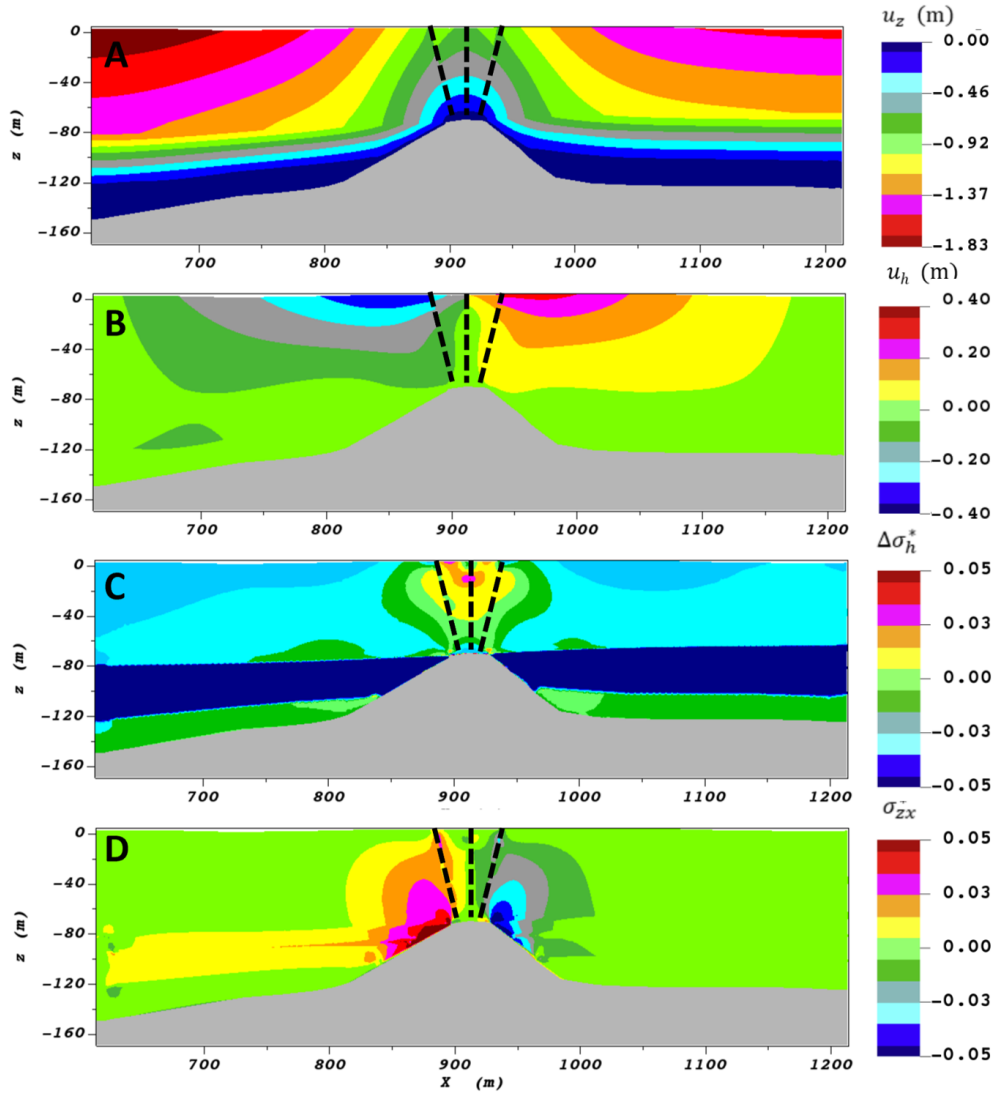

Figure 5.5: Outcomes of geomechanical model (GM) model in 2000. (a) Vertical and (b) horizontal displacements u_z and u_x, respectively; (c) dimensionless horizontal stress variation with respect to the initial values $\Delta\sigma_h^* = \Delta\sigma_x/\Delta p$; and (d) dimensionless shear stress $\sigma_{zx}^* = \sigma_{zx}/\Delta p$. After Li et al. [2021].

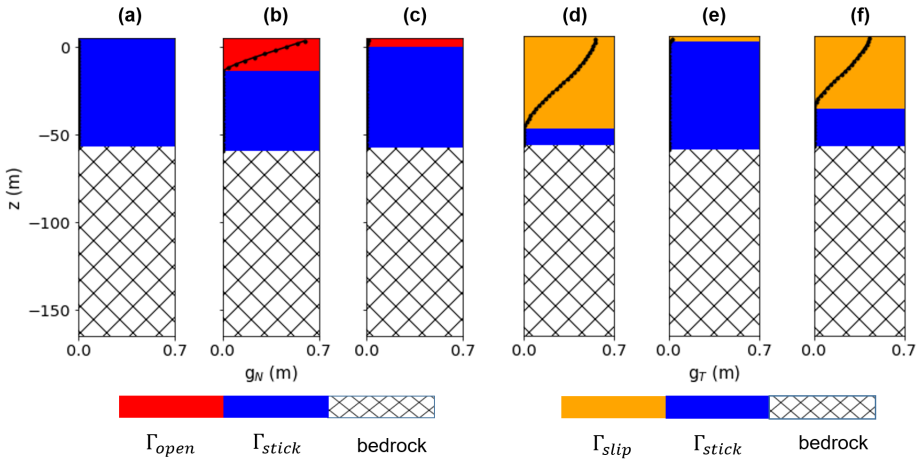

Figure 5.6: Outcomes of geomechanical-earth fissure model model on the IEs. Opening g_N (dotted black line), opening Γ_{open}, and closing Γ_{stick} areas (red and blue zones) at 2000 as obtained for fissure 1, fissure 2, and fissure 3 (see Figure 5.2 for the fissure location). Similar plots are shown for the slip g_T, sliding Γ_{slip}, and close Γ_{stick} areas (orange and blue zones) at the same time. After Li et al. [2021].

close to the land surface only and $f = 0$ (Eq. 2.17) on a larger depth interval. Interestingly, the sliding of fissure #2 is characterized by a certain increase in the shallowest depth range corresponding to the opening depth of fissure #3.

Finally, Figures 5.7(a) and 5.7(b) show the behavior vs time of maximum opening and sliding and activation depth d_{act}, respectively. It is interesting to note how the side fissures activate earlier than fissure #2, i.e. 1991 versus 1992. The earth fissures originate at the land surface and propagate downward with time. Fissure #3 started opening in 1995, a few years later than sliding.

5.1.3 Discussion

The employed geomechanical-earth fissure model model successfully simulates the formation and propagation of multi-fissures in a subsiding basin characterized by a shallow buried ridge. The modeling outcomes demonstrate that tensile and shear stresses accumulate in the sedimentary system above the ridge tip and slopes, respectively, following pressure depletion.

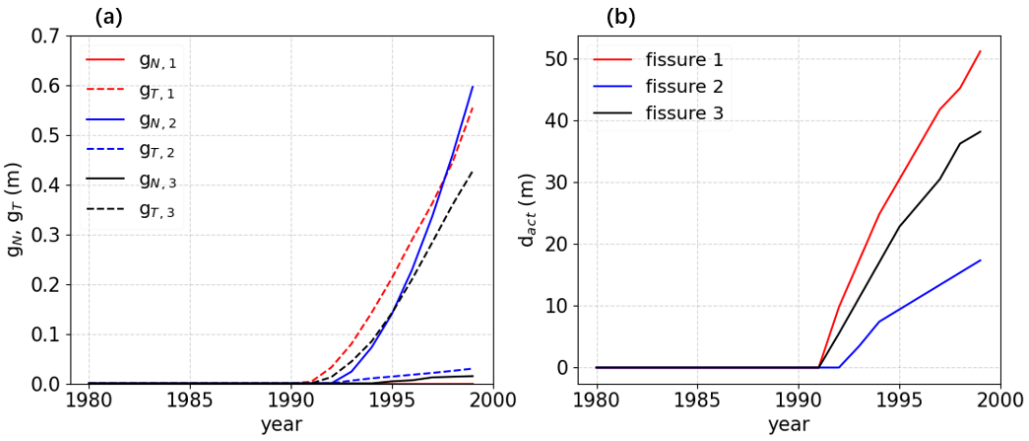

Figure 5.7: Outcomes of the geomechanical-earth fissure model model at Guangming. Behavior vs time of (a) maximum opening g_N and sliding g_T and (b) activation depth d_{act} for the three earth fissures. After Li et al. [2021].

Furthermore, it reveals how fissures form with tensile stress leading to opening (bending condition) and shear stress to sliding (shear condition).

Theoretical investigations developed in the previous decades support our outcome at least in part, although they reported only qualitative stress analyses and generally did not address specifically the possibility of multi-fissure occurrence. Budhu and Shelke [2008] confirmed the importance of shear stress in fissure formation and pointed out that coupling of bending and shearing is the most efficient mechanism causing significant fissures: firstly, a tensile crack forms at ground surface providing a weakness plane for shearing to propagate the discontinuity downwards. Burbey [2010] reported that the presence of the bedrock boundary imposes horizontal deformations greater near the land surface than at the bottom of the aquifer yielding a rotation of the sedimentary block toward the pumping well. Moreover, a large accumulation of vertical shear strain can easily contribute to the formation of earth fissures.

The formation of multi-fissures is mentioned in Budhu [2011]. He suggested that the onset of multiple earth fissures can depend on shearing exclusively and that

field observations in Arizona do indicate preferential earth fissure development near exposed or shallow bedrock ridges or near the margins of

alluvial basins or at preexisting fault boundaries. When one of these conditions exists, only a single earth fissure is likely to form because further energy from simple shear deformation and rotation will be dissipated by its (earth fissure) movement suppressing other earth fissures from forming. When such boundary conditions do not exist, multiple parallel earth fissures could develop simultaneously or progressively. This is not the case for the examples simulated in this work, where we are able to simulate multi-fissure development above shallow ridges.

A more in-depth understanding of the mechanisms causing and controlling earth fissures can be obtained from Figure 5.8. Here, using as reference the geological setting and pressure history in Guangming, the model results at 2000 in terms of displacement field above the ridge is compared for 3 different scenarios: *i*) the "continuous setting", i.e. the solution provided by the GM model (Figure 5.8(a)); *ii*) the "earth fissure setting", i.e. the geomechanical-earth fissure model solution with the IEs activated based on Coulomb criterion (Figure 5.8(b)); and *iii*) the "cut setting", i.e. a GM-IE solution obtained with friction-less IEs that corresponds to the GM solution with inner boundaries placed along the IEs alignments (Figure 5.8(c)). This latter is a nonphysical scenario, representing the other extreme of the possible range of fissure parameters with respect to the "continuous setting". It helps understand better what occurs in the most realistic "earth fissure setting". The displacement field is represented by deforming the mesh geometry with respect to the initial setup. The main features of the displacement and stress fields are sketched in the panels to the right, i.e. Figure 5.8(d), Figure 5.8(e), and Figure 5.8(f), respectively.

The differences between the three scenarios are significant: if with the continuous setting and

cut setting the portion above the ridge moves downward less than the side parts because of the larger aquifer compaction occurring far from the ridge, an opposite condition develops for the

earth fissure setting. This behavior, which is rather counterintuitive, can be understood by looking at the stress field that develops around the ridge. Shear stress accumulation causes a rotation of the fissure #1 and #3 planes toward the foot-wall (i.e. counterclockwise for fissure #1 and clockwise for fissure #3), causing the hanging wall to slide downward with respect to the foot-wall. Notice the different values of u_x and u_z at the two sides of the earth fissure that develop in this setting (Figure 5.8(e)): horizontal displacements

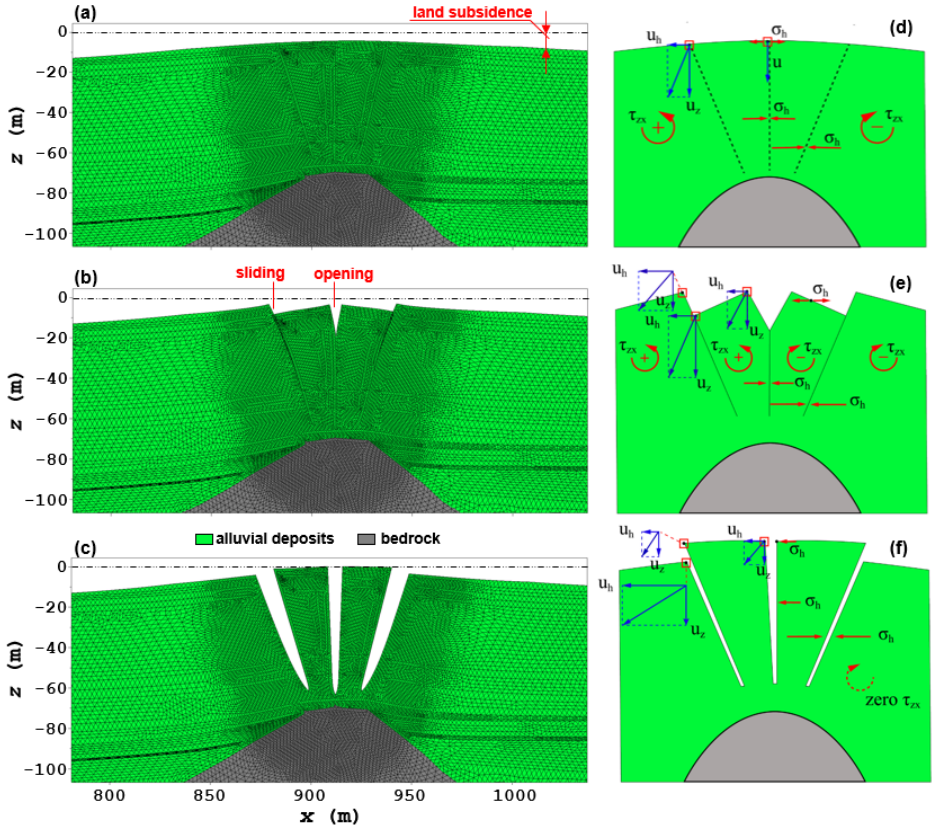

Figure 5.8: Guangming case study: comparison between the model solution in terms of deformed mesh at 2000 with (a) the "continuous setting" as obtained by the GM simulator, (b) the "earth fissure setting" as obtained by geomechanical-earth fissure model simulator, and (c) the "cut setting" as computed by the GM model once discontinuity surfaces are added along the IE alignments of model (b). The displacement exaggeration is 10. We highlight land subsidence obtained on the FEs, opening and sliding obtained on the IEs. (d-f) Sketches representing the correspondent distribution of most significant displacements (in blue) and stresses (in red). After Li et al. [2021].

largely prevail on vertical movements on the foot-wall, the opposite on the hanging wall.

A similar rotation was already highlighted by Hernandez-Marin and Burbey [2012] in the case of a fault zone fully intercepting an aquifer system. The larger downward movement of the hanging wall relative to the foot-wall is confirmed by direct observations, see the photo in Figure 5.1(c). It is also to point out that any significant shear stress develops around the tip and the cracks for the "cut setting".

A final remark is worth to be done in relation to the grid requirements needed to accurately simulate the multi-fissure development. In the recent study by Ye et al. [2018], a similar modeling approach was applied to reproduce a single fissure evolution at Guangming village. Ye et al. [2018] highlighted the need to use a two-scale modeling approach to simulate the generation and development of earth fissures caused by extensive aquifer exploitation in real 3D geological settings. The approach is based on the sequential use of regional groundwater and classical geomechanical models, followed by a local groundwater flow model and an advanced geomechanical-earth fissure model simulator. The local model was characterized by element size ranging between 35 and 150 m in the horizontal direction and from 3 to 5 m in the vertical direction. Modeling multi-fissure occurrence needs to downscale even more the mesh resolution in the horizontal direction, with elements characterized by a few meters in size along all the directions.

A robust calibration and validation of these models is a step that is not possible yet. With the exception of the fissure length and, in a few cases, estimates of sliding and opening [Li et al., 2021], measurements are quite scarce and generally started after the fissure already developed. In Guangming, for example, the Geological Survey of Jiangsu Province established piezometers, extensometer groups, fiber optics, and leveling lines in 2009 only, when the majority of the fissure development already occurred.

On the other hand, the previous case studies have highlighted the powerful strength of SAR-based interferometry techniques on long-term deformation acquisitions over a large scale. Advance applications, combining ascending and descending orbits to retrieve vertical and west-east movements [Miller and Shirzaei, 2015], using Persistent Scatters processing chains on X-band scenes could be quite effective in deriving accurate space and time distribution of the differential land displacements that develop around multi-fissure areas.

5.2 Sensitivity Analyses on Factors Controlling Earth Fissures

Section 5.1 delves into the dynamics of multi-fissure within a subsiding aquifer system intersected by a buried bedrock ridge, focusing on the case study in Guangming. The analysis of displacement and stress fields highlights the significant influence of the ridge on fissure formation. However, the deterministic approach employed in the modeling application does not allow for quantifying how fissure occurrences are linked to the ridge geometry. Moreover, as a case study, it fails to account for complexities introduced by other factors such as changes in pore pressure and variability in aquifer properties and thickness.

This section is aimed at overcoming these deficiencies. A simplified case study is constructed featuring an impermeable and incompressible rock ridge situated within a subsiding basin. Stress and displacement analyses are conducted alongside evaluations of fissure states utilizing the same geomechanical-earth fissure model model adopted for Guangming. To ascertain the relative influence of various parameters on fissure propagation, three distinct methodologies for global sensitivity analysis are employed. The first method involves conventional sampling-based Sobol' sensitivity analysis which is then juxtaposed with two surrogate-based approaches: one employing general polynomial chaos expansion (PCE) based Sobol' analysis and another utilizing feature importance evaluation via a gradient boosting tree (GBT) model. These methods serve to quantify the degree to which the fissure aperture responds to different contributing factors within the modeled system.

5.2.1 Model Setup and Parameterization

The investigated configuration conceptualizes the geological setting in Guangming Village, representing an aquifer system featuring an undulating bedrock. The numerical simulation is developed on a quasi-3D domain 2,000 m long (x-direction), 50 m thick (y-direction), and 500 m deep (z-direction) (Figure 5.9). Identically to the Guangming investigation, a traction-free top surface and a fixed bottom surface are considered. On the lateral surfaces, the horizontal displacements are precluded in the orthogonal direction.

The conceptual model is composed of three hydrostratigraphic units: an

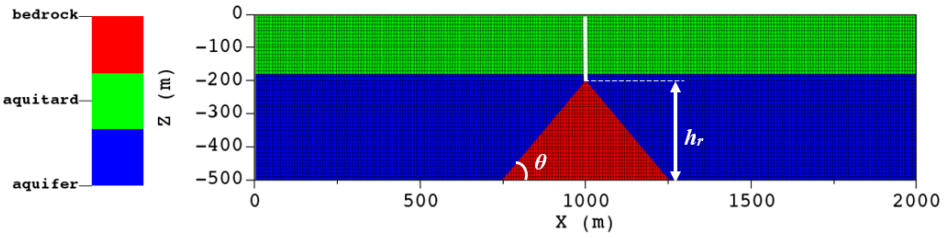

Figure 5.9: FE grid of one numerical experiment in sensitivity analysis, where $\tan\theta = 1.2$, $\zeta = 0.65$. The three colors (red, green and blue) represent the hydrogeologic units. h_r represents bedrock ridge height which is the function of θ. The IE alignment is highlighted by a white line whose length is equal to $500 - h_r$. After Li et al. [2022].

upper aquitard, a bottom aquifer, and a buried triangular bedrock. For the sake of simplicity, each material is assumed to behave elastically with the same Poisson ratio $\nu = 0.25$. Cohesion c and friction angle φ are set equal to 0.01 MPa and 30° respectively. A piezometric drop linearly varies from 0 to Δp in 10 years and is uniformly assigned to the bottom aquifer, meanwhile, the upper aquitard is regarded as a hydraulically "inactive" unit where the pore pressure propagation from the underlying sandy layer is negligible.

The initial stress field is computed based on the gradient density ($\sigma_v = 1200$ kg/m^2/m) and the minimum-to-maximum stress ratio reads $\hat{\sigma}_h/\hat{\sigma}_v = \nu/(1-\nu)$. The vertical size of tetrahedral FE elements is 10 m and the horizontal dimension is in the range between 5.5 and 20 m, slightly varying according to the ridge geometry (Figure 5.9).

The multi-fissure analysis developed by Li et al. [2021] highlighted that, regardless of the slope θ of the ridge, an earth fissure always opens above the ridge tip, where a stress state characterized by high tension develops. However, the areas affected by large shear stress and susceptible to the formation of shear fissures depend on θ. Addressing these changes in a global sensitivity analysis investigation would require continuous repositioning of the IEs within the FE mesh, leading to significant model complexity. Therefore, shear fissures are not addressed in the model investigation presented in the following.

In principle, fissures cannot propagate within the bedrock where pressure does not change and the stress field variation is negligible. Therefore, an IE alignment is vertically introduced from the land surface to the ridge tip as

Table 5.2: Range of the input features for global sensitivity analysis: the four random variables $\tan\theta$, ζ, c_m, and Δp are uniformly distributed.

Feature	Min	Max
$\tan\theta$	5.0e-1	1.9e-0
ζ	4.0e-1	9.0e-1
c_m (MPa^{-1})	5.0e-3	5.0e-2
Δp (MPa)	-1.0e-0	0.0e-0

highlighted by the white line in Figure 5.9. The triangular IE discretization is consistent with FE discretization. Stress distribution and magnitude depend on the ridge geometry, the aquifer thickness, and differential subsidence. This latter is primarily dependent on the pore pressure change and sediment compressibility. Therefore, these four variables, i.e. ridge geometry, aquifer thickness, pressure change and sediment compressibility, are selected as input features for global sensitivity analysis.

Here, the ridge geometry is characterized by the slope of the bedrock ridge ($\tan\theta$). Note that the length of the ridge basement is fixed at 500 m. The fraction of the aquifer thickness over the domain thickness (500 m) is denoted ζ. The selected ranges for $\tan\theta$ and ζ are determined by the domain dimensions and discretization. The ranges for the aquifer compressibility (c_m) and the maximum piezometric decline (Δp) are based on available literature data on exploited aquifer systems [Burbey, 2002, Conway, 2016, Ochoa-González et al., 2018, Ye et al., 2018, Zhu et al., 2020]. The piezometric decline reaches the maximum value with a linear behavior in 10 years. The variability ranges of the parameters used in this study are summarized in Table 5.2. A uniform probability distribution is assumed for each variable.

5.2.2 Deterministic Model Run

One experiment designed for global sensitivity analysis is randomly selected to present the numerical outcomes. The simulated temporal evolution of tensile stress on a vertical section of the domain is shown in Figure 5.10. Tensile stress σ_h initially accumulates around the ridge tip. As the piezometric level declines, a tensile zone also occurs at the land surface above the apex of the ridge. Once tensile stress exceeds the tensile strength, i.e.

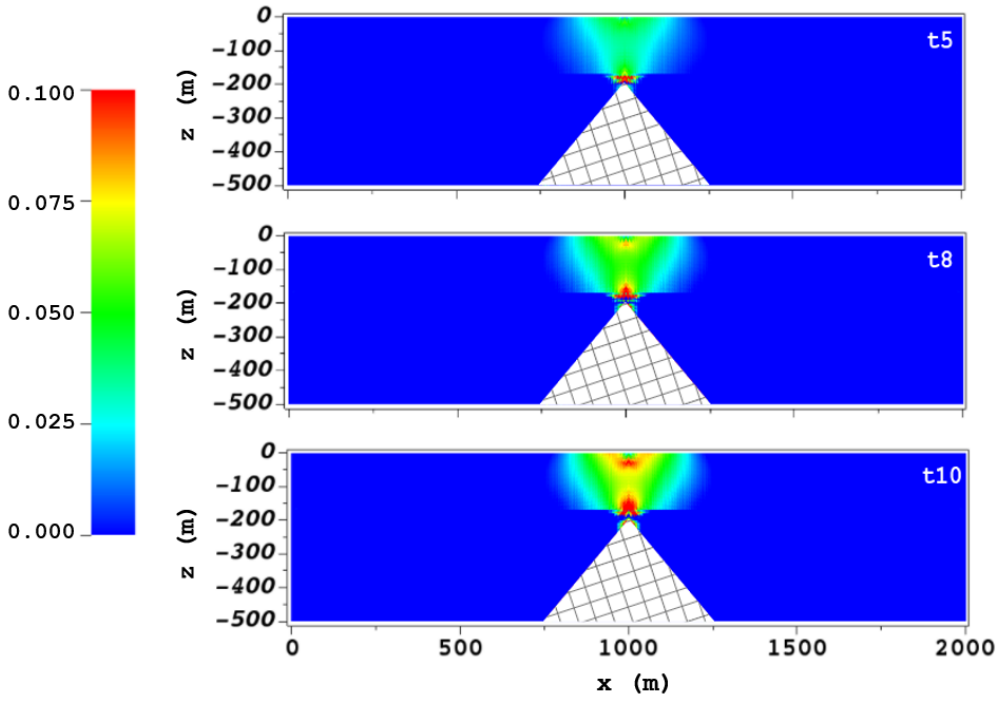

Figure 5.10: Sequential evolution of the dimensionless horizontal stress $\sigma_h^* = \sigma_h/\Delta p$ at the 5th, 8th and 10th years as simulated with the geomechanical-earth fissure model model. The results are obtained using $\tan\theta = 1.2$, $\zeta = 0.65$, $c_m = 0.05$ MPa^{-1} and $\Delta p = -0.89$ MPa. After Li et al. [2022].

$t_N = 0$ (see Section 2.1.3), IEs change from a stick to an open state with the discontinuity that develops at the land surface and propagates downwards. Simultaneously, tensile stress dissipates due to the fissure opening. Notice that the porous medium directly above the ridge tip does not experience any shear stress due to the symmetric configuration. Therefore, only fissure opening develops with this setting.

Figure 5.11 shows the evolution of the earth fissure as provided by the IEs. Fissure initially originates at the land surface where the tensile strength is the lowest and later develops at depth too, just above the ridge tip, in response to the concentration of tensile stress. The upper portion of the fissure, which initially is very narrow, keeps enlarging horizontally and extending downwards as the aquifer pressure continues to decrease. At the 10th year, corresponding to a piezometric decline in the confined aquifer equal to 1 MPa, the fissure reaches a depth of about 30 m with a maximum opening of 1.7 m

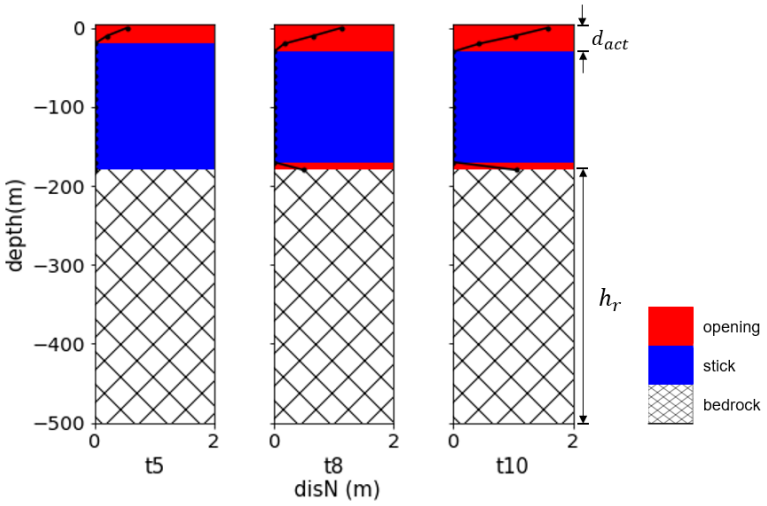

Figure 5.11: Sequential evolution of fissure opening at the 5th, 8th and 10th years: opening g_N (dotted black line), opening Γ_{open} and closing Γ_{stick} areas (red and blue zones) are provided. The results are obtained using $\tan\theta = 1.2$, $\zeta = 0.65$, $c_m = 0.05$ MPa^{-1} and $\Delta p = -0.89$ MPa. After Li et al. [2022].

at the land surface, narrowing with depth. Conversely, the discontinuity bottom remains fixed at the same depth without significant development.

Generally, the energy is dissipated after fissuring mainly at the land surface. Moreover, the overburden stress due to sediment load usually limits tensile fissuring at depth [Budhu and Shelke, 2008]. Therefore, the bottom activated zone is not included in the quantity of interest d_{act} that is defined as the fissure depth from the land surface. It is worth mentioning that the size of activated depth is controlled by the vertical length of the IE alignment, thus the relative activated depth $d_{r,act} = d_{act}/(500 - h_r)$ is introduced to have comparable results when varying the model geometry (Figure 5.9). In this case, $d_{r,act}$ equals 0.132.

5.2.3 Surrogates of the Geomechanical-Earth Fissure Model

PCE surrogate

The computation of the PCE coefficients has been initially carried out by the pseudospectral approach (Eq. 2.41) and increasing step by step the PCE

Table 5.3: Validation of the PCE at increasing value of the maximum total degree of the PCE expansion. The coefficient of determination R^2 is used to assess the goodness of fit. R^2_{PS} refers to PCE coefficients computed using the pseudospectral approach through Gauss quadrature, whereas R^2_{RG} is obtained by regression. The number of points indicated are those used to train the surrogate models. After Li et al. [2022].

PCE degree N	# gauss points	R^2_{PS}	# regression points	R^2_{RG}
2	81	0.64	5600	0.64
3	256	0.69	5600	0.68
4	625	0.72	5600	0.73
5	1296	0.77	5600	0.76
6	2401	0.78	5600	0.78
7	4096	0.79	5600	0.79

degree of the polynomial response. The surrogate model $\mathcal{M}_{\text{PCE}}$ is developed to approximate $d_{r,act}$ with input parameters $\boldsymbol{Z} = \{\tan\theta, \zeta, c_m, \Delta p\}$. The validation of the fitted surrogate model is carried out by employing 7000 samples, that is the available set of points used to compute Sobol' indices with the quasi Monte Carlo approach. Moreover, train and validation of the PCE surrogate is also obtained from the 7000 points using 80% for regression and the remaining 20% for validation.

The results are shown in Table 5.3 with the coefficient of determination R^2 used to assess the fit goodness of the surrogate model to the full problem and computed by means of the leave-one-out (LOO) cross-validation (CV). Increasing the PCE degree of both approaches, i.e. pseudospectral and regression, provides similar results with increasing values of the coefficient of determination R^2. Obviously, the computational cost of regression is much higher, in particular at low PCE degrees. The maximum R^2 is close to 0.80. A visual comparison of the full model results and the surrogate solution is shown in Figure 5.12(a). The higher discrepancy is obtained at the boundary of the solution where the surrogate solution provides results larger than 1.0 or lower than 0.0. These solutions correspond to the nonphysical response meaning (i) a fissure reaches and propagates within bedrock ($d_{r,act} > 1.0$) and (ii) a negative opening ($d_{r,act} < 0.0$), representing non-penetration that is not admitted by the model hypothesis (see Eq. 2.18).

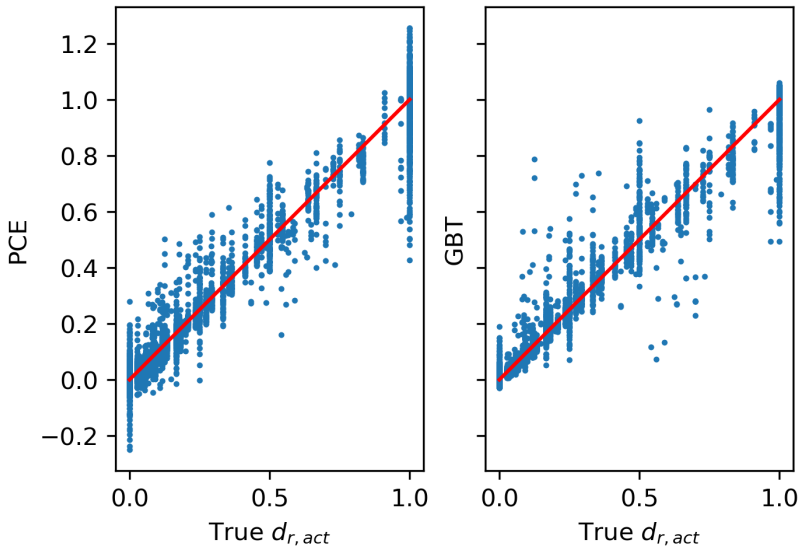

Figure 5.12: Comparison between the full model run and the surrogate solutions. (a) PCE model with regression. Note that $d_{r,act}$ larger than 1.0 representing a fissure that extends within the buried bedrock, and lower than 0 indicating interpenetration of solid bodies are attributed to nonphysical solutions. (b) GBT model, where the predictions are basically within the rational range.

GBT surrogate

Gradient boosting algorithm is also implemented with increasing size of input data to check the convergence, thereof 80% is used to fit model with remaining 20% for validation. Hyperparameter tuning is carried out by a Grid Search method which enumerates all the possible combinations of hyperparameters and gets optimal values based on the corresponding coefficient of determination R^2_{GB}. In this application, only the learning rate ν has been tuned as it is the most important hyperparameter for GBT estimator [Probst et al., 2019].

Table 5.4 shows the model goodness that stabilizes when the data size reaches 5000. In addition to Sobol' samples, the Gauss points (4,096) for the PCE method are also used to validate the regression tree obtained from the maximum sample size (7,000) (Figure 5.12(b)). The regression tree also has some nonphysical predictions ($d_{r,act} > 1.0$), however, the absolute values of discrepancy are much less than that of PCE solutions. Moreover, R^2_{GB}

Table 5.4: Learning rate and validation of GBT at increasing sample size. After Li et al. [2022].

sample size q	learning rate ν	R^2_{GB}
1000	0.23	0.90
2000	0.14	0.94
3000	0.12	0.95
4000	0.16	0.95
5000	0.10	0.96
6000	0.10	0.96
7000	0.10	0.96

Table 5.5: Second-order indices with reference Sobol' method and PCE surrogate model. After Li et al. [2022].

-	S_{12}	S_{13}	S_{14}	S_{23}	S_{24}	S_{34}
Sobol'	0.013	0.033	0.059	-0.005	-0.005	0.010
PCE	0.026	0.020	0.070	0.002	0.017	0.007

suggests GBT algorithm outperforms PCE algorithm with respect to prediction accuracy (R^2_{GB}=0.96 vs R^2_{RG}=0.79). It's crucial to acknowledge that the fissure opening ratio $d_{r,act}$ exhibits high discontinuity, as it remains constant within certain sub-domains (q) regardless of parameter variations. Consequently, both surrogate models fail to capture this characteristic, regardless of the increase in sampling size.

5.2.4 Importance Metrics

Sobol' technique is chosen as the "reference" sensitivity analysis with the input samples generated by the Sobol' sequence. As mentioned in Section 5.2.3, these samples are reused to train and validate PCE and GBT surrogates.

Knowing that the reliability of sensitivity measures obtained by metamodels are dependent on their predictive power, we can ensure PCE and GBT are good surrogates and the "overfitting" problem can be excluded according to the R^2 values obtained from the cross-validation.

Figure 5.13 shows that Sobol' and PCE methods estimate similar results of first-order indices S_i and total Sobol' indices (S_{Ti}), with the PCE algorithm showing a quicker convergence with respect to the quasi Monte Carlo

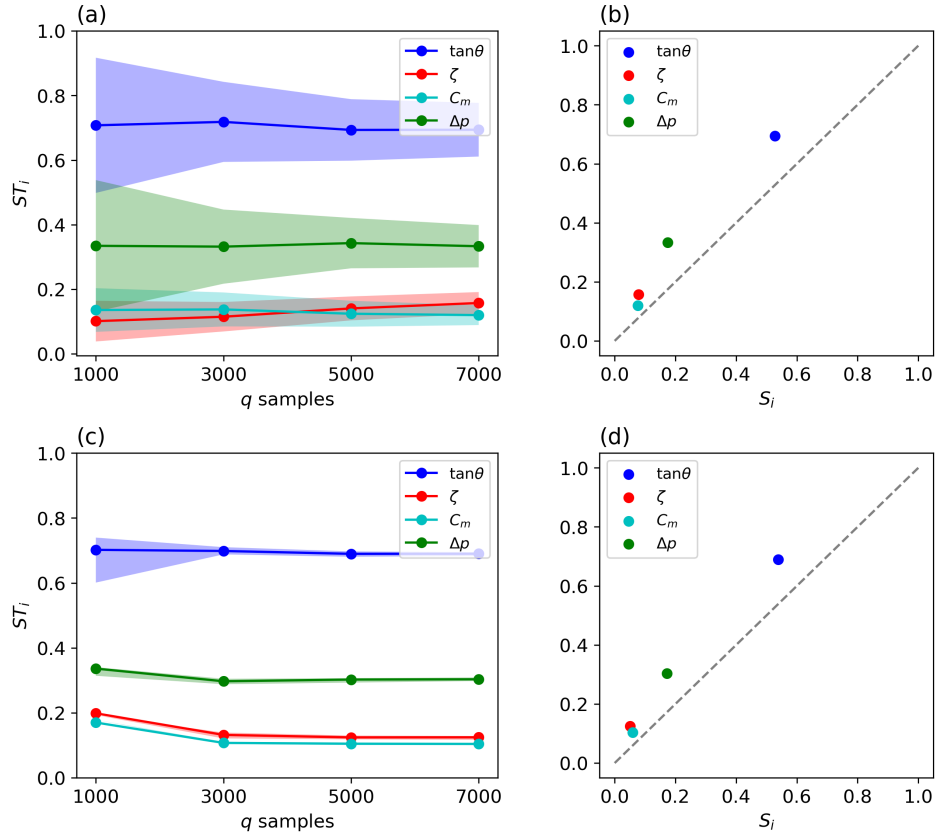

Figure 5.13: Sobol' indices with reference Sobol' method (top panels) and PCE (bottom panels) method. Left panels present the convergence of Sobol' total indices $S_{T,i}$, with the shaded areas in (a) representing the 95% confidence intervals of the indices. The right panels show the relationships between first-order and total indices. After Li et al. [2022].

method. For each variable, S_i accounts for the larger proportion of the corresponding S_{Ti}, indicating a minor contribution from interactions between the i-th variable and the other input factors.

The second-order indices from Sobol' technique and PCE, both computed with 7000 samples, are listed in Table 5.5. The small interaction between input factors is evident. Note that Sobol' technique gives some negative indices for the non-influential terms indicating some computation errors that could not be eliminated with the current sample size [Herman and Usher, 2017].

Figure 5.14(a) depicts MDA importance indices obtained from the GBT

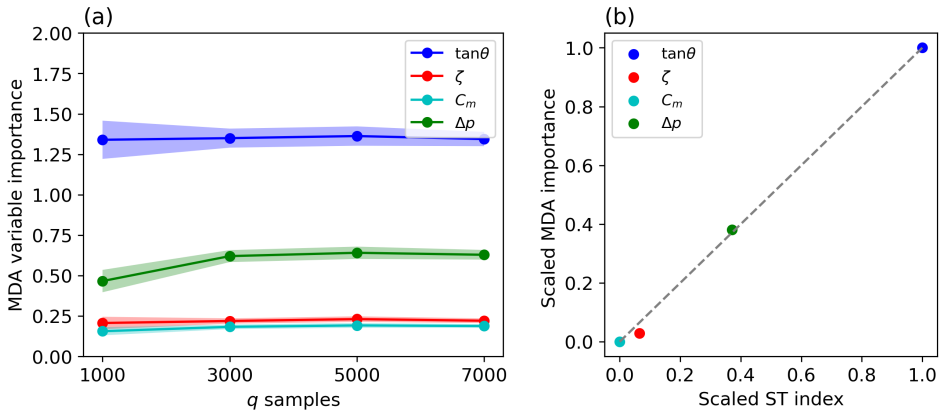

Figure 5.14: MDA metric with the GBT method. (a) Convergence of MDA and (b) comparison of total effect between Sobol' and GBT methods. The importance indices are obtained from the sample size $q = 7000$. After Li et al. [2022].

model with default repetition $K = 100$. A comparison with Sobol' method measures is presented in Figure 5.14(b). Note that Sobol' indices and MDA importance indices measure different quantities, thus a min-max scaling for each value is employed for direct comparison of the indices. According to Eq. 2.85, both PCE and GBT surrogate models reach the convergence criteria $k_q < 0.05$ at $q = 7,000$ (with $\Delta q = 2,000$ samples and $t = 3$ intervals). Conversely, the reference Sobol' method fails to converge at a 7,000 sample size which proves surrogate models can reduce the overall computational cost of analysis with respect to Sobol' method. Moreover, GBT not only ranks the variables in the same way as Sobol' method but also provides basically identical proportional indices with respect to the total effect.

The importance metrics obtained from the three methods highlight that the ridge geometry is the most influential variable for the fissure opening, with the pressure variation also having a non-negligible impact on the fissure development. The contributions from the other two variables are smaller.

5.2.5 Partial Dependence

Partial dependence is also used to investigate the surrogate model response to the variable changes (Figure 5.15). A number of 50 samples from the validation set are used to illustrate how the model prediction of one variable

changes, keeping the other features. Note that each sample is represented by one thin line. The thicker lines represent the partial dependence calculated from the whole validation set (20% of 7,000 samples). Although there are some discrepancies between PCE and GBT results, the trend of partial dependence for each variable is similar.

The impact is limited when $\tan\theta < 1$, however, once exceeding 1.47, the relative activated depth boosts significantly. The model response remains almost constant until $\zeta > 0.8$ when the average line slope abruptly increases, although the contribution of thicker aquifers is still limited. According to the gradient variation, $d_{r,act}$ is more sensitive with c_m up to 0.02 MPa^{-1} and a larger compressibility does not favor a much larger fissure development. Δp causes a relatively larger output variation with respect to ζ and c_m, which is consistent with the variable importance ranking. The slope of partial dependence gently decreases when the absolute value of Δp reduces.

Based on these analyses, we conclude that the ridge geometry and the pressure variation are the first and secondary variables influencing fissure generation and propagation. Therefore, the partial dependence of these two variables is plotted as shown in Figure 5.16. The outcomes of two surrogate models are mainly consistent with respect to the model output distribution. In general, the size of the ridge slope controls the upper limit of the fissure opening, and a certain amount of Δp is necessary for the fissure occurrence.

5.2.6 Discussion

Earth fissuring accompanying differential subsidence above buried bedrock ridges is becoming a worldwide hazard. Since the 1950s, this typical fissure occurrence has been reported, for example, in Casa Grande in Arizona, USA [Jachens and Holzer, 1979], Yangzi Delta in China [Wang et al., 2010], Najran Basin in Saudi Arabia [Youssef et al., 2014]. These studies have pointed out that fissure formation is induced by groundwater depletion and buried geological structures, but the undergoing physical process is not well known owing to little information and limited modelling technique.

Here, the investigation is restricted to the depth of the fissure opening that occurs when the stress normal component becomes greater than zero. Nevertheless, the formation of fissures due to sliding represents another possible mechanism as presented in the multi-fissure formation at Guangming village, China. These are more complex cases, where discontinuities develop

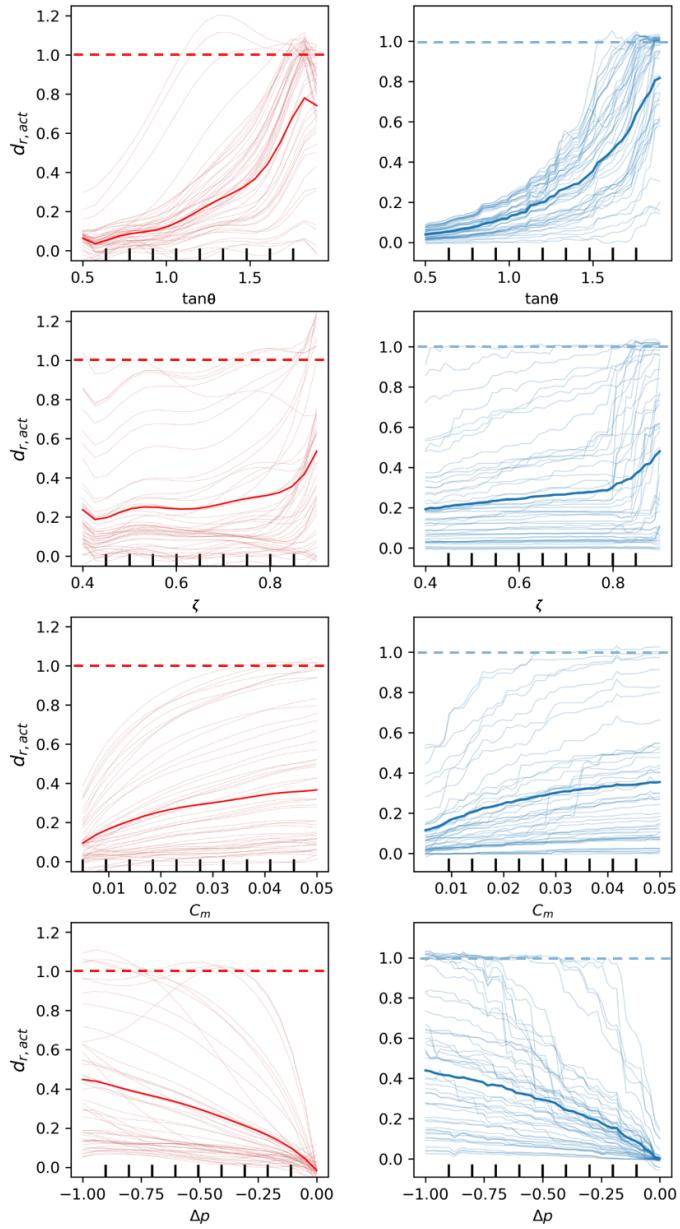

Figure 5.15: Marginal effect of PCE (left panel) and GBT (right panel) methods on the model parameters $\tan\theta$, ζ, c_m, and Δp. Each subplot contains 50 samples which are represented by the thin lines. Partial dependence is highlighted by the thick line. After Li et al. [2022].

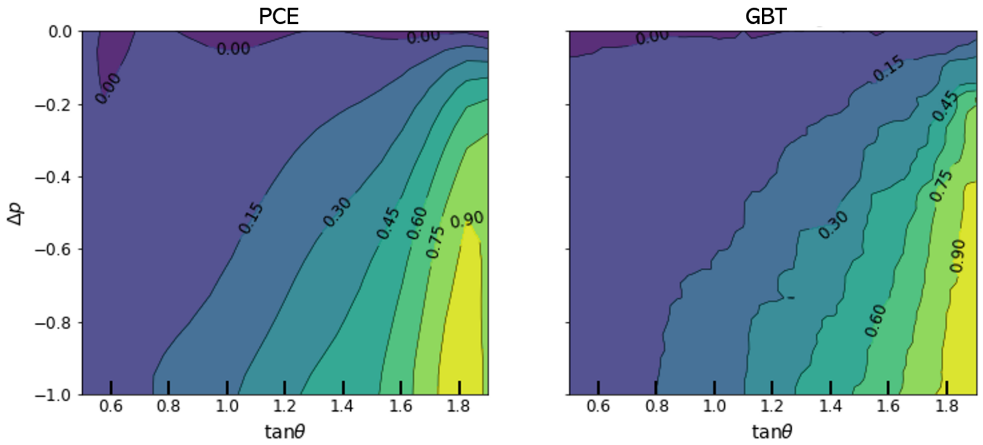

Figure 5.16: Partial dependence of $\tan\theta$ and Δp with PCE (left panel) and GBT (right panel). After Li et al. [2022].

where the stress field reaches the yield surface (Eq. 2.17), and require an appropriate analysis of the stress field in the continuous body before inserting the IEs in the most critical zones of the 3D mesh. Notice that in regions with bare land surface, e.g., in Arizona [Cook, 2011, 2013], initial (thin) fissures caused by stress accumulation can be enlarged at the land surface by erosion and collapses due to surface flow during significant rainfall events. These processes are not accounted for in our modelling approach.

With more fissure appearances over the last decades, researchers started focusing on the quantitative analyses of the fissure formation mechanism. Sheng et al. [2003] defined the ratio of tensile stress over tensile strength as an indication for fissure inception and carried out a one-at-a-time sensitivity analysis which suggested the confining stress and, secondarily, the depth of aquifer as the key parameters for fissure formation. Unfortunately, the impact of the ridge geometry was not taken into account in this analysis.

Frigo et al. [2019] applied a multivariate regression to fit the depth of fissure opening as a function of the pressure variation and the ratio between exploited aquifer thickness and ridge tip depth. The regression surface consists of a pair of planes with discontinuous joints, highlighting that a fissure is more prone to occur when the depth of the ridge tip is shallow. It is also found that pressure depletion plays an important role in controlling differential subsidence. However, multivariate analysis standardizes regression coefficients as direct measures of sensitivity, which is more suitable for linear

problems. Moreover, the number of evaluated variables was restricted to two to derive a regression surface in a 3D setting. Thus, the ridge depth and aquifer geometry were combined in a single parameter.

In the work developed in this thesis, a global sensitivity analysis using a variance-based approach is performed to systematically investigate the model sensitivity to input parameters and model geometry. Sobol' and total effects indices result in ranking the input factors, with a priority of importance assigned to the geometry of the ridge and the pore pressure drop of the system. The aquifer thickness and the compressibility are less influential with respect to the increase in the probability of fissure opening. The interactions between factors are one order of magnitude lower than the main indices, indicating a second-order effect on the output variation.

Results are mostly according to the mentioned previous studies, except for the less importance assigned to the aquifer thickness. However, this parameter was considered in a combined form with the ridge depth in Frigo et al. [2019], probably causing an overestimation effect. Another reason may be attributable to the selection of the bounds values of the uniform distributions from which each parameter is sampled [Wagener and Pianosi, 2019]. For example, the slope of the bedrock ridge ($\tan\theta$) is assumed to variable between 0.5 and 1.9 due to some model grid constraints, discarding all θ values lower than $\sim 27°$. This may result in a not sufficiently wide choice of the parameter space, cutting out the possible influence of the other parameters at lower θ values.

It is also pointed out that further analyses are needed to consider the possibility that variance is not a good measure of the output uncertainty, for example using indices that consider moment independence [Borgonovo, 2007, Pianosi and Wagener, 2015, Dell'Oca et al., 2017].

The multi-fissure simulation illustrates that the distribution of shear stress is influenced by these factors, similar to tensile stress. This suggests that their effect on fissure sliding may be analogous. For instance, a steeper buried ridge may result in greater shear stresses concentrated around the ridge, potentially making it more susceptible to sliding under the same pore pressure decline. However, this hypothesis requires validation through rigorous quantitative analysis, considering the interaction between opening and sliding. Since the locations of shear fissures vary based on different input variables, it's infeasible to adjust the interface elements for each simulation using the current modeling approach. Conducting sensitivity analysis regard-

ing shear fissures requires more flexible modeling approaches to overcome this limitation. PCE surrogates demonstrate stable predictive performance with 4096 Gauss points, while GBT requires 5000 samples to achieve a comparable level. The cost of using surrogates primarily involves obtaining these "training samples" by repeatedly calling the geomechanical simulator. Despite both methods failing to perfectly capture the high discontinuity of $d_{r,act}$, the resulting important metrics align with the Sobol' indices. Furthermore, Sobol' indices require a sample size larger than 7000 to converge, meaning it necessitates calling the geomechanical model over 7000 times. In contrast, the cost of calling for surrogates 7000 times is negligible. Therefore, the use of surrogates is recommended to reduce computational expenses. In particular for the output variables with regularity, the qualified surrogates can be obtained with a handful of samples and the original model is demanding. For instance, the coupled poroelastic model presented in Chapter 3.

Surrogates based on PCE techniques are prominent because of the easy derivation of the Sobol' indices at no additional computational burden. However, it is observed that increasing the level of problem nonlinearity, e.g., in the proximity of the fissure opening, the method fails to provide a good model proxy (e.g., the predicted $d_{r,act} > 1$, see Figure 5.12(a)). For this reason, the GBT algorithm is also employed to estimate total sensitivity measures, i.e., the mean decrease accuracy estimates MDA. Compared to Sobol' indices, MDA importance lacks of a straightforward interpretation, as they are computed based on the model prediction accuracy rather than the effects on the output variance. Thus, MDA is limited to assessing the interaction effects between the input variables. However, this limit can be compensated by using other interpretability methods like SHAP [Lundberg and Lee, 2017] or by using them as an interpretation of Sobol' total effects. The counterpart of this methodology, which seems more suitable for applications on discontinuous problems compared to PCE, is that GBT regression tree spends more time on tuning hyperparameters to optimize the model performance, increasing the overall computational burden.

Chapter 6

Conclusion

This thesis aims to enhance the understanding of land subsidence and earth fissures resulting from groundwater over-exploitation. The specific objectives are to 1) infer the primary hydrogeological and geomechanical properties governing land subsidence, and 2) discern key parameters and their impacts on earth fissure behaviors.

Regarding land subsidence, two distinct strategies are employed for aquifer characterization. The fundamental concept of both strategies revolves around characterizing properties through the integration of numerical simulations and observations, specifically land surface displacements measured by InSAR. The primary difference between the two strategies lies in the spatial variability of the hydromechanical properties.

Specifically, a sparse-gird Bayesian framework is proposed to deduce homogeneous properties in the phreatic aquifer system of the Alto Guadalentín Basin, Spain. The Bayesian framework adopts a coupled poroelastic model, which allows for the incorporation of hydraulic head and displacement records into Bayesian inversion. To reduce the computational cost, the numerical solutions are then substituted by much cheaper surrogates based on sparse grid collocation. Markov Chain Monte Carlo methods enable to generation of large samples to compute the statistical moments of the parameters of interest, providing satisfactory estimates of the hydraulic conductivity and soil compressibility.

In the case of heterogeneous confined aquifer systems, an iterative procedure is employed to characterize the hydraulic conductivity and soil compressibility separately. The focus is on the derivation of the spatial distribution of specific storage using Kriging interpolation. Indirect "observa-

tions" of specific storage are obtained from the Terzaghi 1D consolidation equation taking advantage of InSAR measurements, groundwater flow model solutions, and borehole data. The efficacy of this approach has been demonstrated to estimate the Gaussian field of specific storage of the aquifer system in the Gediz River Basin, Turkey.

In the Alto Guadalentín application, joint inversion of piezometric head and InSAR displacements proved to be more accurate than hydraulic data inversion alone. Simulation outcomes outline significant variations in saturation degree and porosity, indicating that the linkage between the groundwater model and the geomechanical model is crucial in describing the long-term subsidence process in phreatic aquifers. The proposed modelling approach could be enhanced by considering the soil compressibility as a function of porosity. This Bayesian framework has been restricted to low-parameter dimensions, i.e. homogeneous properties. Alternatively, the decoupled strategy proposed in Gediz offers an efficient and straightforward means to characterize the aquifer heterogeneity. Both strategies highlight the potential of InSAR measurements in characterizing aquifer systems.

It must be emphasised that both applications face challenges in capturing the hydraulic behavior of the aquifer systems due to lack of reliable and sufficiently detailed piezometric records and withdrawal information. Further research is required to develop a more robust large-scale joint inversion scheme, using high-fidelity numerical simulators to infer high-dimensional parameters fields, encompassing aquifer properties and source terms such as pumping rates.

As for earth fissures, this thesis adopts a novel numerical approach to simulate multi-fissures in the Guangming village, China, demonstrating how earth fissures form and develop in the presence of a steep bedrock ridge. The subsequent sensitivity analyses highlight the significant impact of the geometry of the ridge on earth fissure behaviors. Notably, a steeper and shallower ridge exacerbates the susceptibility of earth fissures to groundwater depletion, emphasizing the importance of considering geological features in mitigating such hazards and developing sustainable groundwater management.

Overall, this thesis has contributed to understand aquifer systems and associated geohazards through the integration of novel numerical modeling approaches with robust uncertainty quantification methodologies. In a real-world problem, sensitivity analysis is useful for assessing the importance of

uncertain parameters. Once the most influential parameters are identified, an inverse scheme can be employed to quantify the uncertainty associated with these parameters by minimizing the discrepancies between numerical simulations and observations. This process not only enhances prediction accuracy but also facilitates the quantification of uncertainty in aquifer responses through forward modeling, ultimately providing insights into risk assessment and aiding stakeholders in making informed groundwater management decisions. Cost-effective surrogates play a crucial role in managing computational costs throughout this process.

Addressing the challenges involved in these steps requires multidisciplinary approaches. By leveraging expertise from fields such as hydrogeology, geophysics, remote sensing, and computational modeling, comprehensive solutions can be developed for managing groundwater resources sustainably and mitigating associated risks. Collaboration across disciplines ensures that diverse perspectives are considered, leading to more effective and holistic approaches to groundwater management.

Bibliography

A. Alghamdi, M. A. Hesse, J. Chen, and O. Ghattas. Bayesian poroelastic aquifer characterization from insar surface deformation data. part i: Maximum a posteriori estimate. *Water Resources Research*, 56(10):e2020WR027391, 2020.

A. Alghamdi, M. A. Hesse, J. Chen, U. Villa, and O. Ghattas. Bayesian poroelastic aquifer characterization from insar surface deformation data. 2. quantifying the uncertainty. *Water Resources Research*, 57(11):e2021WR029775, 2021.

A. Arabameri, M. Santosh, F. Rezaie, S. Saha, R. Coastache, J. Roy, K. Mukherjee, J. Tiefenbacher, et al. Application of novel ensemble models and k-fold cv approaches for land subsidence susceptibility modelling. *Stochastic Environmental Research and Risk Assessment*, 36(1):201–223, 2022.

M. J. Asher, B. F. Croke, A. J. Jakeman, and L. J. Peeters. A review of surrogate models and their application to groundwater modeling. *Water Resources Research*, 51(8):5957–5973, 2015.

I. Babuška, F. Nobile, and R. Tempone. A stochastic collocation method for elliptic partial differential equations with random input data. *SIAM Journal on Numerical Analysis*, 45(3):1005–1034, 2007.

J. Bear. *Hydraulics of Groundwater*. Dover Publications, Inc., 1979.

M. Béjar-Pizarro, C. Guardiola-Albert, R. P. García-Cárdenas, G. Herrera, A. Barra, A. López Molina, S. Tessitore, A. Staller, J. A. Ortega-Becerril, and R. P. García-García. Interpolation of gps and geological data using insar deformation maps: Method and application to land subsidence in the alto guadalentín aquifer (se spain). *Remote Sensing*, 8(11):965, 2016.

J. W. Bell, F. Amelung, A. Ferretti, M. Bianchi, and F. Novali. Permanent scatterer insar reveals seasonal and long-term aquifer-system response to groundwater pumping and artificial recharge. *Water Resources Research*, 44(2), 2008.

A. Bhosekar and M. Ierapetritou. Advances in surrogate based modeling, feasibility analysis, and optimization: A review. *Computers & Chemical Engineering*, 108:250–267, 2018.

A. W. Bishop. *The Principle of Effective Stress*. Norges Geotekniske Inst., 1960.

P. Blanco-Sánchez, J. J. Mallorquí, S. Duque, and D. Monells. The Coherent Pixels Technique (CPT): An advanced DInSAR technique for nonlinear deformation monitoring. *Pure and Applied Geophysics*, 165:1167–1193, 2008. doi: 10.1007/s00024-008-0352-6.

G. C. Bohling and J. J. Butler Jr. Inherent limitations of hydraulic tomography. *Groundwater*, 48(6):809–824, 2010.

R. Bonì, G. Herrera, C. Meisina, D. Notti, M. Béjar-Pizarro, F. Zucca, P. J. González, M. Palano, R. Tomás, J. Fernández, et al. Twenty-year advanced DInSAR analysis of severe land subsidence: The Alto Guadalentín Basin (Spain) case study. *Engineering Geology*, 198:40–52, 2015.

R. Bonì, C. Meisina, F. Cigna, G. Herrera, D. Notti, S. Bricker, H. McCormack, R. Tomás, M. Béjar-Pizarro, J. Mulas, et al. Exploitation of satellite a-dinsar time series for detection, characterization and modelling of land subsidence. *Geosciences*, 7(2):25, 2017.

E. Borgonovo. A new uncertainty importance measure. *Reliability Engineering & System Safety*, 92(6):771–784, 2007.

L. Breiman. Random forests. *Machine Learning*, 45(1):5–32, 2001.

G. Bru, C. Guardiola-Albert, P. Ezquerro, and M. Béjar-Pizarro. A-DInSAR processing in Gediz River Basin (Turkey). Technical report, RESERVOIR Project Deliverable D3.3, Madrid, Spain, 2021.

G. Bru, J. J. Portela, P. Ezquerro, M. I. Navarro-Hernández, A. Staller, M. Béjar-Pizarro, C. Guardiola-Albert, J. Fernández-Merodo, J. López-Vinielles, R. Tomás, and J. M. López-Sáncez. Imaging land subsidence in the Guadalentín River Basin (SE Spain) using Advanced Differential SAR Interferometry. In *5th Joint International Symposium on Deformation Monitoring (JISDM), Valencia, Spain*, 2022. doi: 0.4995/JISDM2022.2022.13826.

M. Budhu. Earth fissure formation from the mechanics of groundwater pumping. *International Journal of Geomechanics*, 11(1):1–11, 2011.

M. Budhu and A. Shelke. The formation of earth fissures due to groundwater decline. In *Proceedings of the 12th International Conference of International Association for Computer Methods and Advances in Geomechanics (IACMAG)*, pages 3051–3059, 2008.

H.-J. Bungartz and M. Griebel. Sparse grids. *Acta Numerica*, 13:147–269, 2004.

T. J. Burbey. The influence of faults in basin-fill deposits on land subsidence, Las Vegas Valley, Nevada, USA. *Hydrogeology Journal*, 10(5):525–538, 2002.

T. J. Burbey. Mechanisms for earth fissure formation in heavily pumped basins. In *Land Subsidence, Associated Hazards and the Role of Natural Resources Development (Proceedings of EISOLS 2010)*, volume 339, pages 3–8. IAHS Publ., 2010.

D. Carreón-Freyre, M. Cerca, G. Ochoa-González, P. Teatini, and F. R. Zuniga. Shearing along faults and stratigraphic joints controlled by land subsidence in the Valley of Queretaro, Mexico. *Hydrogeology Journal*, 24:657–674, 2016. doi: 10.1007/s10040-016-1384-0.

J. Carrera and S. P. Neuman. Estimation of aquifer parameters under transient and steady state conditions: 1. Maximum likelihood method incorporating prior information. *Water Resources Research*, 22(2):199–210, 1986.

D. V. Carvalho, E. M. Pereira, and J. S. Cardoso. Machine learning interpretability: A survey on methods and metrics. *Electronics*, 8(8):832, 2019.

M. Castagna and A. Bellin. A bayesian approach for inversion of hydraulic tomographic data. *Water Resources Research*, 45(4), 2009.

P. Castellazzi, N. Arroyo-Domínguez, R. Martel, A. I. Calderhead, J. C. Normand, J. Gárfias, and A. Rivera. Land subsidence in major cities of central mexico: Interpreting insar-derived land subsidence mapping with hydrogeological data. *International journal of applied earth observation and geoinformation*, 47:102–111, 2016.

J. Cerón and A. Pulido-Bosch. Groundwater problems resulting from co 2 pollution and overexploitation in alto guadalentín aquifer (murcia, spain). *Environmental Geology*, 28:223–228, 1996.

J. C. Cerón-García. *Estudio hidrogeoquímico del acuífero del Alto Guadalentín (Murcia)*. PhD thesis, Universidad de Granada, 1995.

E. Chaussard, R. Bürgmann, M. Shirzaei, E. J. Fielding, and B. Baker. Predictability of hydraulic head changes and characterization of aquifer-system and fault properties from insar-derived ground deformation. *Journal of Geophysical Research: Solid Earth*, 119(8):6572–6590, 2014.

CHS. Estudio y redacción del plan de ordenación del acuífero del Alto Guadalentín. Technical report, Confederación Hidrográfica del Segura, 1994.

CHS. Asistencia técnica para el estuduio de cuantificación del volumen anual de sobreexplotación de los acuíferos de la Unidad Hidrogeológica 07.28 Alto Guadalentín y 07.33 Aguilas. Technical report, Confederación Hidrográfica del Segura, 2005.

V. Ciriello, V. Di Federico, M. Riva, F. Cadini, J. De Sanctis, E. Zio, and A. Guadagnini. Polynomial chaos expansion for global sensitivity analysis applied to a model of radionuclide migration in a randomly heterogeneous aquifer. *Stochastic Environmental Research and Risk Assessment*, 27(4):945–954, 2013.

B. D. Conway. Land subsidence and earth fissures in south-central and southern Arizona, USA. *Hydrogeology Journal*, 24(3):649–655, 2016.

J. P. Cook. Why did the fissure cross the roads? New and old earth fissure activity in Cochise County, Arizona. *Arizona Geology*, 41(1):Future Article, 2011.

J. P. Cook. Revisiting earth fissures near Luke Air Force Base, central Maricopa County, Arizona. Arizona Geological Survey Open File Report, OFR-13-15, 2013.

J. B. Copas. Regression, prediction and shrinkage. *Journal of the Royal Statistical Society: Series B (Methodological)*, 45(3):311–335, 1983.

V. Couaillier and É. Savin. Generalized polynomial chaos for non-intrusive uncertainty quantification in computational fluid dynamics. In *Uncertainty Management for Robust Industrial Design in Aeronautics*, pages 123–141. Springer, 2019.

O. Coussy. *Poromechanics*. John Wiley & Sons, 2004.

T. Crestaux, O. Le Maître, and J. M. Martinez. Polynomial chaos expansion for sensitivity analysis. *Reliability Engineering and System Safety*, 94(7):1161–1172, 2009. doi: 10.1016/j.ress.2008.10.008.

M. Crosetto, O. Monserrat, M. Cuevas-González, N. Devanthéry, and B. Crippa. Persistent scatterer interferometry: A review. *ISPRS Journal of Photogrammetry and Remote Sensing*, 115:78–89, 2016.

S. De Marchi. On leja sequences: some results and applications. *Applied mathematics and computation*, 152(3):621–647, 2004.

A. Dell'Oca, M. Riva, and A. Guadagnini. Moment-based metrics for global sensitivity analysis of hydrological systems. *Hydrology and Earth System Sciences*, 21(12):6219–6234, 2017. doi: 10.5194/hess-21-6219-2017.

J. Doherty. Ground water model calibration using pilot points and regularization. *Groundwater*, 41(2):170–177, 2003. doi: 10.1111/j.1745-6584.2003.tb02580.x.

J. Doherty, M. Fienen, , and R. Hunt. *Approaches to highly parameterized inversion: Pilot-point theory, guidelines, and research directions.* U.S. Geological Survey Scientific Investigations Report 2010-5168, 36 p, 2010.

V. Dubourg. *Adaptive surrogate models for reliability analysis and reliability-based design optimization.* PhD thesis, Université Blaise Pascal-Clermont-Ferrand II, 2011.

J. Eggleston and J. Pope. Land subsidence and relative sea-level rise in the southern chesapeake bay region. Technical report, US Geological Survey, 2013.

A. Elçi, C. Simsek, O. Gunduz, and A. Baba. *GEDİZ NEHİR HAVZASI YERALTI SUYU AKIM MODELI VE KİRLENME POTANSİYELİ (DRASTIC METODU) RAPORU (Gediz River Basin Groundwater Flow Modeling and Pollution Potential Report).* July 2015. doi: 10.13140/RG.2.2.26021.58084.

A. Elçi, E. A. Batkan, B. Caylak, M. M. Bayirtepe, and A. H. Ören. Groundwater flow model for the Gediz River Basin alluvial aquifer (Turkiye). Technical report, RESERVOIR Project Deliverable D5.3, Ismir, Turkiye, 2022.

P. Ezquerro, C. Guardiola-Albert, G. Herrera, J. A. Fernández-Merodo, M. Béjar-Pizarro, and R. Bonì. Groundwater and subsidence modeling combining geological and multi-satellite SAR data over the Alto Guadalentín aquifer (SE Spain). *Geofluids*, 2017:1–17, 2017.

P. Ezquerro, R. Tomás, M. Béjar-Pizarro, J. Fernández-Merodo, C. Guardiola-Albert, A. Staller, J. Sánchez-Sobrino, and G. Herrera. Improving multitechnique monitoring using Sentinel-1 and Cosmo-SkyMed data and upgrading groundwater model capabilities. *Science of The Total Environment*, 703:134757, 2020.

J. S. Famiglietti. The global groundwater crisis. *Nature Climate Change*, 4(11): 945–948, 2014.

C. C. Faunt, M. Sneed, J. Traum, and J. T. Brandt. Water availability and land subsidence in the central valley, california, usa. *Hydrogeology Journal*, 24(3): 675, 2016.

J. Fernandez, J. F. Prieto, J. Escayo, A. G. Camacho, and et al. Modeling the two- and three-dimensional displacement field in Lorca, Spain, subsidence and the global implications. *Scientific Reports*, 8:14782, 2018.

J. Fernandez-Merodo, P. Ezquerro, D. Manzanal, M. Bejar-Pizarro, R. Mateos, C. Guardiola-Albert, J. Garcia-Davalillo, J. Lopez-Vinielles, R. Sarro, G. Bru, J. Mulas, R. Aragon, C. Reyes-Carmona, P. Mira, M. Pastor, and G. Herrera. Modeling historical subsidence due to groundwater withdrawal in the Alto Guadalentìn aquifer-system (Spain). *Engineering Geology*, 283:105998, 2021. doi: 10.1016/j.enggeo.2021.105998.

L. Formaggia, A. Guadagnini, I. Imperiali, V. Lever, G. Porta, M. Riva, A. Scotti, and L. Tamellini. Global sensitivity analysis through polynomial chaos expansion of a basin-scale geochemical compaction model. *Computational Geosciences*, 17:25–42, 2013.

A. Franceschini, M. Ferronato, C. Janna, and P. Teatini. A novel lagrangian approach for the stable numerical simulation of fault and fracture mechanics. *Journal of Computational Physics*, 314:503–521, 2016.

A. Franceschini, N. Castelletto, and M. Ferronato. Block preconditioning for fault / fracture mechanics saddle-point problems. *Computer Methods in Applied Mechanics and Engineering*, 344:376–401, 2019.

J. H. Friedman. Greedy function approximation: a gradient boosting machine. *Annals of Statistics*, pages 1189–1232, 2001.

N. Friedman and E. Zander. Sglib collection of tutorials. `https://ezander.github.io/ParameterAndFieldIdentification/`, 2020. Accessed: 2021-09-23.

N. Friedman, C. Zoccarato, E. Zander, and H. G. Matthies. A worked-out example of surrogate-based bayesian parameter and field identification methods. In J. Chiachio-Ruano, M. Chiachio Ruano, and S. Snkararaman, editors, *Bayesian Inverse Problems: Fundamentals and Engineering Applications (1st ed.)*, pages 155–203. CRC Press, 2021. doi: 10.1201/b22018.

M. Frigo, M. Ferronato, J. Yu, S. Ye, D. Galloway, D. Carreón-Freyre, and P. Teatini. A parametric numerical analysis of factors controlling ground ruptures caused by groundwater pumping. *Water Resources Research*, 55(11):9500–9518, 2019.

D. L. Galloway and T. J. Burbey. Regional land subsidence accompanying groundwater extraction. *Hydrogeology Journal*, 19(8):1459, 2011.

G. Gambolati and P. Teatini. Geomechanics of subsurface water withdrawal and injection. *Water Resources Research*, 51(6):3922–3955, 2015.

G. Gambolati, P. Teatini, D. BaÃº, and M. Ferronato. Importance of poroelastic coupling in dynamically active aquifers of the Po River Basin, Italy. *Water Resources Research*, 36(9):2443–2459, 2000. doi: 10.1029/2000WR900127.

T. A. Garipov, M. Karimi-Fard, and H. A. Tchelepi. Discrete fracture model for coupled flow and geomechanics. *Computational Geosciences*, 20(1):149–160, 2016. doi: 10.1007/s10596-015-9554-z.

L. Gazzola, M. Ferronato, M. Frigo, C. Janna, P. Teatini, C. Zoccarato, M. Antonelli, A. Corradi, M. C. Dacome, and S. Mantica. A novel methodological approach for land subsidence prediction through data assimilation techniques. *Computational Geosciences*, 25:1731–1750, 2021.

L. Gazzola, M. Ferronato, P. Teatini, C. Zoccarato, A. Corradi, M. C. Dacome, and S. Mantica. Reducing uncertainty on land subsidence modeling prediction by a sequential data-integration approach. Application to the Arlua off-shore reservoir in Italy. *Geomechanics for Energy and the Environment*, 33:100434, 2023. doi: 10.1016/j.gete.2023.100434.

A. Gelman, J. B. Carlin, H. S. Stern, and D. B. Rubin. *Bayesian data analysis*. Chapman and Hall/CRC, 1995.

A. Gelman, W. R. Gilks, and G. O. Roberts. Weak convergence and optimal scaling of random walk metropolis algorithms. *The annals of applied probability*, 7(1):110–120, 1997.

R. G. Ghanem and P. D. Spanos. *Stochastic finite elements: a spectral approach*. Springer Verlag, New York. (Reedited by Dover Publications, Mineola, 2003), 1991.

A. Goldstein, A. Kapelner, J. Bleich, and E. Pitkin. Peeking inside the black box: Visualizing statistical learning with plots of individual conditional expectation. *Journal of Computational and Graphical Statistics*, 24(1):44–65, 2015.

P. J. González and J. Fernández. Drought-driven transient aquifer compaction imaged using multitemporal satellite radar interferometry. *Geology*, 39(6):551–554, 2011.

A. Guzy and A. A. Malinowska. State of the art and recent advancements in the modelling of land subsidence induced by groundwater withdrawal. *Water*, 12 (7):2051, 2020.

Ö. Hacıoğlu, A. T. Başokur, and Ç. Diner. Geothermal potential of the eastern end of the Gediz basin, western Anatolia, Turkey revealed by three-dimensional inversion of magnetotelluric data. *Geothermics*, 91:102040, 2021.

J. Herman and W. Usher. Salib: An open-source python library for sensitivity analysis. *Journal of Open Source Software*, 2(9):97, 2017. doi: 10.21105/joss.00097.

M. Hernandez-Marin and T. J. Burbey. Controls on initiation and propagation of pumping-induced earth fissures: insights from numerical simulations. *Hydrogeology Journal*, 18(8):1773–1785, 2010.

M. Hernandez-Marin and T. J. Burbey. Fault-controlled deformation and stress from pumping-induced groundwater flow. *Journal of hydrology*, 428:80–93, 2012.

M. A. Hesse and G. Stadler. Joint inversion in coupled quasi-static poroelasticity. *Journal of Geophysical Research: Solid Earth*, 119(2):1425–1445, 2014.

J. Hoffmann, D. L. Galloway, and H. A. Zebker. Inverse modeling of interbed storage parameters using land subsidence observations, antelope valley, california. *Water Resources Research*, 39(2), 2003.

A. Hooper. A multi-temporal insar method incorporating both persistent scatterer and small baseline approaches. *Geophysical Research Letters*, 35(16), 2008.

M. A. Iglesias and D. McLaughlin. Data inversion in coupled subsurface flow and geomechanics models. *Inverse Problems*, 28(11):115009, 2012.

B. Iooss and P. Le Maître. A review on global sensitivity analysis methods. In *Uncertainty Management in Simulation-Optimization of Complex Systems*, pages 101–122. Springer, 2015.

G. Isotton, P. Teatini, M. Ferronato, C. Janna, N. Spiezia, S. Mantica, and G. Volonte. Robust numerical implementation of a 3D rate-dependent model for reservoir geomechanical simulations. *International Journal for Numerical and Analytical Methods in Geomechanics*, 43(18):2752–2771, 2019.

R. C. Jachens and T. L. Holzer. Geophysical investigations of ground failure related to groundwater withdrawal - Picacho Basin, Arizona. *Ground Water*, 17(6):574–585, 1979.

C. Janna, N. Castelletto, M. Ferronato, G. Gambolati, and P. Teatini. A geomechanical transversely isotropic model of the Po River basin using PSInSAR derived horizontal displacement. *International Journal of Rock Mechanics and Mining Sciences*, 51:105–118, 2012.

M. Jaxa-Rozen and J. Kwakkel. Tree-based ensemble methods for sensitivity analysis of environmental models: A performance comparison with sobol and morris techniques. *Environmental Modelling & Software*, 107:245–266, 2018. doi: 10.1016/j.envsoft.2018.06.011.

A. Kaintura, T. Dhaene, and D. Spina. Review of polynomial chaos-based methods for uncertainty quantification in modern integrated circuits. *Electronics*, 7(3): 30, 2018.

J. Kaipio and E. Somersalo. *Statistical and computational inverse problems*, volume 160. Springer Science & Business Media, 2006.

M. Karimi-Fard, L. J. Durlofsky, and K. Aziz. An efficient discrete fracture model applicable for general purpose reservoir simulators. In *SPE Reservoir Simulation Symposium*. Society of Petroleum Engineers, 2003. doi: 10.2118/79699-MS.

M. C. Kasmarek and E. W. Strom. *Hydrogeology and simulation of ground-water flow and land-surface subsidence in the Chicot and Evangeline aquifers, Houston area, Texas*, volume 2. US Department of the Interior, US Geological Survey, 2002.

M. R. Kianifar and F. Campean. Performance evaluation of metamodelling methods for engineering problems: Towards a practitioner guide. *Structural and Multidisciplinary Optimization*, 61:159–186, 2020. doi: 10.1007/s00158-019-02352-1.

J. P. Kleijnen. Kriging metamodeling in simulation: A review. *European Journal of Operational Research*, 192(3):707–716, 2009. doi: 10.1016/j.ejor.2007.10.013.

C. Lataniotis, D. Wicaksono, S. Marelli, and B. Sudret. UQLab user manual – Kriging (Gaussian process modeling). Technical report, Chair of Risk, Safety and Uncertainty Quantification, ETH Zurich, Switzerland, 2022. Report UQLab-V2.0-105.

O. Le Maître, O. Knio, H. Najm, and R. Ghanem. Uncertainty propagation using Wiener-Haar expansions. *Journal of Computational Physics*, 197(1):28–57, 2004. ISSN 0021-9991. doi: 10.1016/j.jcp.2003.11.033.

R. W. Lewis and B. A. Schrefler. A finite element simulation of the subsidence of gas reservoirs undergoing a water drive. In *Finite Elements in Fluids*, volume 4, pages 179–199. Wiley Chichester, 1982.

Y. Li, P. Teatini, J. Yu, A. Franceschini, M. Frigo, C. Zoccarato, and S. Ye. Aseismic multifissure modeling in unfaulted heavily pumped basins: Mechanisms and applications. *Water Resources Research*, 57(10):e2021WR030127, 2021. doi: 10.1029/2021WR030127.

Y. Li, N. Friedman, P. Teatini, A. Benczur, S. Ye, L. Zhu, and C. Zoccarato. Sensitivity analysis of factors controlling earth fissures due to excessive groundwater pumping. *Stochastic Environmental Research and Risk Assessment*, 38: 3911–3928, 2022. doi: 10.1007/s00477-022-02237-8.

J. S. Liu and J. S. Liu. *Monte Carlo strategies in scientific computing*, volume 75. Springer, 2001.

Y. Liu, D. Zhang, G.-y. Wang, C. Liu, and Y. Zhang. Discrete element method-based prediction of areas prone to buried hill-controlled earth fissures. *Journal of Zhejiang University - SCIENCE A*, 20(10):794–803, 2019.

G. Louppe. Understanding random forests: From theory to practice. *arXiv preprint arXiv:1407.7502*, 2014.

S. M. Lundberg and S.-I. Lee. A unified approach to interpreting model predictions. In *Proc. of the 31st International Conference on Neural Information Processing Systems*, pages 4768–4777. Curran Associates Inc., 2017.

J. Margat and J. Van der Gun. *Groundwater around the world: a geographic synopsis*. Crc Press, 2013.

J. J. Martínez Díaz, E. Masana, and M. Ortuño. Active tectonics of the alhama de murcia fault, betic cordillera, spain. 2012.

G. Matheron. Principles of geostatistics. *Economic geology*, 58(8):1246–1266, 1963.

D. McLaughlin and L. R. Townley. A reassessment of the groundwater inverse problem. *Water Resources Research*, 32(5):1131–1161, 1996.

M. M. Miller and M. Shirzaei. Spatiotemporal characterization of land subsidence and uplift in Phoenix using InSAR time series and wavelet transforms. *Journal of Geophysical Research: Solid Earth*, 120(8):5822–5842, 2015. doi: 10.1002/2015JB012017.

P. S. Minderhoud, G. Erkens, V. Pham, V. T. Bui, L. Erban, H. Kooi, and E. Stouthamer. Impacts of 25 years of groundwater extraction on subsidence in the mekong delta, vietnam. *Environmental research letters*, 12(6):064006, 2017.

A. Narayan and J. D. Jakeman. Adaptive leja sparse grid constructions for stochastic collocation and high-dimensional approximation. *SIAM Journal on Scientific Computing*, 36(6):A2952–A2983, 2014.

S. Nardean, M. Ferronato, Y. Zhang, S. Ye, X. Gong, and P. Teatini. Understanding ground rupture due to groundwater overpumping by a large lab experiment and advanced numerical modeling. *Water Resources Research*, 57(3): e2020WR027553, 2021.

M. I. Navarro-Hernández, R. Tomás, J. Valdes-Abellan, G. Bru, P. Ezquerro, C. Guardiola-Albert, A. Elçi, E. A. Batkan, B. Caylak, A. H. Ören, C. Meisina, L. Pedretti, and M. Rygus. Monitoring land subsidence induced by tectonic activity and groundwater extraction in the eastern Gediz River Basin (Türkiye) using Sentinel-1 observations. *Engineering Geology*, 327:107343, 2023.

R. M. Neal. Slice sampling. *The Annals of Statistics*, 31(3):705–767, 2003.

G. H. Ochoa-González, D. Carreón-Freyre, A. Franceschini, M. Cerca, and P. Teatini. Overexploitation of groundwater resources in the faulted basin of Querétaro, Mexico: A 3D deformation and stress analysis. *Engineering Geology*, 245:192–206, 2018. doi: 10.1016/j.enggeo.2018.08.014.

C. Paniconi and M. Putti. A comparison of Picard and Newton iteration in the numerical solution of multidimensional variably saturated flow problems. *Water Resources Research*, 30(12):3357–3374, 1994.

F. Pedregosa, G. Varoquaux, A. Gramfort, V. Michel, B. Thirion, O. Grisel, M. Blondel, P. Prettenhofer, R. Weiss, V. Dubourg, J. Vanderplas, A. Passos, D. Cournapeau, M. Brucher, M. Perrot, and E. Duchesnay. Scikit-learn: Machine learning in Python. *Journal of Machine Learning Research*, 12:2825–2830, 2011.

J. Peng, L. Chen, Q. Huang, Y. Men, W. Fan, and J. Yan. Physical simulation of ground fissures triggered by underground fault activity. *Engineering Geology*, 155:19–30, 2013. doi: 10.1016/j.enggeo.2013.01.001.

J. Peng, J. Qiao, X. Sun, Q. Lu, J. Zheng, Z. Meng, J. Xu, F. Wang, and J. Zhao. Distribution and generative mechanisms of ground fissures in china. *Journal of Asian Earth Sciences*, 191:104218, 2020.

M. Peng, Z. Lu, C. Zhao, M. Motagh, L. Bai, B. D. Conway, and H. Chen. Mapping land subsidence and aquifer system properties of the willcox basin, arizona, from insar observations and independent component analysis. *Remote Sensing of Environment*, 271:112894, 2022.

F. Pianosi and T. Wagener. A simple and efficient method for global sensitivity analysis based on cumulative distribution functions. *Environmental Modelling & Software*, 67:1–11, 2015. doi: 10.1016/j.envsoft.2015.01.004.

C. Piazzola and L. Tamellini. The Sparse Grids Matlab kit–a Matlab Implementation of Sparse Grids for High-Dimensional Function Approximation and Uncertainty Quantification. *ACM-TOMS*, 2023a. doi: 10.1145/3630023.

C. Piazzola and L. Tamellini. The Sparse Grids Matlab Kit. 2023b. `https://github.com/lorenzo-tamellini/sparse-grids-matlab-kit`.

A. Pirouzi and A. Eslami. Ground subsidence in plains around tehran: site survey, records compilation and analysis. *International Journal of Geo-Engineering*, 8 (1):30, 2017.

G. Porta, L. Tamellini, V. Lever, and M. Riva. Inverse modeling of geochemical and mechanical compaction in sedimentary basins through p olynomial c haos e xpansion. *Water Resources Research*, 50(12):9414–9431, 2014.

P. Probst, A.-L. Boulesteix, and B. Bischl. Tunability: importance of hyperparameters of machine learning algorithms. *The Journal of Machine Learning Research*, 20(1):1934–1965, 2019.

N. Rahmawati, J.-F. Vuillaume, and I. L. S. Purnama. Salt intrusion in coastal and lowland areas of semarang city. *Journal of hydrology*, 494:146–159, 2013.

S. Razavi, B. A. Tolson, and D. H. Burn. Review of surrogate modeling in water resources. *Water Resources Research*, 48(7), 2012.

A. Rezaei and Z. Mousavi. Characterization of land deformation, hydraulic head, and aquifer properties of the gorgan confined aquifer, iran, from insar observations. *Journal of Hydrology*, 579:124196, 2019.

O. Roustant, J. Fruth, B. Iooss, and S. Kuhnt. Crossed-derivative based sensitivity measures for interaction screening. *Mathematics and Computers in Simulation*, 105:105–118, 2014.

Y. Rubin, X. Chen, H. Murakami, and M. Hahn. A bayesian approach for inverse modeling, data assimilation, and conditional simulation of spatial random fields. *Water Resources Research*, 46(10), 2010.

A. Saltelli. Sensitivity analysis for importance assessment. *Risk Analysis*, 22(3): 579–590, 2002.

A. Saltelli and P. Annoni. How to avoid a perfunctory sensitivity analysis. *Environmental Modelling & Software*, 25(12):1508–1517, 2010.

T. J. Santner, B. J. Williams, W. I. Notz, and B. J. Williams. *The Design and Analysis of Computer Experiments*, volume 1. Springer, 2003.

Z. Sheng and D. C. Helm. Multiple steps of earth fissuring caused by ground-water withdrawal. In *Land Subsidence Case Studies and Current Research: Proceedings of the Dr. Joseph F. Poland Symposium on Land Subsidence*, volume 8, pages 149–154. Assoc. Eng. Geol. Special Publication, 1998.

Z. Sheng, D. C. Helm, and J. Li. Mechanisms of earth fissuring caused by groundwater withdrawal. *Environmental & Engineering Geoscience*, 9(4):351–362, 2003.

X.-Q. Shi, Y.-Q. Xue, S.-J. Ye, J.-C. Wu, Y. Zhang, and J. Yu. Characterization of land subsidence induced by groundwater withdrawals in Su-Xi-Chang area, China. *Environmental Geology*, 52(1):27–40, 2007.

H. Si. Adaptive tetrahedral mesh generation by constrained Delaunay refinement. *International Journal for Numerical Methods in Engineering*, 75(7):856–880, 2008. doi: 10.1002/nme.2318.

R. G. Smith, R. Knight, J. Chen, J. Reeves, H. Zebker, T. Farr, and Z. Liu. Estimating the permanent loss of groundwater storage in the southern s an j oaquin v alley, c alifornia. *Water Resources Research*, 53(3):2133–2148, 2017.

I. M. Sobol'. Sensitivity analysis for non-linear mathematical models. *Mathematical Modelling and Computational Experiment*, 1:407–414, 1993.

I. M. Sobol'. Global sensitivity indices for nonlinear mathematical models and their monte carlo estimates. *Mathematics and Computers in Simulation*, 55 (1-3):271–280, 2001.

I. M. Sobol', D. Asotsky, A. Kreinin, and S. Kucherenko. Construction and comparison of high-dimensional sobol'generators. *Wilmott*, 2011(56):64–79, 2011.

P. Sochala and O. Le Maître. Polynomial chaos expansion for subsurface flows with uncertain soil parameters. *Advances in Water Resources*, 62:139–154, 2013. ISSN 0309-1708. doi: 10.1016/j.advwatres.2013.10.003.

A. M. Stuart. Inverse problems: A Bayesian perspective. *Acta Numerica*, 19: 451–559, 2010. doi: 10.1017/S0962492910000061.

B. Sudret. Global sensitivity analysis using polynomial chaos expansions. *Reliability Engineering & System Safety*, 93(7):964–979, 2008.

SYGM. Project of the preparation of water allocation plans for the Küçük Menderes and Gediz River Basins. Current status analysis report, Ankara, Turkiye. Technical report, SYGM, 2017.

A. Tarantola. *Inverse problem theory and methods for model parameter estimation.* SIAM, 2005.

P. Teatini, M. Ferronato, G. Gambolati, W. Bertoni, and M. Gonella. A century of land subsidence in Ravenna, Italy. *Environmental Geology*, 47(6):831–846, 2005.

P. Teatini, M. Ferronato, G. Gambolati, and M. Gonella. Groundwater pumping and land subsidence in the Emilia-Romagna coastland, Italy: Modeling the past occurrence and the future trend. *Water Resources Research*, 42(1), 2006a. doi: 10.1029/2005WR004242.

P. Teatini, M. Ferronato, G. Gambolati, and M. Gonella. Groundwater pumping and land subsidence in the emilia-romagna coastland, italy: Modeling the past occurrence and the future trend. *Water Resources Research*, 42(1), 2006b.

P. Teatini, N. Castelletto, M. Ferronato, G. Gambolati, and L. Tosi. A new hydrogeologic model to predict anthropogenic uplift of Venice. *Water Resources Research*, 47(12), 2011a. doi: 10.1029/2011WR010900.

P. Teatini, G. Gambolati, M. Ferronato, A. T. Settari, and D. Walters. Land uplift due to subsurface fluid injection. *Journal of Geodynamics*, 51(1):1–16, 2011b. doi: 10.1016/j.jog.2010.06.001.

K. Terzaghi, R. B. Peck, and G. Mesri. *Soil Mechanics in Engineering Practice*. John Wiley & Sons, 1996.

S. Üner and D. D. Dogan. An integrated geophysical, hydrological, thermal approach to finite volume modelling of fault-controlled geothermal fluid circulation in Gediz Graben. *Geothermics*, 90:102004, 2021.

M. T. Van Genuchten and D. Nielsen. On describing and predicting the hydraulic properties. *Annales Geophysicae*, 3(5):615–628, 1985.

M. Vittek, P. Borovansky, and P.-E. Moreau. A simple generic library for C. In *Reuse of Off-the-Shelf Components. Proc. of 9th International Conference on Software Reuse, Turin, Italy*, pages 423–426. Springer, 2006.

C. M. Wade, K. M. Cobourn, G. S. Amacher, and E. T. Hester. Policy targeting to reduce economic damages from land subsidence. *Water Resources Research*, 54(7):4401–4416, 2018.

T. Wagener and F. Pianosi. What has global sensitivity analysis ever done for us? A systematic review to support scientific advancement and to inform policy-making in earth system modelling. *Earth-Science Reviews*, 194:1–18, 2019. doi: 10.1016/j.earscirev.2019.04.006.

G. Wang, G. You, B. Shi, Z. Qiu, H. Li, and M. Tuck. Earth fissures in Jiangsu Province, China, and geological investigation of Hetang earth fissure. *Environmental Earth Sciences*, 60(1):35–43, 2010.

H. Wang. *Theory of Linear Poroelasticity with Applications to Geomechanics and Hydrogeology*, volume 2. Princeton university press, 2000.

Z. Wang, Y. Zhang, J. Wu, J. Yu, and X. Gong. Numerical simulation of earth fissures due to groundwater withdrawal. *Proceedings of the International Association of Hydrological Sciences*, 372:395–398, 2015.

G. W. Wasilkowski and H. Wozniakowski. Explicit cost bounds of algorithms for multivariate tensor product problems. *Journal of Complexity*, 11(1):1–56, 1995.

N. Wiener. The homogeneous chaos. *American Journal of Mathematics*, 60(4): 897–936, 1938. doi: 10.2307/2371268.

R. Winston. *ModelMuse version 5.1.1*. U.S. Geological Survey Software Release, https://doi.org/10.5066/P90QQ94D, 2022.

A. D. Woodbury and Y. Rubin. A full-bayesian approach to parameter inference from tracer travel time moments and investigation of scale effects at the cape cod experimental site. *Water Resources Research*, 36(1):159–171, 2000.

D. Xiu. Efficient collocational approach for parametric uncertainty analysis. *Communications in Computational Physics*, 2(2):293–309, 2007.

D. Xiu and J. S. Hesthaven. High-order collocation methods for differential equations with random inputs. *SIAM Journal on Scientific Computing*, 27(3):1118–1139, 2005.

S. Ye, Y. Wang, J. Wu, P. Teatini, J. Yu, X. Gong, and G. Wang. Characterization of earth fissures in South Jiangsu, China. *Proceedings of the International Association of Hydrological Sciences*, 372:249–253, 2015. doi: 10.5194/piahs-372-249-2015.

S. Ye, Y. Luo, J. Wu, X. Yan, H. Wang, X. Jiao, and P. Teatini. Three-dimensional numerical modeling of land subsidence in Shanghai, China. *Hydrogeology Journal*, 24(3):695–709, 2016.

S. Ye, A. Franceschini, Y. Zhang, C. Janna, X. Gong, J. Yu, and P. Teatini. A novel approach to model earth fissure caused by extensive aquifer exploitation and its application to the Wuxi case, China. *Water Resources Research*, 54(3): 2249–2269, 2018.

J. Yoo and T. Frederick. The varying impact of land subsidence and earth fissures on residential property values in maricopa county–a quantile regression approach. *International Journal of Urban Sciences*, 21(2):204–216, 2017.

A. M. Youssef, A. A. Sabtan, N. H. Maerz, and Y. A. Zabramawi. Earth fissures in Wadi Najran, Kingdom of Saudi Arabia. *Natural Hazards*, 71(3):2013–2027, 2014.

E. Zander. Sglib github repository. `https://github.com/ezander/sglib-testing`, 2020. Accessed: 2021-09-23.

Y. Zhang, Z. Wang, Y. Xue, J. Wu, and J. Yu. Mechanisms for earth fissure formation due to groundwater extraction in the Su-Xi-Chang area, China. *Bulletin of Engineering Geology and the Environment*, 75(2):745–760, 2016.

L. Zhu, A. Franceschini, H. Gong, M. Ferronato, Z. Dai, Y. Ke, Y. Pan, X. Li, R. Wang, and P. Teatini. The 3-D facies and geomechanical modeling of land subsidence in the Chaobai Plain, Beijing. *Water Resources Research*, 56(3), 2020. doi: 10.1029/2019WR027026.

C. Zoccarato, M. Ferronato, A. Franceschini, C. Janna, and P. Teatini. Modeling fault activation due to fluid production: Bayesian update by seismic data. *Computational Geosciences*, 23:705–722, 2019.

C. Zoccarato, L. Gazzola, M. Ferronato, and P. Teatini. Generalized polynomial chaos expansion for fast and accurate uncertainty quantification in geomechanical modelling. *Algorithms*, 13(7):156, 2020.